99-0136

Safety in Mines Research Advisory Committee

Final Project Report

Improvement of worker safety through the investigation of the site response to rockbursts

T O Hagan, A M Milev, S M Spottiswoode,
B Vakalisa and N Reddy

Research agency : CSIR: Division of Mining Technology
Project number : GAP 530
Date : December 1998
Library reference
Number : 990136

Table of contents

Page

Table of contents 2
Executive summary 4
Preface 6
Acknowledgements 7
List of figures 8
List of tables 13
1 Introduction 14
1.2 Project outputs 14
1.3 Research Methodologies 15
1.4 Structure of the report 16
2 Rockburst investigations 16
2.1 Introduction 16
2.2 Source Mechanisms 18
2.3 Damage Mechanisms 21
2.4 Conclusions and Recommendations 30
3 Controlled seismic source experiment 31
3.1 Introduction 31
3.2 Test site and instrumentation 32
3.3 Calibration blast and pre-blast monitoring 34
3.4 Numerical modelling for planning the main blast and expected velocities 36
3.5 Main blast 45
3.5.1 Source description 45
3.5.2 Seismic observations in the near field 47
3.5.3 Seismic observations in far field 58
3.6 Post blast measurements 61
3.6.1 Tunnel wall damage 62
3.6.2 Amplification of the seismic signal monitoring after the blast 67
3.7 Conclusions 73
4 Dynamic behaviour of the rock around underground excavations 75
4.1.1 Introduction 75
4.1.2 Site description. 75
4.1.3 Method of observation 78
4.1.4 Analysis of peak particle velocities 82

4.1.4.1 Up-hole micro seismic array (3 D observations)....82
4.1.4.2 In-stope measurements of the peak particle velocities (2 D seismic array)....87
4.1.5 Dynamic response of the hangingwall observed by 3 D micro seismic array. 91
4.1.6 Conclusions....94
4.2 Dynamic behaviour of pre-stressed elongates: underground measurements at Western Deep Levels, East Mine site....95
4.2.1 Introduction....95
4.2.2 Data....95
4.2.3 Analysis....97
4.2.4 Conclusions....101
4.3 Triaxial measurements of peak particle velocities in underground tunnel: Kloof Gold Mine....101
4.3.1 Introduction. 102
4.3.2 Site description....103
4.3.3 Data....104
4.3.4 Results....105
4.3.5 Conclusions and discussions....110
5 New interpretation techniques and developments....110
5.1 Rock mass behaviour under seismic loading in a deep mine environment...110
5.1.1 Summary....110
5.1.2 Introduction....111
5.1.3 Three-dimensional image of ground motion....112
5.1.4 Spectral analysis of the three dimensional ground motion....116
5.1.5 Structural effect....120
5.1.6 Site Effect – Microzonation....121
5.1.7 Multi-degree-of-freedom model in time and frequency domains....124
5.1.8 Conclusions....127
5.2 Monitoring falls of ground with Modified Ground Motion Monitor....128
5.3 Single-block rockburst model....130
6 Conclusions and Recommendations....132
7 References....136
8 Published Articles....142

Executive summary

The objective of this investigation is to improve worker safety through a better understanding of mine excavation response to rockbursts. The improved understanding should lead to improved mine layout and support design. The project is a continuation of GAP 201 and consists of two main enabling areas namely:

- a comprehensive investigation of rockbursts that have caused damage and posed a hazard to workers
- measurement and analysis of the dynamic response of the rock surrounding excavations following seismic shaking

Twenty-eight accident site investigations were completed in the years 1994 to 1997, inclusive, mainly as part of project GAP 201. Six additional investigations were done in 1998 as part of this project and in combination with the initial findings have served to highlight certain aspects of the rockburst phenomenon. These aspects include the existence of the following problem areas that need to be addressed:

- a lack of knowledge of the stress fields affecting a particular mine
- an underestimation of the extent of the unstable zone surrounding tunnels
- poor condition of tunnel support elements due to corrosion
- siting of tunnels in areas of fault loss and tunnels intersecting faults at oblique angles
- ineffective gully support design and implementation
- shape of remnant pillars
- backfill usage

The source mechanism in the vast majority of cases was diagnosed as a seismic event resulting from slip on either a dyke contact or a fault. In some cases the seismic data coupled with the extent, nature and location of the damage make the degree of certainty, with respect to the source mechanism involved, extremely high.

Other source mechanisms include remnant pillar failure, stabilising pillar foundation failure and face bursts.

The most common damage mechanism resulting from seismic activity is predictably collapse and shakedown of hangingwall. Other mechanisms are tunnel wall and footwall heave occurred in both tunnels and stopes.

Many factors affect the severity of damage. Mine layout factors include poor remnant shape, inappropriate pillar design, and broadside on face orientation when approaching geological features and excessive leads or lags between panels. Incorrect input parameters, such as k-ratios when modelling also result in inappropriate layouts. Tunnels positioned in fault loss zones sustained serious damage in some cases. Inappropriate and poorly designed support in tunnels, gullies and stopes and in some cases sub-standard application of the support in these crosscut also played a role in determining the severity of the sustained damage.

As one of the enabling outputs of GAP 530 a seismic event was successfully simulated by means of a large blast in solid rock close to an excavation. The idea was to thoroughly instrument the resultant "rockburst" site in order to gain further insight into the damage mechanisms involved. The results were startlingly similar to what would be expected in a rockburst. Ground penetrating radar scans and petroscope probes indicated the development of new fractures parallel to the tunnel sidewall. High speed camera shots revealed that fragments of rock were being ejected from the tunnel wall at velocities of up to 3,3 m/s. The amplification of peak particle velocities on the surface of the tunnel wall after the blast was increased five to six fold indicative of the damage resulting from the simulated seismic event. Tendon support in the tunnel had the effect of reducing the peak particle velocities and damage to the wall. All the above results have important implications with respect to support design.

Site response measurements at other sites showed that two distinct mechanisms exist i.e. associated with structural response and local site response. The former reflects behaviour common to the site as a whole and the latter on the other hand reflects the behaviour of individual blocks.

The results from the 3 D seismic measurements show two possible mechanisms of dynamic behaviour: structural response, defined as a common spectral behaviour at all surface seismograms; and local site effect, defined by spectral peaks at one or two surface seismograms.

Other ground motion measurements on the two opposite walls of a tunnel revealed that peak velocities may be affected by the position of the event source relative to the wall. This directional dependence means that some parts of the excavation may be more hazardous than others. However, this phenomenon has not being fully studied and more observations are required.

Preface

The knowledge gained during the course of this project has been and will be disseminated by means of publication for the conferences, symposia and seminars listed below. In addition, reports on the findings of rockburst investigations have been presented to mine management. Key findings will be included in the revision of the Industry Guide to the Amelioration of the Hazards of Rockfalls and Rockbursts (COMRO, 1988), scheduled for publication in 1999.

Hagan, T.O. 1998. Rockburst investigations – some case studies. *SIMRAC Symposium*, July, Delta Park, Johannesburg.

Hagan, T.O., Durrheim, R.J., Roberts, M.K.C. and Haile, A.T. 1998. Rockburst investigations in South African Mines, *Proc of the 9th ISRM congress, Paris, 1999.*

Milev, A.M., Spottiswoode S.M. and Stewart R. J. 1998. Dynamic response of the rock surrounding deep level mining excavations, *Proc of the 9th ISRM congress,* Paris, 1999.

Hagan, T.O., Milev, A.M., Spottiswoode, S.M., Reddy, N. and Hildyard, M.W. 1998. Simulated rockburst on the wall of an underground tunnel, In: T.O. Hagan (Editor), *Proc. 2nd SARES symposium,* Johannesburg.

Hildyard, M.W., Milev, A.M., and Rorke A.J. 1998. Numerical modelling of an experimental rockburst near a mining tunnel, In: T.O. Hagan (Editor), *Proc. 2nd SARES symposium,* Johannesburg.

Hagan, T.O. 1998. Rockburst site response investigations, *SIMRAC Symposium,* Kloof, South Africa.

Acknowledgements

The authors of the report would like to express their thanks to SIMRAC for the financial support and to the GAPREAG committee for their encouragement. To the management, production and rock engineering staff of the following mines we wish to express our sincere appreciation for their assistance and co-operation at the various experiment sites:

- Kopanang Mine
- Western Deep levels Limited
- Lonrho Eastern Plats

The success of the rockburst investigations depended on the support of many persons on a number of mines. We are grateful for the willing assistance we received.

List of figures

Page

Figure 2.1 Plan of rockburst site of Hartebeestfontein Gold Mine. 18
Figure 2.2 Section of a stabilising pillar with shear along the pillar edge 20
Figure 2.3 Buckling of the Greenbar in the gully hangingwall. 20
Figure 2.4 Various forms of support failure in a tunnel. 23
Figure 2.5 Rock ejected from the face against first line of packs. 26
Figure 2.6 Site of the remnant pillar on Deelkraal Gold Mine....27
Figure 2.7 Closure on backfill in the back area. 28
Figure 3.1 Controlled seismic source experiment layout and deployment of the seismic sensors. 33
Figure 3.2 Attenuation curve of peak particle velocities measured from the calibration blast. 34
Figure 3.3 Comparison of model with geophone recordings from calibration blast, for modelled source of 9 GPa, 800 μs rise-time, step shape load and 0,1m diameter. Geophones C8, C3, C6 and C5 extended in a line along the near tunnel wall, starting at 5,8 m from the blast and in approximately 4 m intervals. Motion is normal to the tunnel wall. 41
Figure 3.4 Maximum velocity on tunnel wall for pre-blast model, source # 3 9 GPa, 800 μs, step shape load and 0,3 m diameter, with a single 8 m blasthole. 42
Figure 3.5 Comparison of the pre-blast model velocities for source #3 with the final blast measurements for geophones C5, C6, C4 and C8 starting at 7 m ahead of the blast, and at approximately 4 m intervals along the tunnel wall. 43
Figure 3.6 Maximum velocities at near tunnel wall for the post-blast model source #4. Maximum velocity for a blast pressure of 1 GPa is much lower than that recorded. Position of maximum velocity is now opposite the blast holes, due to the relatively long wavelength, and synchronisation of the blasts. 44
Figure 3.7 Graphical illustration of the main blast source. 47
Figure 3.8 (a) The accelerogram recorded in the area of high-intensity damage. This accelerometer was ejected at 3.3 m/s. 48
Figure 3.8 (b) The accelerogram recorded in the area of low-intensity damage. 48

Figure 3.8 (c) The accelerogram recorded in the solid rock 3 m into the hangingwall close to the area of damage. 49
Figure 3.9 Displacement curves for six fragments and one marker ball. 54
Figure 3.10 Fitted curves limited to first 100 ms of data. The second point for fragment 7 has been omitted. 54
Figure 3.11 Comparison of peak particle velocities recorded in solid rock to peak particle velocities measured on the skin of the blasting wall in the areas of different degrees of fragmentation. 56
Figure 3.12 Attenuation curve of peak particle velocities measured from the main blast. 57
Figure 3.13 (a, b, c) Three component seismogram of the blast recorded by the Vaal River Operations regional seismic network at station 850 m from the blast; a) is horizontal component X, b) is horizontal component Y and c) is the vertical component. 59
Figure 3.14 Energy emitted in P- waves versus energy emitted in S- waves for the blast and 14 mine induced seismic events located in the same portion of the mine. 60
Figure 3.15 Energy versus moment for the blast and 14 mine induced seismic events located in the same portion of the mine 61
Figure 3.16 Geometry of the controlled seismic source experiment site. 62
Figure 3.17 Photograph of a portion of the damaged sidewall. A rockbolt can be seen in the top centre. 64
Figure 3.18 Volume of rock ejected along the tunnel wall. 65
Figure 3.19 A ground penetrating radar scan taken after the simulated seismic event. The lower part of the plot is at the skin of the tunnel and the top part of the plot is at 9 m penetration. 66
Figure 3.20 A plan of the test site. 68
Figure 3.21 Peak particle velocities measured on the blasting wall, the hangingwall and the footwall before the main blast. 69
Figure 3.22 Peak particle velocities measured on the blasting wall, the hangingwall and the footwall after the main blast. 70
Figure 3.23 Peak particle velocities measured on the blasting wall before the main blast. 71
Figure 3.24 Peak particle velocities measured on the blasting wall after the main blast. 71
Figure 3.25 A Log_{10} amplitude spectral ratio, closer to distant geophone for seismic events recorded at the blasting wall, before the blast. 72

Figure 3.26 A Log_{10} amplitude spectral ratio for the seismic events recorded at the blasting wall, closer geophone to the distant one, after the main blast. 73
Figure 4.1 Mining plan and position of the test sites. 76
Figure 4.2 Stratigraphic column of the Carbon Leader. 77
Figure 4.3 (a) Determination of velocity for a plane wave passing a pair of spatially separated geophones; (b) Example of difference in recorded arrivaltimes at a pair of spatially separated geophones. 81
Figure 4.4 Plan and sectional view of 3 D micro seismic network installed at WDL, East Mine, 93E4 panel: configuration I, operated from January '98 to May '98; configuration II has operated since May '98..83
Figure 4.5 Maximum velocities recorded at site WDL, East mine, 93E4 panel, geophones A, B, C and D are installed in the borehole from top to bottom. 85
Figure 4.6 Maximum velocities recorded at site WDL, East mine, 93E4 panel (3D observations): G2 to G6 are placed on the hangingwall, G1 is about 5 into a hangingwall, and G7 is on the footwall. 86
Figure 4.7 Configuration of micro seismic array consisting of two ground motion monitors (A & B) with a common trigger and 15 geophones. All geophones are on the hangingwall except B5, B6 and B7 which are located on the footwall. 88
Figure 4.8 Maximum velocities recorded by box "A" (Figure 4.7). All geophones A1 to A8 are on the hangingwall. The geophone A8 is low gain. 89
Figure 4.9 Log_{10} spectral ratio (A5/A4) of the seismic signal recorded on both sides of a fault by geophones 20 cm from each other shown in Figure 4.7. 90
Figure 4.10 Maximum velocities recorded by box "B" (Figure 4.7). Geophones B1 to B4 and B8 are placed on the hangingwall. Geophones B5 to B7 are on the footwall. Geophone B8 is low gain. 91
Figure 4.11 Log_{10}(spectral ratio) of the seismic signal recorded at 6,5 m into the hangingwall (G1) and a number of seismic signals recorded at the skin of the excavation (G2, G3, G4, G5 and G6) for configuration I from Figure 4.4. 92
Figure 4.12 Log_{10}(spectral ratio) of the seismic signal recorded in solid rock (G1) and a number of seismic signals recorded at the skin of the excavation (G2, G3, G4, G5 and G6) for configuration II from Figure 4.4. 93

Figure 4.13 A schematic diagram shows the instrumentation of the props, the footwall and the hangingwall. An 8 channel Ground Motion Monitor connected to 8 uniaxial vertical geophones was used. The geophones were connected to the box via a junction box (JB). 96
Figure 4.14 (a) Log_{10} velocity amplitude spectrum of the channels recorded on and close to the Eben Haeser prop. 97
Figure 4.14 (b) Log_{10} velocity amplitude spectrum of the channels recorded on and close to the pencil prop.....98
Figure 4.15 (a) Median phase differences between the footwall channel 1 and other channels at the Eben Haeser prop site. 99
Figure 4.15 (b) Median phase differences between the two prop channels and the hangingwall channel at the Eben Haeser prop site. 100
Figure 4.16 (a). Median phase differences between the footwall channel 5 and other channels at the pencil prop site. 100
Figure 4.16 (b). Median phase differences between the two prop channels and the hangingwall channel at the pencil prop site. 101
Figure 4.17 Experimental setup (a) showing the cross-section of a tunnel with triaxial sensor positions; (b) plan view of the experimental site and its surrounding areas. The diagrams are not drawn to scale. ...104
Figure 4.18 (a) Peak velocities of three mutually orthogonal components of the eastern sidewall site plotted on the same graph. 105
Figure 4.18 (b) Peak velocities of three mutually orthogonal components of the western sidewall site plotted on the same graph.....105
Figure 4.18 (c) Peak velocities of two mutually orthogonal components of the hanging wall plotted on the same graph. The component perpendicular to the surface had resonance. 106
Figure 4.19 (a) Peak velocities of events common to eastern and western walls recorded perpendicular (x component) to the walls. 107
Figure 4.19 (b) Peak velocities of events common to eastern and western walls recorded tangential (y component) to the walls.....107
Figure 4.19 (c) Peak velocities of events common to eastern and western walls recorded tangential (z component) to the walls.....108
Figure 4.20 (a) Log_{10} average velocity spectra of events from the eastern wall (solid line) and events from the western wall (dashed line). Only events common to both walls were considered.....109

Figure 4.20 (b) Log_{10} average velocity spectra of events from the eastern wall (solid line) and events from the western wall (dashed line). All events recorded at the walls were considered.....109
Figure 5.1. Seismograms recorded by the Portable Seismic System (borehole array, vertical channels). Stations A, B, C and D are located from the top to the bottom. 113
Figure 5.2 Seismograms recorded by the Ground Motion Monitor (surface array, vertical channels). Channels 2, 3, 4, 5 and 6 are located on the skin of the hangingwall and channel 7 is on the footwall.....115
Figure 5.3 Amplitude spectra of body wave group for events recorded by the borehole array. The records from sites A and B are marked by a solid lines; record from station C is marked with dashed-dot line and record from station D is marked by a dotted line. ...118
Figure 5.4 The sum of three modal responses calculated at the time 0,105 s (solid line); the match with the real ground motion is very good (channel 5 - dashed line). 125
Figure 5.5 Observed (solid line) and calculated (dashed line) spectra for channel 5. The third curve is the transfer function in the frequency domain between channel 6 and channel 5. 126
Figure 5.6 Sketch of the geophones and wire deployment for monitoring fall of grounds (FOG) at Lonrho Eastern Plats belt 2.....128
Figure 5.7 Two consecutive seismograms before and after the fall of ground on 6 May '98, recorded at 6 E 1 down-dip Lonrho Eastern Plats belt 2 129
Figure 5.8 Maximum velocities as a function of time shortly before the fall of ground on 6 May '98.....130
Figure 5.9 Sketch of a single-block rockburst. In this model, the total amount of damage, or relative slip, amounted to 9 mm. 131

List of tables

Page

Table 3.1 Maximum velocities as a function of charge mass and numbers of holes, according to the Equations 3.1, 3.2, and 3.3.....36

Table 3.2 Source parameters used to model the blast in the tunnel experiment. Initial estimates of these parameters did not match calibration data, from which other parameters were derived.....39

Table 3.3 Explosive Charging Details and Estimated Energies. 46

Table 3.4 Firing times.....46

Table 3.5 Velocities obtained from the blasting. 50

Table 3.6 Measurements of displacement from 7 fragments, clearly visible on the frame.....52

Table 3.6 (continuation) Measurements of displacement from 7 fragments, clearly visible on the frame. 53

Table 3.7 Equations for the fitted curves in Figure 3.10 The slope of each line is the average fragment ejection velocity in m/s. 55

Table 3.8 Dilation readings in mm at six extensometer stations. 66

Table 5.1 Spectral peaks from the vertical borehole array (Portable Seismic System data). The peaks without letters indicate that amplification was observed at all geophones, letter D or C indicates that the peak was observed only at that particular geophone. 116

Table 5.2 Spectral peaks observed at the skin of the hangingwall channels 2, 3 and 6; the peaks are marked by the symbol " * ". 119

Table 5.3 A number of possible inclusion thickness H and length 2L, for a resonance frequency of 160 Hz. 123

1 Introduction

Rockbursts are a major hazard in South African mines, accounting for as many as 100 fatal accidents annually. This project seeks to investigate the cause and effect of these rockbursts i.e. the source and damage mechanisms.

The objective is to improve worker safety through a better understanding of mine excavation response to rockbursts. The improved understanding should lead to more effective mine layouts and support design.

The project is an extension of GAP 201 and consists of two main enabling outputs namely:

- a comprehensive investigation of rockbursts posed a hazard to workers

- measurement and analysis of the dynamic response of the rock surrounding excavations to seismic shaking

There are a number of source and damage mechanisms at work and the severity of the damage resulting from a rockburst varies greatly depending upon a variety of factors. These factors are examined in some detail under both of the above mentioned enabling outputs.

1.2 Project outputs

The primary outputs of the project are criteria and guidelines that will ultimately be used to reduce the rockburst hazard through the improved design of support systems and excavations. Other outputs include:

- design criteria for support elements such as props, tendons and bolts based on measurements of the dynamic response motion (acceleration, velocity, displacement, duration and frequency of shaking, etc) of the rock surrounding stopes and tunnels following a seismic event

- techniques for analysing the site response
- calibration and validation of computer programs used to model the dynamic behaviour of rock, such as WAVE and ELFEN
- evaluation of existing guidelines and criteria for layout, support, numerical modelling, seismic hazard assessment (e.g. Industry Guide to Methods of Ameliorating the Hazards of Rockfalls and Rockbursts, COMRO, 1988), based on the findings of detailed investigations of rockbursts
- Evaluation of the implementation of existing knowledge and technology by mines
- dissemination of the detailed findings of rockburst investigations, including recommendations of practical measures to prevent the occurrence of similar rockbursts or to limit the damage caused by rockbursts, through reports to the mine on which the rockburst occurred
- dissemination of the general knowledge gained through rockburst investigations through the new Rockburst Handbook and industry seminars

1.3 Research Methodologies

The first enabling output involved comprehensive investigations of at least four rockburst accident sites. The investigation by a team of specialists typically encompassed an assessment of the rockburst. While the details of each investigation may differ from case to case, the general procedure outlines below were followed:

- conduct site visits by a team of specialists (support, layout, geology and seismology) as soon after the event as practical
- mapped the local geology and rock mass condition (joints, fractures) measure the size distribution of the ejected rubble, asses the performance of support elements and systems, study the source parameters of the seismic event, and determine the source mechanism
- review the seismic history to determine whether there were any indications of increased seismic hazard, assess the layout, in particular, design parameters such as ERR and ESS
- test support elements such as elongates or hydraulic props

The second enabling output involves the measurement and analysis of the dynamic response of the rock surrounding excavations to seismic loading. The following procedures were involved:

- install ground motion monitors in stopes and tunnels
- adapt or develop techniques for analysing the data (e.g. from earthquake engineering methods)
- conduct of a controlled seismic source (simulated rockburst) to augment the findings
- assessment of the influence of support elements on the site response

1.4 Structure of the report

Section 2 covers the rockburst site investigations. Those completed during the course of this project have served to highlight certain problem areas, which are discussed. The full report on each investigation is given in an addendum. In section 3 the highly successful simulated rockburst experiment is described in some detail. A section follows this describing the other aspects of the dynamic behaviour. Section 5 then covers the new interpretation techniques and developments.

2 Rockburst investigations

2.1 Introduction

The requirement for the project GAP 530 was that at least four rockburst investigations be carried out. The methodology followed was identical to that for GAP 201 outlined in Durrheim et al, 1997. Five such investigations were completed. Work on the sixth in the list is presently in progress:

1. Rock engineering aspects of the rockburst at No. 11 Shaft, Impala Platinum Mine, 31 December 1997 (Durrheim et al., 1998).
2. Rock engineering aspects of the rockburst at Western Deep Levels South Mine on 7 January 1998 (Spottiswoode et al., 1998).

3. Hartebeestfontein No. 4 Shaft. Rock Engineering aspects of the rockburst accident of 5 March 1998 (Hagan et al., 1998).
4. Follow-up visit to the area affected by the rockburst at Elandsrand Gold Mine (Deelkraal Section) on 7 May 1997 (Hagan et al., 1998).
5. Investigation of damage to 64B West haulage at the great Noligwa Mine due to a seismic event of magnitude 3,7 on 21 August 1998 (Haile, 1998b).
6. Investigation of the rockburst accident of 2 October 1998 on 102 and 106 levels at Western Deep Levels West Mine (the report is still in preparation).

In addition to the above a further five rockburst sites were investigated (Turner, 1998):

- Western Deep Levels East Mine. 120 level W5 panel (two visits).
- Western Deep Levels East Mine. 83 level W3 panel.
- Western Deep Levels East Mine. 101 level E1 panel (two visits)
- Western Deep Levels East Mine. 102 level E4 panel.
- Western Deep Levels West Mine. 101 level N1 and N2 panels (two visits).

The findings resulting from 28 accident site investigations are described in Durrheim et al, 1997. A study of the additional sites listed above in combination with these initial findings has served to highlight certain aspects of the rockburst phenomenon including important problem areas that need to be addressed.

A number of source and damage mechanisms were postulated. Examples of the most common seismic source mechanisms are described in some detail. In some cases the source mechanism can be determined with a high degree of certainty.

Numerous rockburst damage mechanisms are listed. Some of the investigations are described in more detail to illustrate problem areas that apply widely in the mining industry. These are:

- A lack of knowledge of the stress fields affecting a particular area.
- An underestimation of the extent of the unstable zone surrounding tunnels.
- Poor condition of tunnel support elements due to corrosion.
- Siting of tunnels in areas of fault loss and tunnels intersecting faults at oblique angles
- Ineffective gully support design and implementation.

- Shape of remnant pillars.
- Backfill usage.

2.2 Source Mechanisms

The source mechanism, in most cases, was diagnosed as a seismic event resulting from slip on either a fault or dyke contact. Other mechanisms including remnant pillar failure, pillar foundation failure and face bursts.

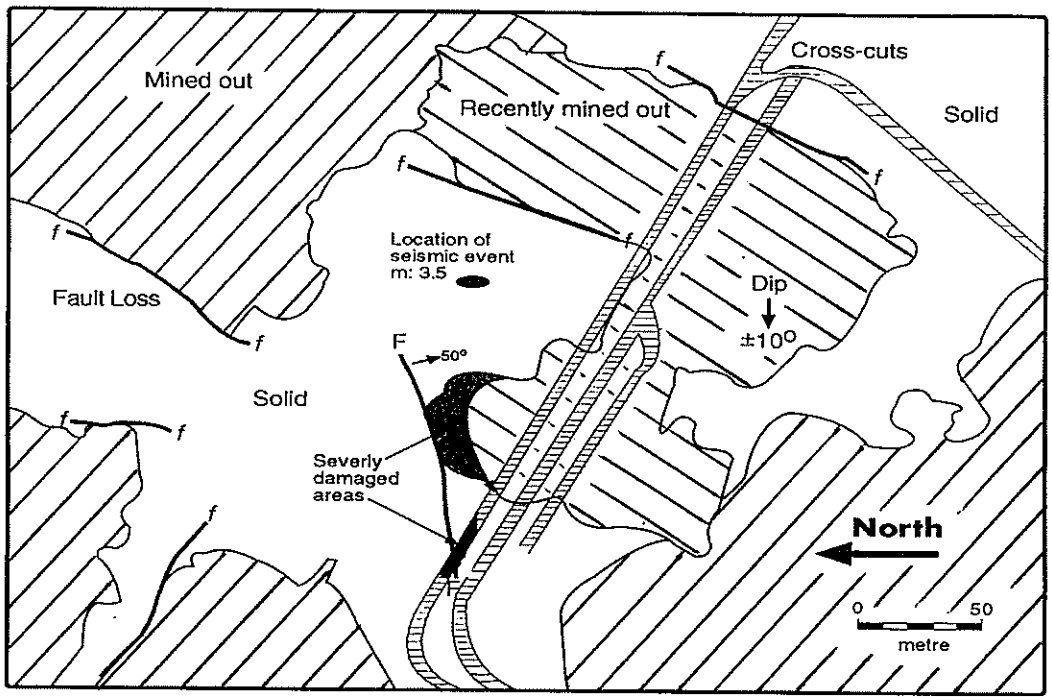

Figure 2.1 Plan of rockburst site of Hartebeestfontein Gold Mine.

In some cases the source mechanism was determined with a high degree of certainty. A case of fault slip is illustrated in Figure 2.1, where a plan of the rockburst site of Hartebeestfontein Gold Mine, in the Klerksdorp Goldfield, is depicted (Hagan et al., 1998).

The reef is extensively faulted, and dips approximately 10 degrees to the West. The area labelled as 'recently mined out' was previously left solid to protect the crosscuts

shown. A seismic event, with local magnitude of M_L=3,5 was located approximately 70 m in the footwall at the plan position shown in Figure 2.1.

The following evidence pointed to the fault marked 'FF'as the source of the seismic event:

- The location of the event was in the footwall beneath the recent mining on what could be the extension of the fault plane marked FF. The fault plane dips 50 degrees to the south.
- Seismic data, in the form of a moment tensor solution, indicated that a plane with the attitude of the fault FF would have been the most likely plane of slip.
- Damage in the crosscut was most intense at the intersection of the fault with the crosscut and took the form of fractured sidewall and footwall particularly on the north side of the tunnel. The severity of the dynamic loading in this area was evident when it was noticed that spare rails stacked on the north side of the tunnel had been moved underneath the previously installed sleepers.
- Closure was most evident in the panel closest to the fault. Timber and composite timber/brick packs were badly damaged.
- Rapid yielding hydraulic props had punched into the footwall indicating the possibility of dynamic loading in excess of 3 m/s.

Figure 2.2 illustrates another source mechanism, namely pillar foundation failure. The section is that of a strike stabilising pillar in a tabular reef in the Far West Rand region of the Witwatersrand Goldfield. A two metre thick, weak argillite known as the Greenbar is situated one to two metres in the hangingwall quartzite above the reef plane. Shear probably took place along the pillar edge on a plane as indicated. Dilation owing to shearing resulted in compression and expansion of the pillar edge which, in turn, caused buckling of the weak argillite in the hangingwall up-dip of the pillar. The latter is evident in a photograph (Figure 2.3).

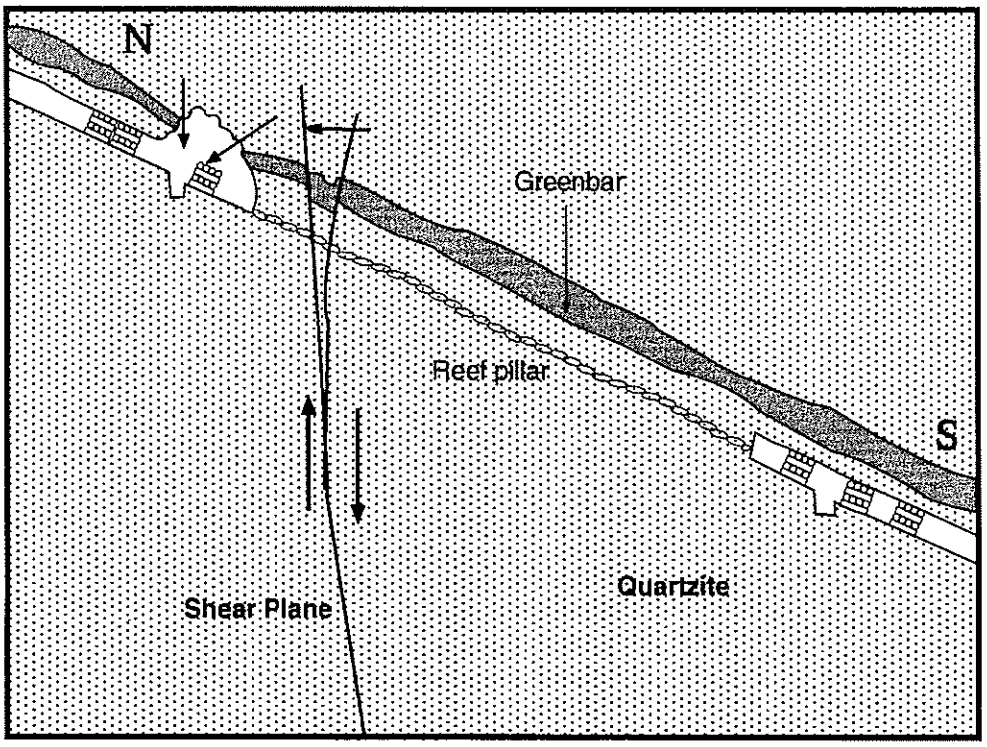

Figure 2.2 Section of a stabilising pillar with shear along the pillar edge

Figure 2.3 Buckling of the Greenbar in the gully hangingwall.

The following evidence tends to support foundation failure as a source mechanism:

- Damage was detectable along 60 m of the gully on the north side of the pillar.
- Buckling of the Greenbar was clearly visible in sections of the hangingwall up-dip of the pillar.
- The location of the main seismic event was in the footwall below the pillar.
- The moment tensor solution indicated that slip along this plane was the likely source.
- Aftershocks were located approximately on the plane in the footwall below the pillar.

2.3 Damage Mechanisms

The 34 investigations showed the most common damage mechanism to be collapse and shakedown of hangingwall. Less common were tunnel wall damage, footwall heave and face rock ejection.

Many factors affected the severity of damage. Mine layout factors included poor remnant shape, deficient pillar design, breast mining on to geological features and excessive leads or lags between panels. Incorrect input parameters such, as k-ratios when modelling also resulted in inappropriate layouts for a stress field. Tunnels positioned in fault loss zones sustained serious damage in some cases. Inappropriate and poorly designed support in tunnels, gullies and stopes and in some cases sub-standard application of the support in these excavations also played a role in determining the severity of the sustained damage.

Certain rockburst investigations served to highlight problem areas that apply widely in the industry. The areas are:

- A lack of knowledge of the stress fields affecting a particular mine.
- An underestimation of the extent of the unstable zone surrounding tunnels.
- Poor condition of tunnel support elements owing to corrosion.
- Siting of tunnels in zones of fault losses and tunnels intersecting faults at oblique angles.
- Inappropriate gully support.
- Shape of remnant pillars.

- Backfill usage.

In September of 1997 a $M_L = 4,4$ seismic event with two significant aftershocks occurred in the vicinity of East Driefontein No. 4 sub-vertical shaft. Serious damage was sustained in tunnels on four levels between 2400 m and 2800 m below surface.

The investigation served to illustrate that the in situ stress fields, in which the mining excavations are created, significantly influence the type of stability problems that can occur in an area.

Stress measurement work, subsequent to the above-mentioned activity, revealed that an anomalous stress field exists where the horizontal stress component is greater than that of the vertical. The seismic events mentioned above are now thought to be associated with slip on two major geological features in the area. Knowledge of such a stress field would assist significantly with mine design (numerical modelling) both for local and regional support.

Stacey and Wesseloo (1998) have set up a database of stress measurements made in Southern Africa over the past 30 to 40 years. Sponsored by SIMRAC the data are available and should be used by the mining industry. From the point of view of planning of mining operations, the in situ stress field is a most important input parameter for modelling of excavations. As Stacey and Wesseloo (1998) rightly point out, if the incorrect input values for the stresses are used, it is possible that the layout or other modelling, and conclusions arising therefrom may be invalid. This may have significant and adverse implications for stability and safety.

The data show that the horizontal stress orientations in the Klerksdorp area are significantly different from those in the Far West Rand and Free State regions. The data also show that the assumption of a k-ratio of 0,5 in the Far West Rand and Klerksdorp regions is not valid in most cases. The ratio varies locally and there is often a significant horizontal stress anisotropy that should not be ignored when modelling mining sequences in such areas. Programs such as MINSIM_W can accommodate the different horizontal stresses and thus provide, for example, more realistic ESS values on fault planes. Unfortunately, the degree of spatial variations in stress is poorly understood. There are therefore no well defined guidelines as to the number of stress measurements necessary or to the correct means to estimate stress when a limited number of measurements have been made.

In the investigation at East Driefontein serious damage was observed in tunnels and crosscuts in the vicinity of the No. 4 sub-shaft. The damage was owing to failure of the support system when subjected to dynamic loading associated with seismic activity.

The degree of corrosion of the tunnel support, particularly in the vicinity of faults, was high. Failure mechanisms, some of which are evident in a photograph (Figure 2.4), included:

- bulking of the tunnel side- and hangingwall
- shearing and tensile failure of rebars
- pulling out of rebars
- corrosion and consequent failure of tendons and fabric support
- failure along weak joints

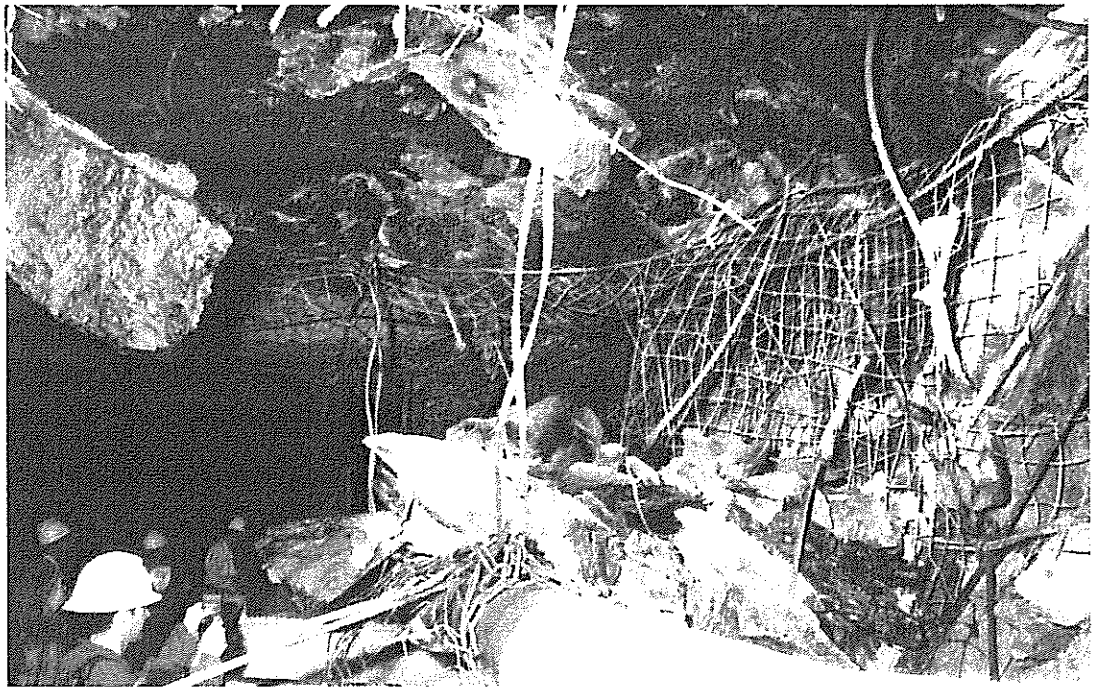

Figure 2.4 Various forms of support failure in a tunnel.

Where tunnels are needed for extended periods, and where seismic activity is likely, it would be wise to identify areas where the support system has been compromised. A systematic programme of pull tests coupled with basic observation of rock and support conditions could achieve this.

The length and spacing of tendons depends on the depth of the unstable zone and needs to be estimated. This can be done by means of petroscope observations and extensometer monitoring thus giving the extent of fracturing and dilation of the tunnel walls respectively. Extent of fallout in previous falls and rockbursts will also give some idea of the depth of instability with which one is dealing.

Other recommendations made in this particular case were:

- shotcrete before meshing and lacing to avoid adhesion and variable thickness problems
- consider injection of resin where ground conditions are exceptionally poor
- identify likely seismogenic structures from data available

The damage resulting from a local magnitude $M_L = 4,0$ seismic event was investigated in the vicinity of No. 5 Shaft at Vaal Reefs. The damage was restricted to haulages, crosscuts and gullies on 60 and 62 levels some 1900 m below surface. The Klerksdorp area is generally dominated by NE-SW striking faults, many of which have been intruded by dykes. Large seismic events are in most cases associated with these and with large bedding-parallel faults (Van den Heever, 1982). The rockburst damage was found to be largely restricted to haulages and crosscuts within a fault loss and was especially pronounced where the crosscuts intersected the fault plane and passed from overstoped to solid ground. This investigation further illustrated the need to more accurately gauge the depth of the unstable zone, which increased significantly where the crosscuts intersected the fault plane. Either the length of tendons should be increased and/or the spacing of tendons should be decreased in such situations. This has the effect of increasing the interaction between reinforcements to form a stable arch. Consideration should also be given to the shear and yield capacity of the tendons for the anticipated design environment.

One of these major faults has a history of large (M_L>3,9) seismic events. The decision to site tunnels in the loss associated with this fault was made at the start of mining. In retrospect it would appear that the siting of tunnels and crosscuts should have been avoided in those fault loss areas where extensive stoping of nearby reef was planned. Some knowledge of the stress regime and the presence of high tectonic stresses in the vicinity of some of the faults would have been useful at the early stages of planning. Slip on faults is uneven owing to variations in the type of country rock and therefore residual anomalous stresses occur in the vicinity of the

fault. As a general rule tunnels should be kept away from faults and tunnels crossing faults should not be highly stressed by mining.

In the course of this investigation it was also possible to compare the performance of two types of gully support namely timber packs and cementitious packs on the gully edges. The latter performed well and did not appear to induce additional damage to the gully sidewalls while still providing adequate hangingwall support. The opposite was true for many of the observed timber packs. The cementitious packs were designed to yield at a load lower than that required to induce damage in the gully sidewall. In addition the peak stress build-up under dynamic loading in the case of a seismic event is significantly less (probably of the order of 30%) than that of a timber pack.

A local magnitude M_L=2,1 seismic event occurred approximately 2300 m below surface at Deelkraal Gold Mine on the VCR horizon (Hagan et al.,1998). Evidence listed below points to the failure of a remnant pillar as the most likely mechanism (refer to Figure 2.6):

- Down-dip siding packs between points C and E had been pushed into the gully.
- Convergence, estimated at between 10 mm and 150 mm, was detected by means of fresh splitting of timber on packs at points A, C, D and E.
- No recent movement was evident on the fault that was exposed at point B.
- On the mining face between points F and G rock had been ejected from the face (Figure 2.6) and had in fact pushed back some of the packs in the first line. Smears of timber on the hangingwall were clear evidence of this. Note also in Figure 2.5 that the hangingwall is still intact.

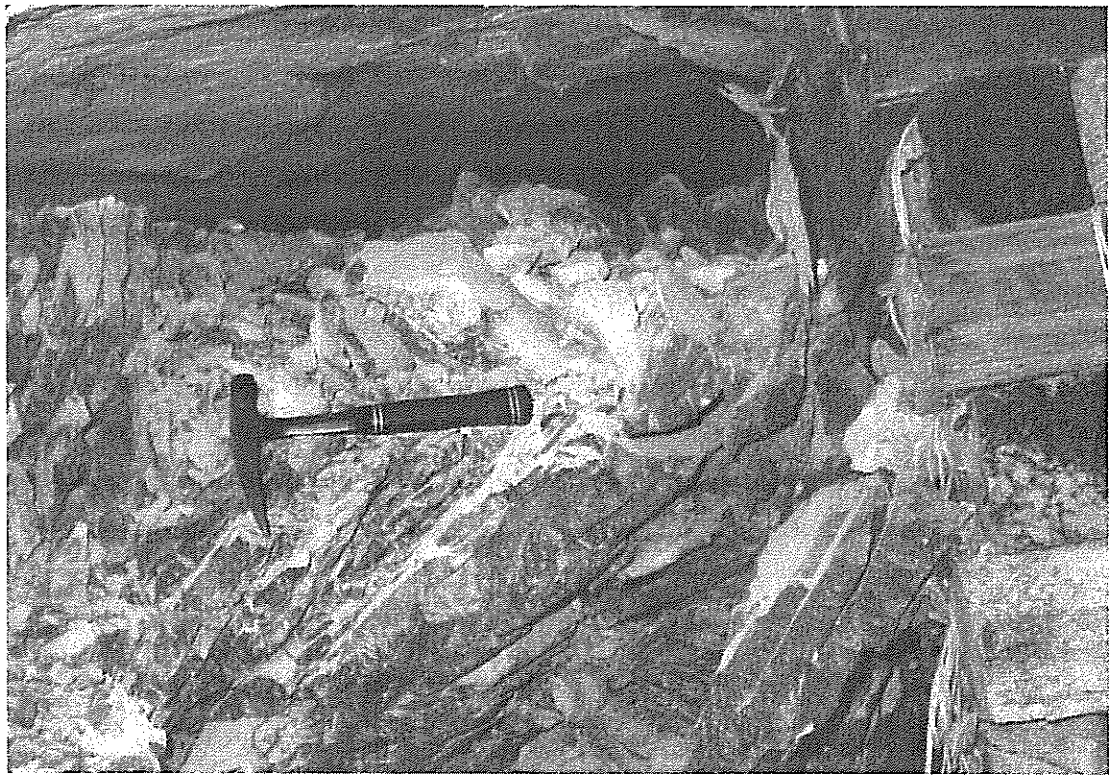

Figure 2.5 Rock ejected from the face against first line of packs.

Calculations were done taking into account the geometry of the remnant and the amount of closure observed and it was determined that a M_L=2,1 was possible assuming that the remnant failed. This and the distribution and nature of the damage led to the conclusion that this was indeed the source mechanism.

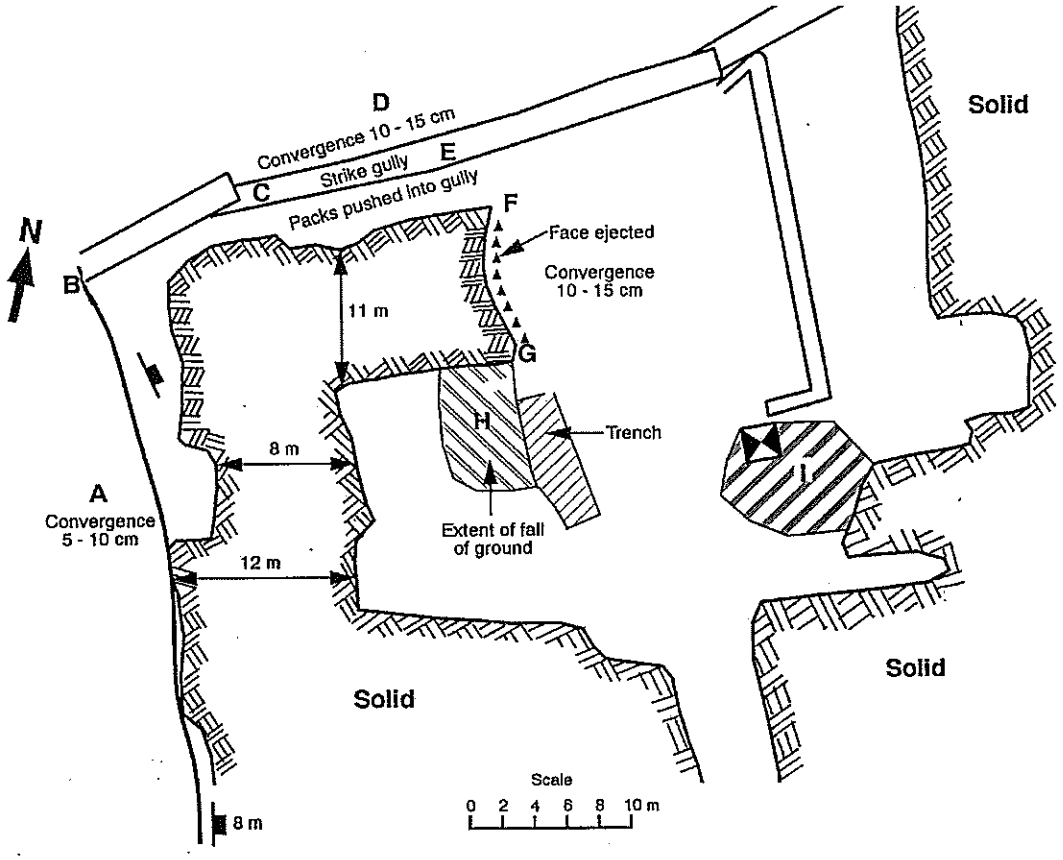

Figure 2.6 Site of the remnant pillar on Deelkraal Gold Mine.

A pillar is in danger of crushing if it is reduced to a critically small width such that a low width to height ratio leads to failure of even one limb of that pillar. In this case the L-shape was poor. Also the trench, shown in Figure 2.6, to negotiate a 2 m roll increased the effective height. The effective height may also have been increased by the presence of weak hangingwall partings in the form of bedding-parallel faults.

A stoping layout giving rise to a triangular-shaped remnant would tend to fail at the apices of the triangle leaving the core intact. In this case matters would have been improved had underhand mining been done from the raise.

Further investigations have shown that similar mechanisms could be at work elsewhere. An example is the investigation at Western Deep Levels South Mine (Spottiswoode et al. 1998), where face bursting at 2400 m below surface generated a M_L=1,4 local magnitude seismic event. A highly stressed area, again on the VCR horizon, was being mined at the time.

A seismic event of local magnitude M_L=3,3 caused severe damage to the 15W longwall at Deelkraal Gold Mine. A number of visits were made to the site by the CSIR Miningtek rockburst investigation team. The mine had decided not to use strike stabilising pillars and the regional support, designed to maintain average energy release rate values below 30 MJ/m^2, was in the form of backfill. The backfill was generally well placed and dip gullies in the back areas had remained open enabling easy access to the stopes. Nevertheless a fair amount of coseismic closure and elastic convergence was evident. The closure manifested itself by buckling elongate support on the face and by breaking of timber poles that had been installed to restrain the backfill, as far back as 40 m in the back area (Figure 2.7).

Figure 2.7 Closure on backfill in the back area.

The Industry Guide (1988) states that for mines extracting extensive (>1000 m span) blocks of ground at depths greater than about 3000 m, backfill alone cannot achieve satisfactory regional support or ERR control. The Guide goes on to say that

theoretical studies indicate that hybrid systems of pillars and backfill combined can offer significant advantages in terms of ERR reduction. In hindsight it would have been better to have this combination at Deelkraal even though the depth of the 15W longwall is not quite 3000 m below surface. Recent results from the Anglogold mines on the Far West Rand show the hybrid systems to be effective in reducing the seismic hazard (Essrich and Amidzic, 1999).

It can be shown numerically that such a hybrid system is more effective when the stabilising pillars are orientated in a dip direction as in the case of the Sequential Grid mining system practised at Elandsrand Gold Mine. In this case, unlike the longwall system with strike oriented pillars, the backfill is placed into areas where far less closure has been allowed to take place thus rendering the backfill more effective as the span increases.

Arguments have been put forward, particularly for certain geotechnical area the Vaal Reef in the Klerksdorp area, that backfill may not be effective as a local support owing to the increased horizontal stresses that may result in an unstable stope hangingwall beam. The validity of this argument needs to be substantiated with documented evidence arising from underground observations and measurements. SIMRAC sponsored research will be attending to this requirement in 1999.

An investigation of a rockburst site on West Driefontein Gold Mine showed the positive effect backfill has on gully and stope conditions on the Carbon Leader Reef horizon. Slip on a dyke contact caused a seismic event of local magnitude M_L=2,7 that resulted in rockburst damage in four panels and gullies on a longwall 2300 m below surface. The backfill at that time covered 67% of the mined-out area but was unfortunately unevenly spread owing to operational problems. Only certain sections of the upper panels were filled and it was very apparent that the gully opposite those unfilled areas had suffered severe damage. The mechanism appeared to be shakedown of the gully hangingwall after failure of the beam. The beam length should be restricted as much as possible by bringing the backfill down close to the gully. Cementitious gully packs with 1400 kN yield force were being used. This was thought to be too strong and resulting in damage to the gully sidewall, particularly in the areas opposite the non-filled zones in the stope. Some of the packs had in fact fallen out completely. One of the recommendations was to use packs with a yield load closer to 1000 kN.

2.4 Conclusions and Recommendations

1. The most common source mechanism of a causative seismic event is slip on either a dyke contact or a fault. In some cases the seismic data coupled with the extent, nature and location of the damage allow the identification of the source mechanism with a high degree of confidence.

2. Other identified source mechanisms include remnant pillar failure, stabilising pillar foundation failure and face bursting.

3. The most common damage mechanism resulting from seismic activity is predictably, collapse and shakedown of hangingwall. Other mechanisms are tunnel wall damage, footwall heave and face rock ejection.

4. Many factors affected the severity of damage and contributed to the occurrence of violent seismic event. Mine layout factors included poor remnant shape, poor pillar design, breast-on face orientation when approaching geological features and excessive leads or lags between panels. Incorrect input parameters, such as k-ratios, when modelling also resulted in poor layouts. Tunnels positioned in fault loss zones sustained serious damage in some cases. Inappropriate and poorly designed support in tunnels, gullies and stopes and in some cases sub-standard application of the support in these excavations also played a role in determining the severity of the damage sustained.

5. Assumptions regarding the stress field affecting a particular mine are probably invalid in many cases. An improved knowledge of the stress field would assist significantly with mine layout (numerical modelling) and both local and regional support planning. It is recommended that mines make use of a database of stress measurements that has recently been established additional stress measurements may be necessary where anomalous situations are evident or anticipated.

6. The degree of corrosion of tunnel support can have a significant effect on the extent and severity of damage resulting from a seismic event. Where tunnels are needed for extended periods, and where seismic activity is likely, areas where support may be compromised must be identified and rehabilitated.

7. The depth of the unstable zone surrounding tunnels needs to be estimated. This determines the necessary/optimal length and spacing of tendon support.

8. The siting of tunnels and crosscuts in fault loss zones where extensive mining of nearby reef is planned should be avoided.

9. Cementitious packs, designed to yield at loads lower than that required to induce damage in the gully sidewall, have been seen to perform well under dynamic loading. In one case this was confirmed by a direct comparison with timber packs.

10. The stability of remnant pillars depends largely on the shape and the width: height ratio. The latter may be affected by local geology and by reef geometry. A triangular shape as opposed to L-shaped or narrow rectangular remnants, which are particularly troublesome, is recommended.

11. Backfill can be shown to have a significant regional and local support benefit in some areas particularly on the Far West Rand. The positive effect that backfill has on gully and stope conditions has been observed.

3 Controlled seismic source experiment

3.1 Introduction

Rockbursts are a major hazard in South African deep-level gold mines. Many analyses have been made and many observations of rockburst damage have been carred out. Despite these efforts, the rockburst problem is far from solved.

An artificial rockburst experiment was conducted as a part of this project with the collaboration of GAP 335. An attempt was made to simulate a seismic event by means of a large blast in solid rock close to a crosscut. The idea was to instrument the resultant "rockburst" site in order to gain further insight into the damage

mechanisms involved. An experiment site was set up in a disused crosscut on 53 level (1600 m below surface) on Kopanang Mine previously called Vaal Reefs No. 9 Shaft. The experiment involved a designed source, a fairly dense array of seismic monitoring, extensometer measurements, petroscope observations and study of rock mass condition (fractures, joints, rock strength etc.). Knowledge of the site before and after the experiment was gained using ground penetration radar and seismic measurements.

Earlier attempts at this experiment were unsuccessful and success was only achieved in the middle of September 1998, three months before the end of this project. The quantity and quality of the data exceeded our initial expectations, and more time was required to complete these analyses. The following document is therefore incomplete and it is hoped that further opportunity will arise for a more detailed analysis.

3.2 Test site and instrumentation

The site is situated at Kopanang mine (9 shaft), Vaal River Operations at the 53 BW23 X/C South. The crosscut is 2118 m below datum or 1600 m below surface.

The lithologies in the crosscut comprise argillaceous quartzites of the Strathmore Formation known locally as the MB2. The quartzites are grey, medium grained and argillaceous. The bases of individual beds are coarser, defining an upward fining sequence. Each bed is usually capped by a dark green argillite up to 5 mm thick. Bedding is generally planar with thicknesses ranging from 50 mm – 500 mm. Black argillite lenses occur locally within the quartzites and are laterally impersistent.

A N-S trending normal fault dipping 72^0 to the east occurs 10 m NW from the site. The fault has a throw of over 100 m downthrow to the east. The lithology encountered in the crosscut is thus hangingwall strata of the Vaal Reef. There is some evidence of strike slip movement on the fault.

The site was located in an unused crosscut that was intersected by a crosscut. Five blast holes were drilled from the crosscut in a direction parallel to the crosscut. The charged portion of the holes was about 6 m from the tunnel sidewall. The holes were

drilled in a vertical plane with the collars about 500 mm apart. The purpose of this design was to exclude gas expansion as a direct source of rock ejection. Figure 3.1 illustrates the underground layout and deployment of seismic sensors.

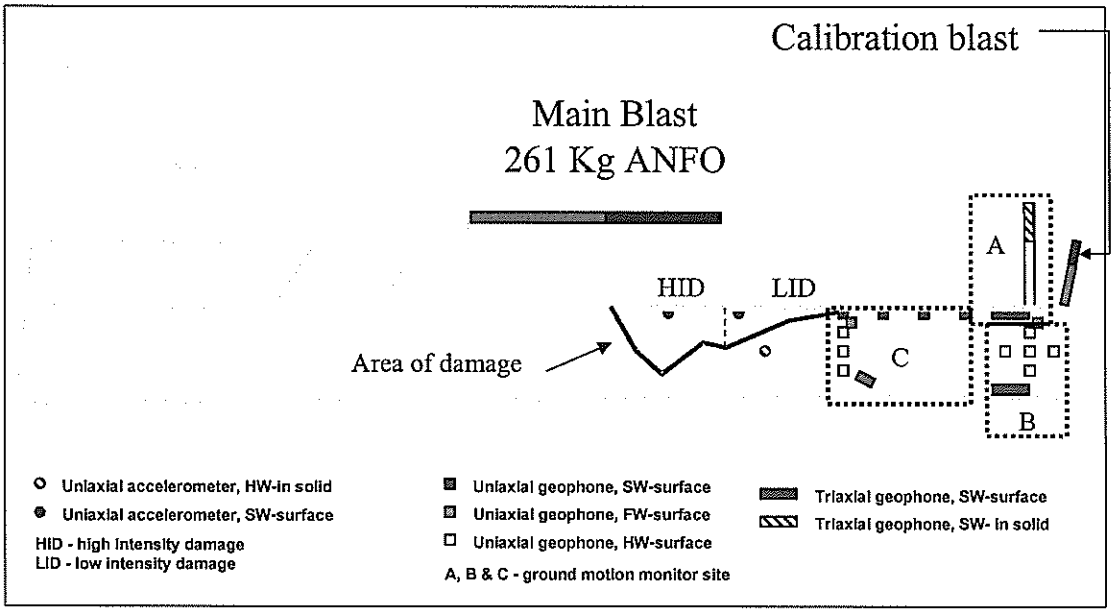

Figure 3.1 Controlled seismic source experiment layout and deployment of the seismic sensors.

Three accelerometers PCB 305A04, shock type, were installed close to the projection of the blast on the tunnel wall. Two of them were placed on the sidewall closest to the blast in the area of maximum expected damage and the third one was installed in a nearby borehole 3 m deep into the hangingwall.

The output from the accelerometers was conditioned using in-line amplifiers set at 1 x times gain. A Speedwave, 4 channel, high-speed digital recorder was used to record the signals. The recorder has a 12 bit resolution and was set at a voltage range of ± 10 V and a sample rate of 500 000 samples per second.

Three 8 channel ground motion monitors were installed along the tunnel at the both sidewalls, the hangingwall and the footwall. Vertical, horizontal and triaxial boats, installed on the skin and into a borehole were used to supply maximum seismic coverage. see Figure 3.1.

Additional measurements of tunnel deformation before and after the experiment were done using extensometers, ground penetration radar and routine geological

techniques such as fracture mapping, assessment of the existing faults and joints and petroscopic observations. Rock ejection velocities during the blast were filmed using a high-speed video camera.

3.3 Calibration blast and pre-blast monitoring

Preliminary modelling and the use of empirical equations for calculation of peak particle velocities gave large variations in expected peak particle velocities. It was therefore decided to perform a small calibration blast.

The blast was conducted into the blasting wall close to the last set of geophones (see Figure 3.1). A horizontal hole, 0,37 mm in diameter drilled 75^0 towards the end of the tunnel was charged with five cartridges Powergell 816 with 0,12 kg each equivalent to 0,66 kg ANFO. The 0,65 m length charge was stemmed with 1,15 m clay. The estimated Velocity of Detonation (VOD) was 4500 m/s.

The measured values of PPV's from this blast are shown in Figure 3.2.

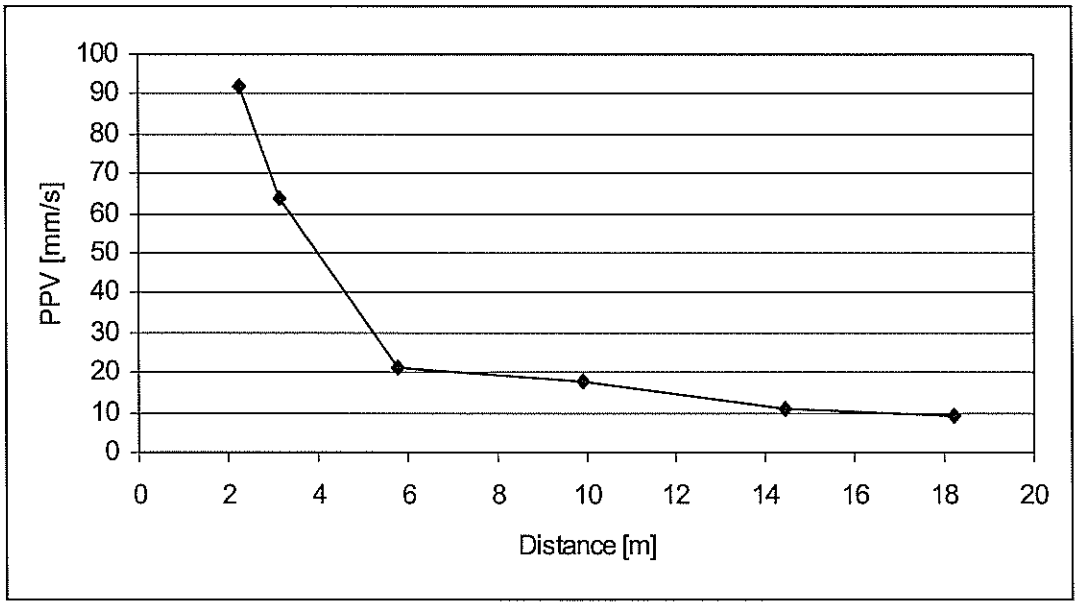

Figure 3.2 Attenuation curve of peak particle velocities measured from the calibration blast.

The attenuation of maximum velocities for the calibration blast $Y_{(R)}$ as a function of distance R was derived as:

$$Y(R) = C' \frac{1}{R^{1.1}} \qquad (3.1)$$

where: *C"* is a constant proportional to the charge mass.

It was important to estimate the parameters of the main blast and predict the position and the value of maximum velocities on the blasting wall. The charge mass of the calibration blast, Powergell 816, was converted to the equivalent mass ANFO, using 1,1 convergent coefficient. Then the peak particle velocity was estimated as a function of the charge mass Q and the distance R. The following equations have been suggested by Rorke (1998), for far field:

PPV = 1143(R/(Q^0,5)^-1,6 (3.2)

where: *R* is a distance in *m* and *Q* = *Charge mass* in *kg*

Another equation for far field measurements was given by Ouchterlony et al, (1997):

PPV = 650(R/(Q^0,5)^-1,42 (3.3)

Persson and Holmberg, (1990) have scaled the equation (3.2) for the near field using a scaling factor f = [atan(H/2R)/(H/2R)], where and H is a charge length in *m*:

PPV = 650(R/(fQ^0,5)^-1,42 (3.4)

The maximum velocities in respect of the number of holes and the charge mass for 5 m long holes were calculated using Equations (3.2), (3.3) and (3.4) and the results are listed in Table 3.1

Table 3.1

Maximum velocities as a function of charge mass and numbers of holes, according to the Equations 3.1, 3.2, and 3.3.

	Charge Mass	Rorke Far Field	Ouchterlony Far Field	Persson & Holmberg Near Field
1 Hole	40	1664,72	907,48	861,91
2 Holes	80	2898,45	1484,46	1409,91
3 Holes	120	4009,03	1979,68	1880,26
4 Holes	160	5046,50	2428,29	2306,34
5 Holes	200	6032,79	2845,16	2702,28

However, these equations are empirically obtained and are based on site-specific measurements. For more accurate estimation of the maximum velocities numerical modelling was needed.

3.4 Numerical modelling for planning the main blast and expected velocities

A more detailed coverage of numerical modelling of this experiment is given in the GAP 332 final report (Napier et al., 1998). Numerical modelling was used both in a forward sense in the design phase, as well as for back analysis to develop an understanding of wave interaction with tunnels.

Source Model

A numerical source was required which would model stress waves emanating from a propagating blast in a borehole, to a distance many times larger than the borehole radius. (In the experiment, the borehole charge lengths were from 4 to 7 m and the borehole diameter was 0,1 m. The tunnel was more than 5 m away, and geophones were located up to 25 m ahead of the blast). A three-dimensional numerical model with this volume of interest required as coarse as possible a representation of the

source to be developed. i.e. it would be pointless to model the borehole in any detail, and ideally the source diameter should require just a single element.

The assumed model was one of a moving radial load applied to the surface of a borehole, where the position of the applied load moves along the axis of the borehole with a certain velocity of detonation (VOD). Through comparisons with an analytic solution for this source model (Kouzniak, 1998; Kouzniak & Rossmanith, 1998), it was found that the source could be represented numerically as a volumetric source without the explicit representation of a borehole, and coarsely, with a single element width corresponding to the borehole diameter. Comparisons made showed that the coarse numerical source corresponds accurately with the analytic source. It was also observed that this source generates shear waves owing to the non-uniform loading of the borehole surface, and that for VOD < Cp, the shear wave is dominant (Napier et al, 1998).

Forward modelling of the experiment using this source model

An approximate representation of the tunnel experiment was made in the program WAVE (Hildyard et al, 1995). A true 3D cavity was not available to simulate the tunnel, and an approximation was made - the free surface conditions of the different tunnel faces were modelled accurately, while the corners of the tunnel were poorly represented. Forward numerical modelling was used to aid in the design of the experiment, to give insight into which measurements were likely to be the most useful, and insight into the positions where recordings should be made. The following questions were identified:

- Can the experiment be tailored to simulate waves from a mining-induced seismic event?
- Where is the expected position of maximum damage?
- How quickly do the motions die off with distance along the tunnel?
- How much damage can be expected on the other walls of the tunnel?

The maximum particle velocity on the tunnel sidewall was found to depend on the following:

- The maximum borehole pressure: This is the assumed maximum pressure reached at the walls of the borehole. The maximum velocity in the models is linearly related to this pressure.

- The rise-time of the pressure: This is the duration over which a point on the borehole wall moves from zero load to maximum load. The faster the rise time, the higher the resulting velocities. This also determines the dominant frequency of the incident waves.
- Delay between (the five) multiple blasts: The initial blast design anticipated a delay of at least 1 ms between blasts (to allow for detonation error). The modelling showed that this was too great a delay for the blasts to behave as a single event i.e. velocities at the tunnel were greatly reduced if the individual holes were detonated with large delays.

No definitive reference to aid in choosing these parameters could be found, but based on blast modelling experience, the following values were assumed to be good estimates (Daehnke, 1998). An upper maximum for the borehole pressure of 1 GPa, and an upper maximum for the rise-time of pressure at a point of 200 μs. The latter corresponds to maximum pressure reached over approximately 12 borehole radii. Pressure decay time is much longer than the rise-time and its influence on wave motions at the tunnel is negligible. Finally, the detonation method for the blast was changed to give approximately simultaneous ignition.

The preliminary modelling demonstrated that:

- Predominantly shear waves could be generated by a suitable choice of VOD.
- The position of maximum damage depends on the VOD/Cs ratio of the blast (where Cs is S-wave velocity), and the distance between the blast and the tunnel wall.
- The magnitude of the maximum velocity (at the tunnel wall) depends on the maximum borehole pressure, rise time of pressure at a point and time delay between individual blasts. Estimates of velocity magnitudes at the tunnel would be entirely dependent on meaningful estimates of these parameters.
- Estimates of motions on the other walls of the tunnel were considered unreliable, since there was not a continuous tunnel free surface in this model, with spurious stresses transmitted through the corners.

Calibration

It was important to estimate parameters such as the pressure and rise-time for the source model, and indeed to evaluate whether this source model would be valid as a representation of the blast. Accelerograms recorded very close to a blast in solid rock were available from an earlier experiment (Rorke, 1992), obtained as part of the preconditioning research project (Lightfoot et al, 1996) research project. Attempts to model these with the chosen source model were not conclusive, and velocities in models using the suggested blast parameter estimates were an order of magnitude less than the recorded velocities. Greater detail is presented in GAP 332 (Napier et al, 1998); but it became apparent that a calibration blast at the actual rockburst experimental site providing velocities at greater distances from the blast, needed to be made. Other data was available to calibrate the model in terms of empirical expressions for far-field velocities due to a blast. Table 3.2 shows the source parameters which were inferred from these calibrations, and used in different models of the tunnel experiment. Other factors which affect the model results are the material parameters. Values of Cp = 5740 m/s and Cs = 3514 m/s were used in all models, based on estimates for solid rock at the site.

Table 3.2

Source parameters used to model the blast in the tunnel experiment. Initial estimates of these parameters did not match calibration data, from which other parameters were derived.

	Source #1, from realistic estimates (Daehnke, 1998)	Source #2, from preconditioning experiment	Source #3, from calibration blast	Source #4, used in post-blast model
Maximum borehole pressure	≤ 1 GPa	10 Gpa	9 GPa	1 Gpa
Pressure rise-time	≤ 200 μs	100 μs	800 μs	800 μs
Borehole diameter	0,1 m	0,2 m	0,3 m	0,2 m
VOD		4200 m/s	4200 m/s	4000 m/s

As mentioned above, a calibration blast was set off at the site. The physical parameters, as given in Chapter 2, were: a 75^0 charge hole, 1 m from the tunnel wall, 0,65 m in length, 0,37 m in diameter and 0,66 kg in equivalent mass with a VOD of 4500m/s. The best modelling match was found with a source rise-time of 0,8 ms, a diameter of 0,1 m (3 times the physical diameter), and a peak pressure of 9 GPa. The long rise time seems necessary because of surprisingly long pulse widths in the data - this differs significantly from data from the preconditioning experiment, where pulse widths are much shorter. Two explanations are possible. The preconditioning experiment measured motions very close to the blast, and the high frequencies measured in the preconditioning experiments may attenuate rapidly to smaller values at the distances associated with the calibration blast. Secondly, the geophones had a filter at 800 Hz so that higher frequencies were not recorded for the calibration blast.

Comparisons for various geophones along the near tunnel wall are shown in Figure 3.3. Geophones C8, C3, C6 and C5 are normal to the tunnel wall starting at 5,8 m from the calibration blast, and positioned at approximately 4 m intervals.

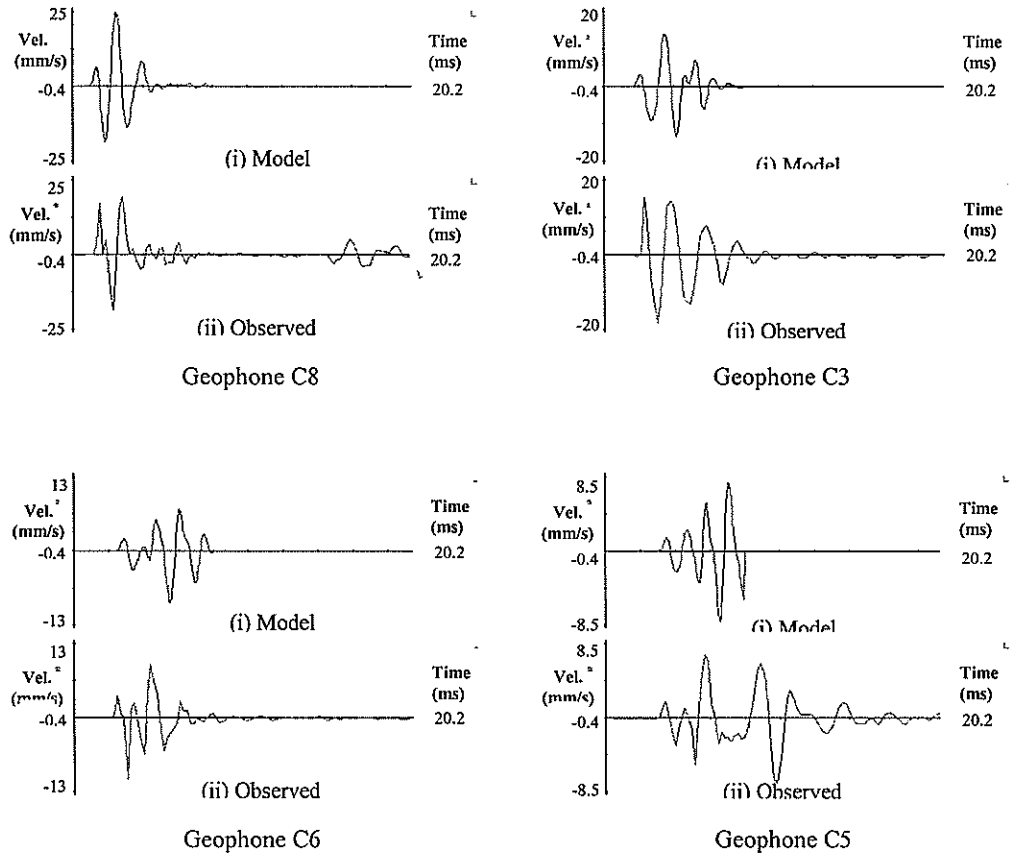

Figure 3.3 Comparison of model with geophone recordings from calibration blast, for modelled source of 9 GPa, 800 μs rise-time, step shape load and 0,1m diameter. Geophones C8, C3, C6 and C5 extended in a line along the near tunnel wall, starting at 5,8 m from the blast and in approximately 4 m intervals. Motion is normal to the tunnel wall.

Pre-blast Modelling

Although neither was ideal, two distinctly different source models were suggested from the different calibration methods. These source models were applied in a model of the final blast design before the actual blast, and later compared with the actual blast.

From the calibration blast, the source for models of the main blast (source #3) was inferred as:

- 0,8 ms rise time. (The rise-time cannot be directly inferred from the pulse width of the measured waveforms, as the VOD has an influence as well).
- Piameter = 0,3 m. (3 times that of the real source)
- Peak Pressure = 9 GPa.

This produced more realistic maximum tunnel velocities (3 m/s from a single 8 m blast hole) than the source derived from the preconditioning experiment (source #2). A surprising result was that the position of maximum velocity was no longer ahead of the blast (Figure 3.4), whereas in the earlier modelling the maximum was ahead of the blast and strongly dependent on the VOD. This was found to result from the long rise-time of the source. Although based on the calibration data, it was a much slower rise-time than what was initially thought to be realistic. If the rise-time is reduced, the maximum tunnel velocity shifts ahead of the blast again.

Variations of blast hole length and blast synchronisation were considered prior to the blast. A 5 m blast hole produced a maximum tunnel velocity of 2,3 m/s compared to 3 m/s for the 8 m blast hole. Five synchronous blasts produced tunnel velocities more than five times that of a single blast. Five asynchronous blasts, each with a 0,5 ms delay, produced a maximum tunnel velocity of 7 m/s.

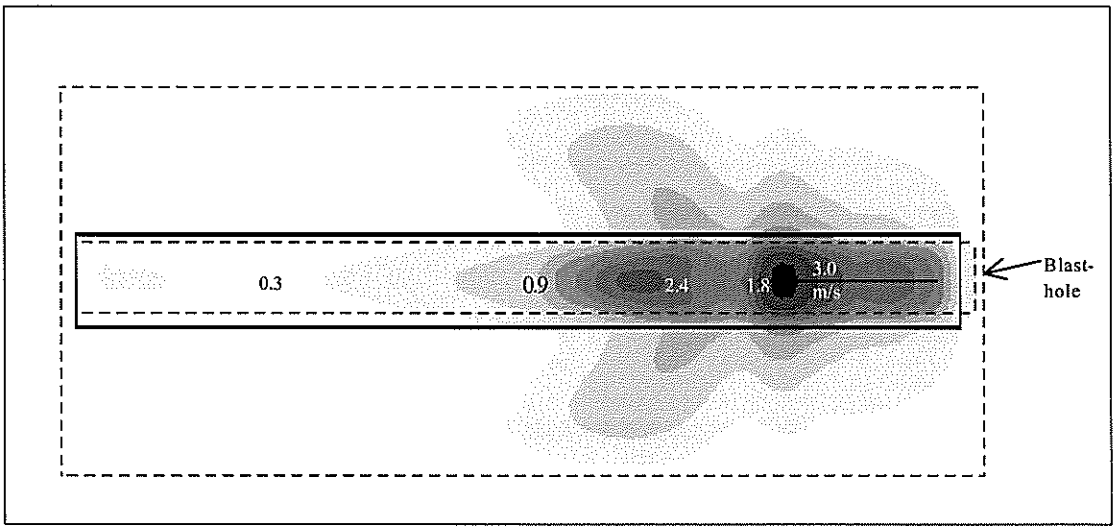

Figure 3.4 Maximum velocity on tunnel wall for pre-blast model, source # 3 9 GPa, 800 μs, step shape load and 0,3 m diameter, with a single 8 m blasthole.

Waveforms from this pre-blast model are compared with waveforms from the final blast in Figure 3.5, for geophone positions at approximately 4 m intervals along the tunnel wall. Experimental waveforms begin before the blast, so these have been shifted into approximately the same time window as the model. In the case of the experiment the maximum occurs in the initial P-wave pulse and there is virtually no S-wave, while for the model the maximum occurs later due to arrival of the shear wave. The maximum amplitudes are similar which indicates that the blast pressure is too high in the source model, since the model was for a single blast hole.

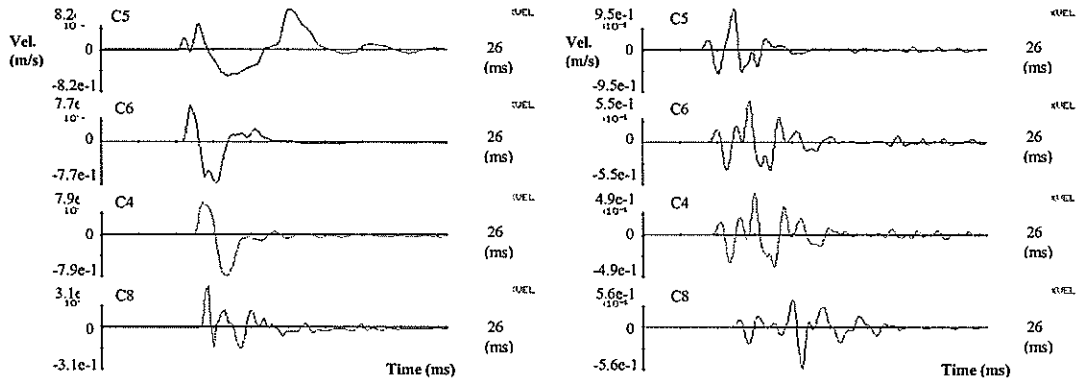

(a) Velocity recordings (m/s) from final blast

(b) Velocities (m/s) from pre-blast model, source #3

Figure 3.5 Comparison of the pre-blast model velocities for source #3 with the final blast measurements for geophones C5, C6, C4 and C8 starting at 7 m ahead of the blast, and at approximately 4 m intervals along the tunnel wall.

Post-blast Modelling

A large amount of data has been gathered from the experiment and has been partially analysed. Most of this has still to be considered from a modelling back-analysis perspective. The validity of the source model has not been established, since the predicted large shear wave is not present in the near field. A well-developed shear wave was observed in the far field at 850 m from the source Figure 3 13 (a, b and c). Nevertheless, a model was run using the final blast positions, sizes, synchronisation and recordings at all geophone positions. The borehole source was reduced to 0,2 m diameter (two times the real diameter), and the pressure to 1 GPa, with a 0,8 ms rise time. The correct lengths and positions of the five blast holes in the

final blast were represented in this model, and the modelled velocity profile along the tunnel near wall is shown in Figure 3.6. It is encouraging that velocities approaching the recorded values were obtained without the extremely high borehole pressures suggested by the calibration modelling. However, once again it was found that the shear component in the model was much greater than the P-wave component, which was not the case in the experimental recordings. One possible explanation is the complexity of the seismic signal in the near field. Both wave groups, compressional and shear, arrived at the receiver at approximately at the same time and interfere with each other. The separation of these phases is often impossible (Aki and Richards, 1980).

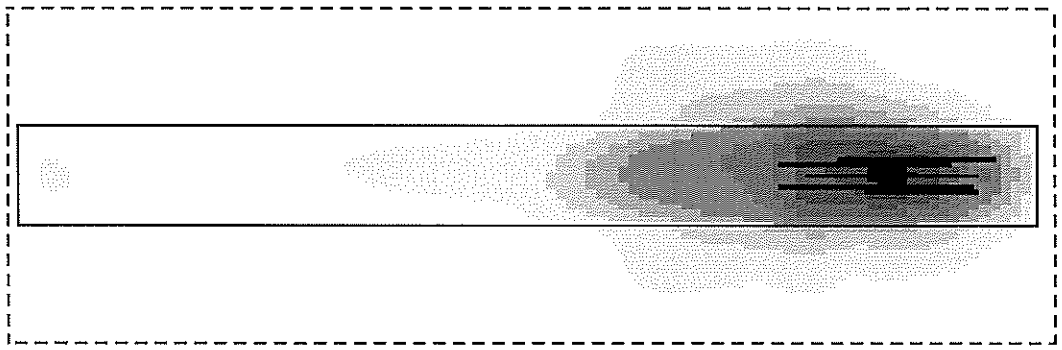

Figure 3.6 Maximum velocities at near tunnel wall for the post-blast model source #4. Maximum velocity for a blast pressure of 1 GPa is much lower than that recorded. Position of maximum velocity is now opposite the blast holes, due to the relatively long wavelength, and synchronisation of the blasts.

Conclusions

Encouraging results were obtained in the development of an equivalent source representation to a set of blast holes. 'Realistic' parameters for rise-time, borehole radius and borehole pressure produce velocities, which are much lower than velocities from available data. Nevertheless altering the source produced some encouraging waveform correspondence with the calibration data. The back-analysis of the main experiment is still in progress.

The lack of a strong shear wave in the measurements of the final blast may indicate that the source model is not valid. Two aspects are being investigated to produce

waves, which better correspond to the experiment. Work on a true tunnel cavity implementation (in case spurious waves are due to the approximate numerical implementation), and alteration of the source model or parameters which may reduce the S-wave and increase the P-wave content.

One of the anticipated advantages of modelling data from a controlled experiment is a detailed knowledge of the source so that source uncertainty is decoupled from the investigation, allowing focus on the interaction with the excavation surface. So far this goal has not been realised. An accurate source model needs to be developed for the modelling phase to be useful, possibly requiring further experiments measuring waveforms from blasts in solid rock.

3.4 Main blast

3.5.1 Source description

The purpose of this blast was to simulate a rockburst in a tunnel using explosive energy as a source. However, one fundamental difference between a blast source and dislocation type of rockburst is the effect of gas expansion. To prevent direct gas expansion causing ejection, the experimental site was chosen in a crosscut that was intersected by a crosscut. Five blast holes were drilled from the crosscut in a direction parallel to the crosscut. They were about 6 m from the tunnel sidewall over the charged portion of the holes. The holes were drilled in a vertical plane with the collars about 500 mm apart. The exact position of the holes was surveyed relative to the tunnel sidewall.

The holes were charged with 261,5 kg low density ANFO, using a compressed air loader. The explosive distribution for each hole is given in Table 3.3. The holes were stemmed with quick setting cement cartridges. The holes were initiated using 10 g/m detonating cord with two Powergell 816 cartridges acting as boosters. The booster position was located 1 m into the charge from the stemming end of the charge. Table 3.3 provides a detailed charging report based on hole length (Rorke, 1998).

Table 3.3

Explosive Charging Details and Estimated Energies.

	Hole 1	Hole 2	Hole 3	Hole 4	Hole 5
Explosive type	ANFO	ANFO	ANFO	ANFO	ANFO
Charge Mass/Metre (kg/m)	8,60	8,60	8,60	9,01	9,01
Estimated in-hole density (g/cm^3)	1,05	1,05	1,05	1,10	1,10
Length of stemming (m)	4,80	8,10	3,42	7,30	6,95
Hole Depth (m)	12,30	14,45	13,34	14,45	11,17
Hole Diameter (mm)	102	102	102	102	102
Explosive Mass Per Hole (kg)	**49,89**	**54,62**	**54,53**	**64,43**	**38,03**
Estimated explosive VOD (m/s)	3600	3600	3600	3800	3800
Estimated Energy (MJ Per Hole)	126,92	138,96	138,74	163,91	96,74
Estimated Borehole Pressure (Gpa)	2,90	2,90	2,90	3,20	3,20

Assuming that there were equal lengths of detonating cord down the barrel of each hole, the hole firing times have been calculated and are listed below. The first hole to fire was the bottom hole. The timing calculation is based on the tie-up of the cord between holes. The cord length was 0,5 m between holes and the detonation velocity of the cord was 7000 m/s. The firing times are given in Table 3.4.

Table 3.4

Firing times.

Hole 1	284 microseconds
Hole 2	213 microseconds
Hole 3	142 microseconds
Hole 4	71 microseconds
Hole 5	0 microseconds

A graphical illustration of this explosive source including length of charge, length of stemming, point of ignition and detonation times is given in Figure 3.7.

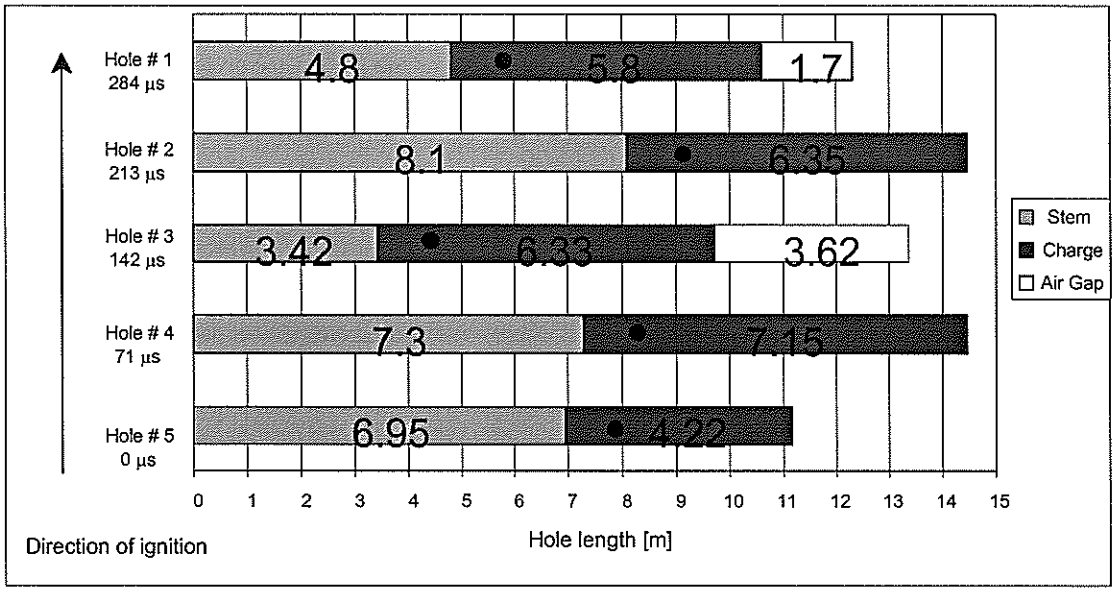

Figure 3.7 Graphical illustration of the main blast source.

3.5.2 Seismic observations in the near field

Ground velocities as measured by the accelerometers in the area of damage

Three accelerometers were installed in close proximity to the blast. Two were placed on the sidewall, close to the blast, in the area of maximum expected damage. The third was installed in a borehole 3 m in the hangingwall, to supply a measure of the waves in solid rock (see Figure 3.1). This accelerometer was also used as a reference for comparison of maximum velocities recorded in solid rock and on the skin of the tunnel.

The accelerograms recorded in this area are plotted in Figure 3.8 (*a, b*, and *c*).

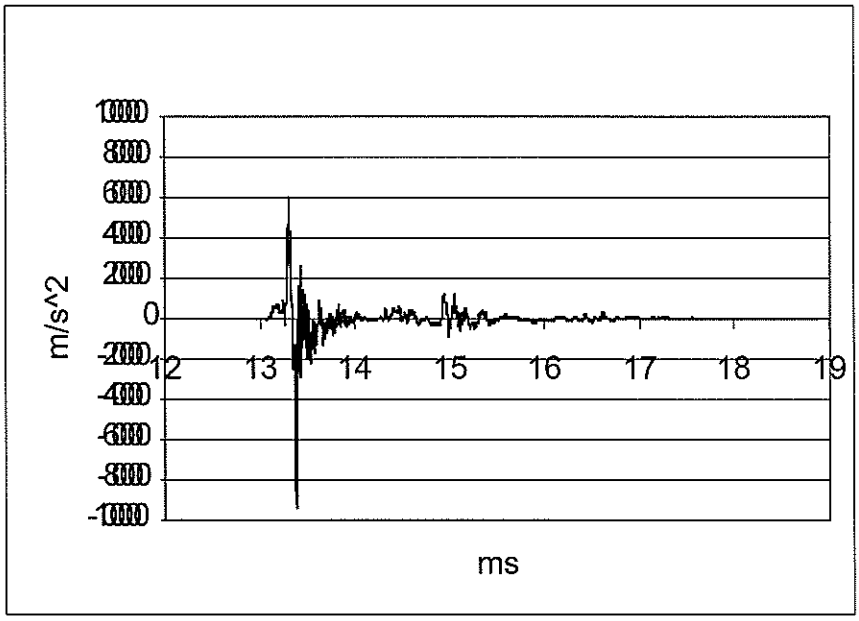

Figure 3.8 (a) The accelerogram recorded in the area of high-intensity damage. This accelerometer was ejected at 3.3 m/s.

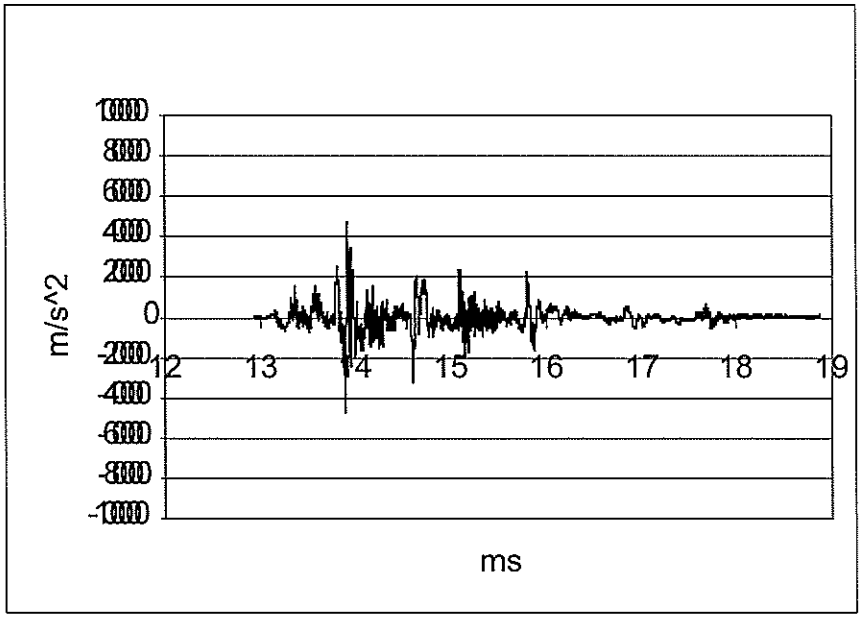

Figure 3.8 (b) The accelerogram recorded in the area of low-intensity damage.

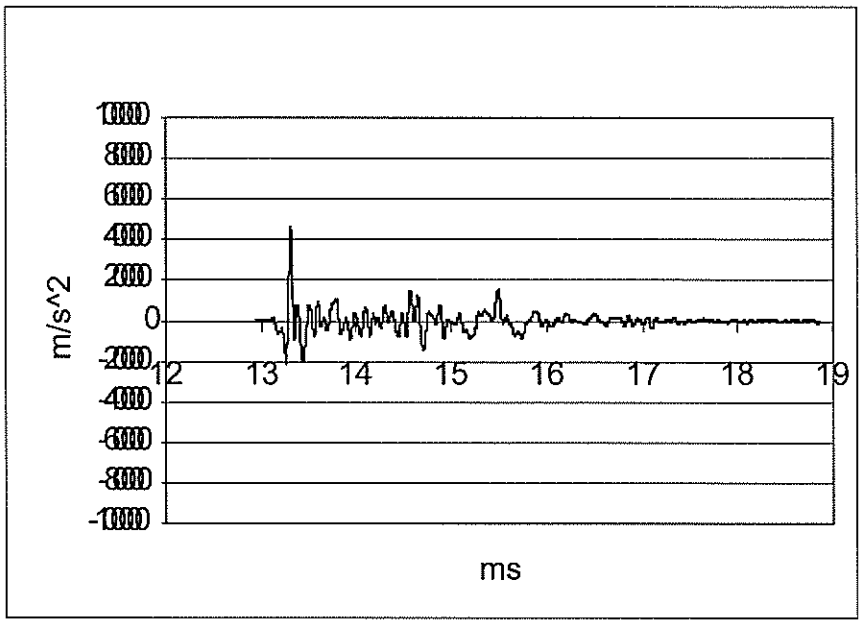

Figure 3.8 (c) The accelerogram recorded in the solid rock 3 m into the hangingwall close to the area of damage.

As the accelerograms developed a DC off-set it was necessary to perform a high-pass filter before the integration to velocity.

The accelerograms *a(t)* were integrated in order to obtain the ground velocities *v(t)* according to the following equation:

$$v(t) = \int_{t_1}^{t_2} a(t)dt \qquad (3.5)$$

Numerically the integration was performed as:

$$v(t)_t = v(t)_{i-1} + f(t)_i \delta t \qquad (3.6)$$

where: *a(t)* is the time history of acceleration, *f(t)* is a high-pass filter and *v(t)* is the time history of velocity

The peak velocities obtained from accelerometers ACT, ACM and ACH are given in Table 3.5.

Table 3.5

Velocities obtained from the blasting.

Accelerometer	Particle Velocity [mm/s]	Remarks
ACT	3328	Located in the area of high intensity damage (HID): ejected
ACM	1626	Located in the area of low intensity damage (LID): not ejected
ACH	1175	Located in the solid rock, 3 m into the hangingwall: not ejected

Ejection velocities from high speed video camera

A "Locam" high-speed camera was used to film the tunnel sidewall to measure rock fragment displacement. The camera is capable of filming at a rate of 500 frames per second. However, lighting conditions in the tunnel were not sufficient, and the frame rate had to be reduced to 200 frames per second. This frame rate provided a time resolution of 5 ms per frame.

Nine 100 mm orange coloured balls were positioned on the tunnel wall closest to the charges. They were located 1 m apart vertically and 2,5 m apart horizontally. The purpose of the balls was to provide locality information and scaling from the high-speed film.

The balls were positioned in three vertical sets of three. The first vertical set was located directly opposite the centre of the explosive charges. The second set was located in the toe vicinity of the charges and the third set was located 2,5 m farther away.

Due to the insufficient lighting, only the top two balls of the third vertical set could be seen. Displacement recordings given in the following section therefore relate to a position that is 2,5 m east of the hole bottoms.

The data from the high-speed camera was hampered by poor lighting conditions. Therefore fragment velocities could only be measured in the top eastern segment of the monitored zone.

The conventional film was converted into VHS video tape and "BMP" computer files.

Fragment velocities were measured by tracking individual fragment positions through space at intervals of 10 frames (equal to 50 ms). This was done manually by measuring displacements on the projected image and converting these to actual distances using the target ball positions for scaling. Table 3.6 provides the original measurement information and the conversion to displacement using a correction for the angle of the camera to the axis of the tunnel.

The equation used to convert from the projected image displacement distances to actual displacement distances was:

$$Displacement = (Projected\ image\ displacement \times 8{,}457)/\cos(14^0) \qquad (3.7)$$

The factor 8,457 converts from image pixels to actual distances in mm and was obtained by measuring the projected image distance between two marker balls. The angle of the camera to the north wall of the crosscut was 14^0. The correction factor $\cos(14^0)$ was applied because it is assumed the rock fragments were ejected at right angles to the tunnel wall.

Table 3.6

Measurements of displacement from 7 fragments, clearly visible on the frame.

Frame	Time (ms)	Dist (mm)	Velocity (m/s)
Ball			
0	0	0,00	0,00
10	50	57,27	1,15
20	100	105,74	2,11
25	125	96,92	3,88
30	150	88,11	3,52
35	175	185,04	7,40
Fragment 2			
0	0	0,00	0,00
10	50	42,29	0,85
20	100	0,00	0,00
25	125	0,00	0,00
30	150	0,00	0,00
35	175	0,00	0,00
Fragment 3			
0	0	0,00	0,00
10	50	35,25	0,70
20	100	70,49	1,41
25	125	39,65	1,59
30	150	0,00	0,00
35	175	0,00	0,00
Fragment 4			
0	0	0,00	0,00
10	50	30,84	0,62
20	100	66,09	1,32
25	125	123,36	4,93
30	150	0,00	0,00
35	175	0,00	0,00

Table 3.6 (continuation)

Measurements of displacement from 7 fragments, clearly visible on the frame.

Fragment 5			
0	0	0,00	0,00
10	50	35,25	0,70
20	100	74,90	1,50
25	125	110,14	4,41
30	150	0,00	0,00
35	175	0,00	0,00
Fragment 6			
0	0	0,00	0,00
10	50	66,09	1,32
20	100	114,55	2,29
25	125	35,25	1,41
30	150	0,00	0,00
35	175	0,00	0,00
Fragment 7			
0	0	0,00	0,00
10	50	123.36	2,47
20	100	70,49	1,41
25	125	52,87	2,11
30	150	0,00	0,00
35	175	0,00	0,00

The data are plotted in the curves given in Figure 3.9 and Figure 3.10. Table 3.7 provides a summary of the fitted curves.

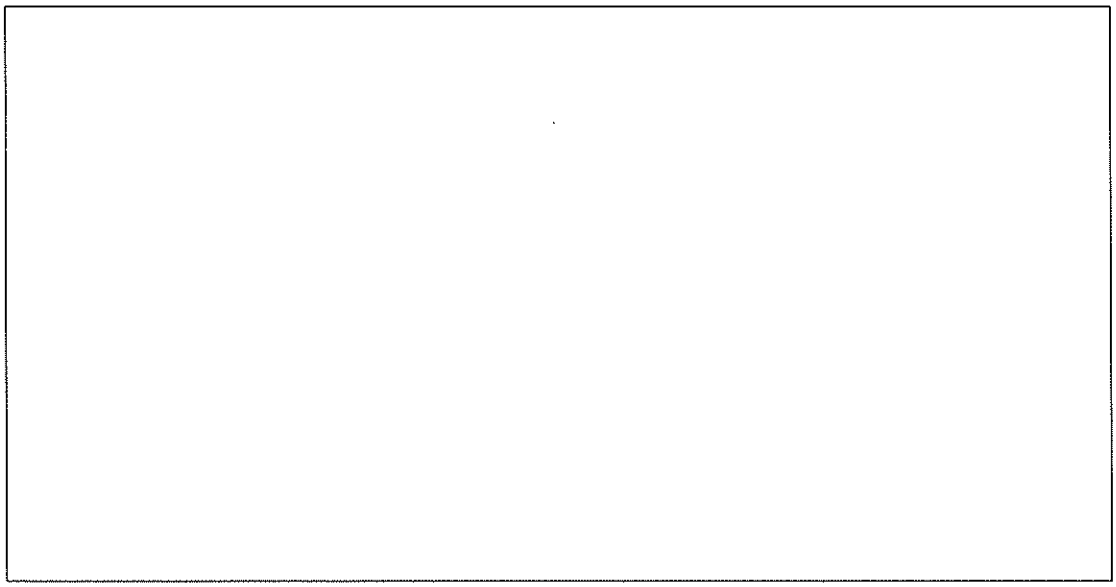

Figure 3.9 Displacement curves for six fragments and one marker ball.

It can be seen from Figure 3.9 for time later than 100 ms the measurements become random, perhaps due to the interaction of the camera with the anther particles or with incoming air wave. In Figure 3.10 all points above 100 ms has been excluded.

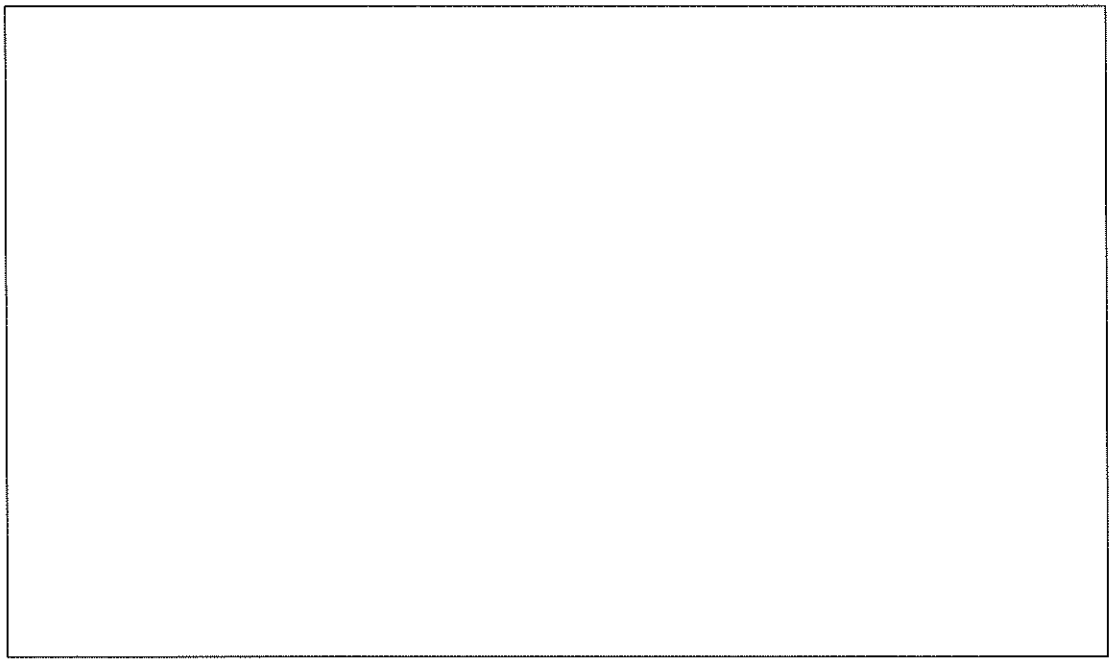

Figure 3.10 Fitted curves limited to first 100 ms of data. The second point for fragment 7 has been omitted.

The coefficients of (Y/X) in Table 3.7 is in fact the ejection velocities for each object.

Table 3.7

Equations for the fitted curves in Figure 3.10 The slope of each line is the average fragment ejection velocity in m/s.

Ball	y = 1,075x
2	y = 0,846x
3	y = 0,705x
4	y = 0,652x
5	y = 0,740x
6	y = 1,813x
7	y = 2,467x

Comparison of the PPV's measured in the solid rock and on the skin of the tunnel

Another important issue for the design of underground support resistance to rockbursts is the amplification of the seismic wave at the skin of the excavations. Previous study has indicated that the seismic wave can be amplified up to 10 times on the fractured and poorly supported surfaces (Durrheim et al. 1997).

The velocities from Table 3.5 have been scaled for the near field attenuation factor ~ $R^{-1/2}$, (Aki and Richards, 1980) and normalised to the nearest distance to the centre of gravity of the blast. The velocity obtained in the solid rock was referred to vlocities obtained at the skin of the blasting wall. A ratio of 2,2 times, between the high intensity damage area and the solid and a ratio of 1,3 times between low intensity damage area and the solid were found (Figure 3.11).

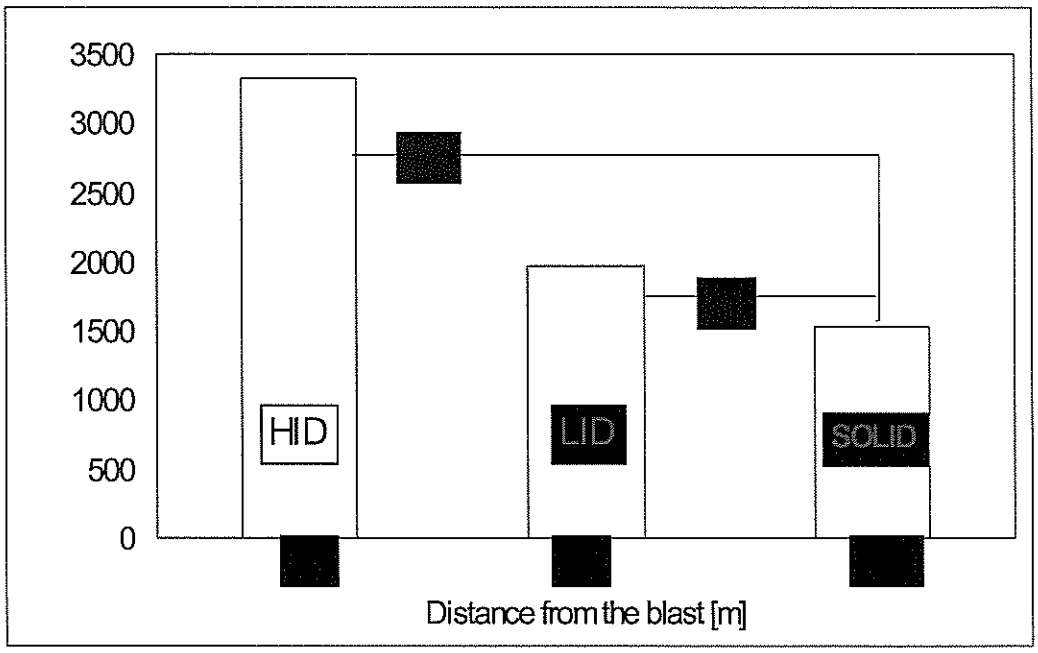

Figure 3.11 Comparison of peak particle velocities recorded in solid rock to peak particle velocities measured on the skin of the blasting wall in the areas of different degrees of fragmentation.

Attenuation of the PPV's on the blasting wall as a function of distance

The integrated accelerograms and recorded velocities on the blasting wall at sites "C" and "A" were plotted as a function of the distance. The distances have been calculated from the centre of gravity of the blast and corrected by the angle of incident *i* between the source-receiver direction and the axes of each geophone:

$$V_a = V / \cos(i) \qquad (3.8)$$

where: *V* is recorded velocity and *i* is the angle between the source-receiver direction and the axis of each geophone.

For angles close to 90^0 the values of *cos(i)* become very small, which leads to overestimation of the calculated velocities. This effect was eliminated by limiting the values of *cos(i)* to the value of the Poisson's ratio calculated for many Earth's materials. In particular for the Witwatersrand quartzite Poisson ratio was measured as ν*=0,18*.

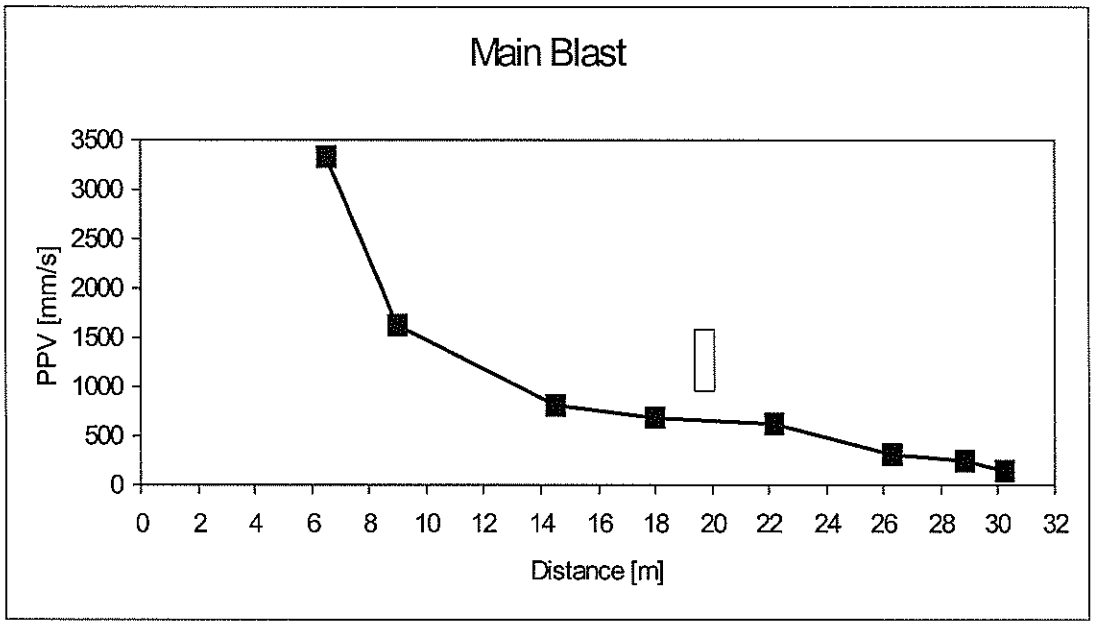

Figure 3.12 Attenuation curve of peak particle velocities measured from the main blast.

The attenuation of maximum velocities for the main blast $Y(R)$ as a function of distance R was derived as:

$$Y(R) = C' \frac{1}{R^{1.7}} \tag{3.9}$$

where: *C"* is a constant proportional to the mass of the charge.

Similar values were reported by Ouchterlony et al, (1997).

A similar attenuation was obtained from the calibration blast (Figure 3.2). The important factors such as joints, faults and number of fractures located in the path of the wave propagation have a strong effect on attenuation. These effects are discussed further in the paragraph "post-blast measurements".

3.5.3 Seismic observations in far field

The simulated rockburst was recorded at almost all stations on the Vaal River Operations regional seismic network (Finnie, 1998). The local magnitude was estimated as M_L = 1,3.

Although, there are significant physical differences in the process of seismic wave generation by blasting and dislocation source type. It was important to analyse the structure of the blast seismogram and some source parameters recorded in a far field and compare them to those generated by dislocation mining tremors located in adjacent areas.

An example of a three component seismogram of the blast recorded at about 850 m from the source is given in Figure 3.13 (*a, b* and *c*).

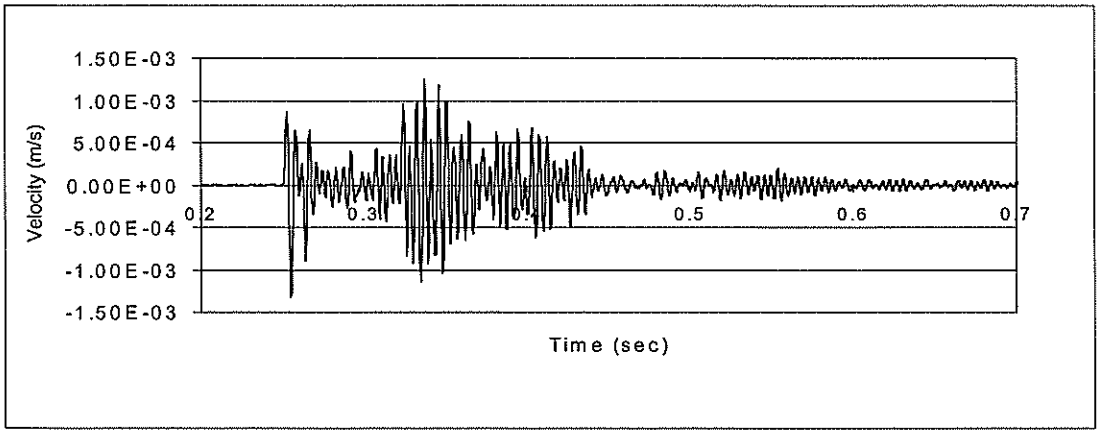

(a) The horizontal component X

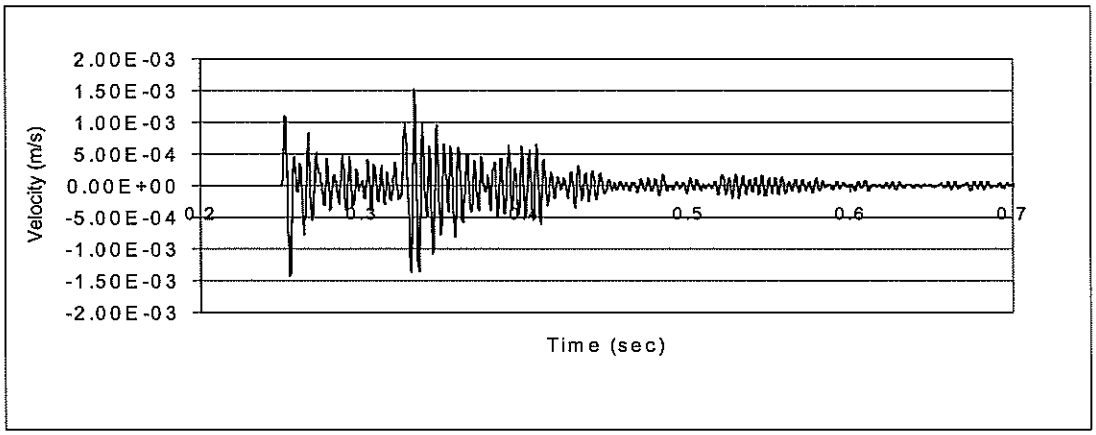

(b) The horizontal component Y

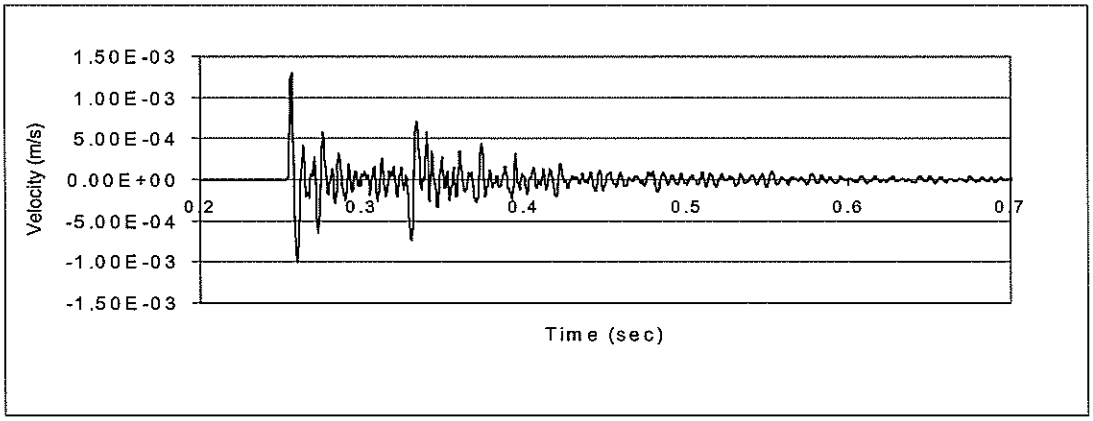

(c) The vertical component Z

Figure 3.13 (a, b, c) Three component seismogram of the blast recorded by the Vaal River Operations regional seismic network at station 850 m from the blast; a) is horizontal component X, b) is horizontal component Y and c) is the vertical component.

As can be seen from the seismograms, both body wave groups are well developed. However, the portion of the energy radiated into the P-waves is greater than the

portion of the energy radiated into the S-waves in comparison to dislocation type seismic sources (see Figure 3.14).

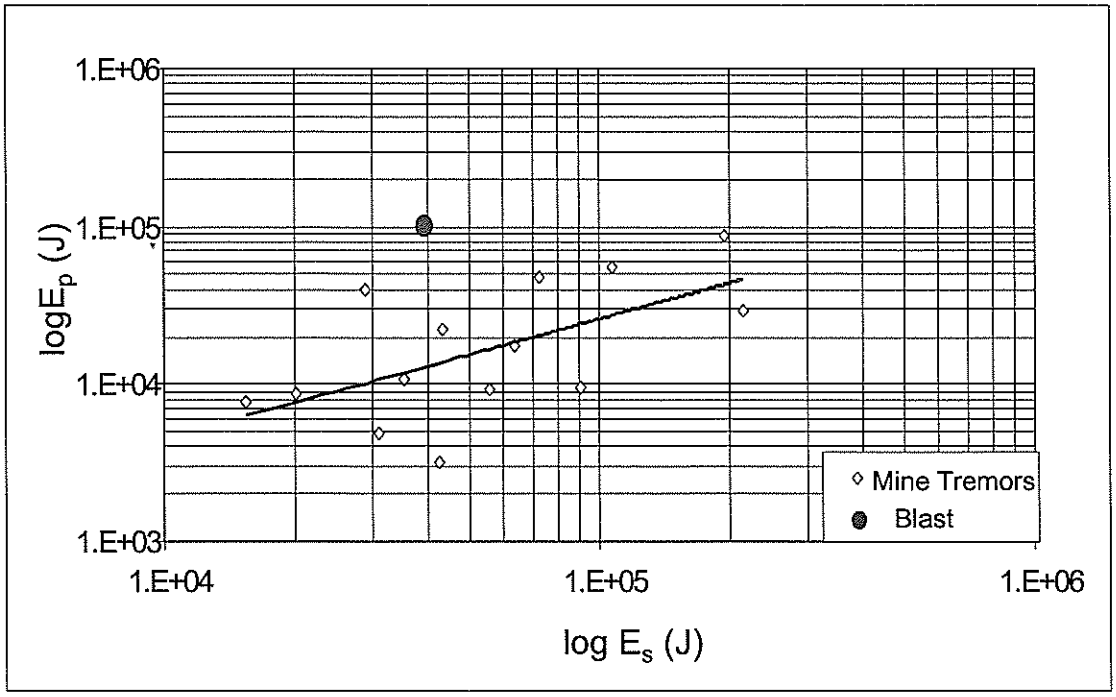

Figure 3.14 Energy emitted in P- waves versus energy emitted in S-waves for the blast and 14 mine induced seismic events located in the same portion of the mine.

An important characteristic of seismic source dynamics is the stress drop, or the difference between the state of stress before and after the rupture. Stress drop can be represented as a plot of *LogE* versus $LogM_0$. Figure 3.15 shows this relationship for the blast and for 14 induced seismic events, which located in the same portion of the mine. The stress drop is also dependent on the rise time. Faster events, like a blasting source, normally generate a smaller stress drop. It can also be seen from Figure 3.15, that the energy radiated from the blast creates a smaller seismic moment then the dislocation seismic events. However, the difference is not that great and the blast can be used for scaling of the seismic events in this region.

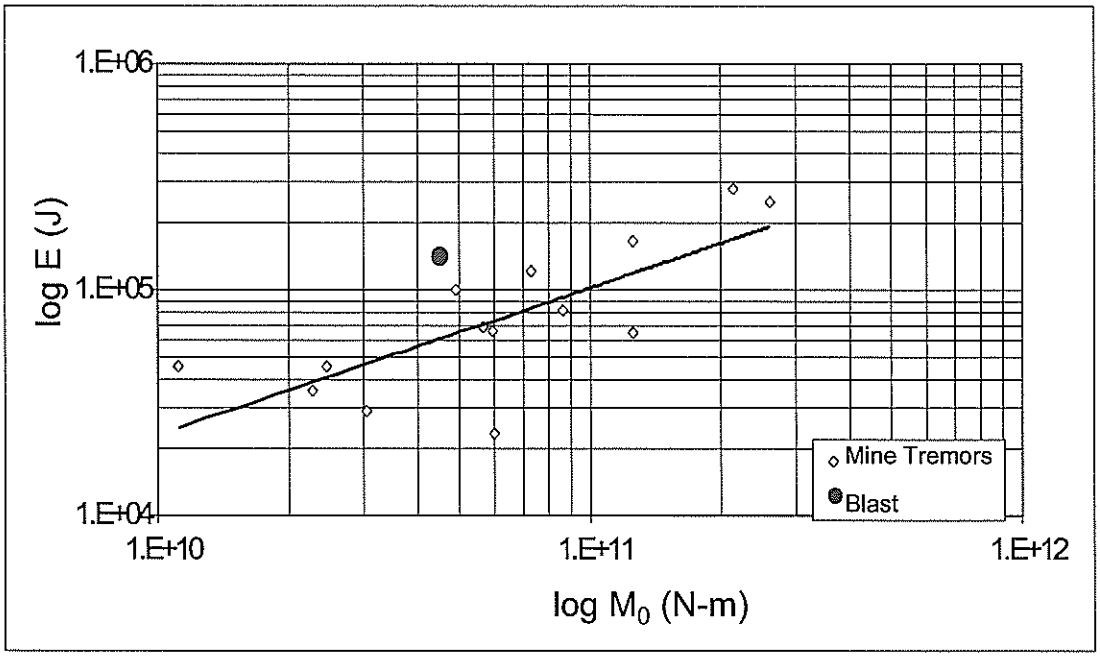

Figure 3.15 Energy versus moment for the blast and 14 mine induced seismic events located in the same portion of the mine

3.6 Post blast measurements

The site geometry obtained from the survey department is shown in Figure 3.16. The five blast holes indicated were each 100 mm in diameter and were charged as shown with a total of 261,5 kg of low density ANFO explosive. As far as was practical the five holes were detonated simultaneously. As can be seen in Figure 3.16 the holes were some 6 m from the tunnel sidewall and it is believed that the damage caused to the sidewall (Figure 3.17) was owing to blast seismic waves i.e. with no gas pressure involved, as would normally be the case. Subsequent studies of the signature of the shock waves (described later in this section) confirmed that the blast was not unlike true seismic event transient waves recorded as a result of the induced seismicity in the area. The tunnel sidewall support was 2,4 m long rock bolts on a 1 m square pattern. The mesh and lace on that portion of the wall where damage was expected had been removed prior to the blast.

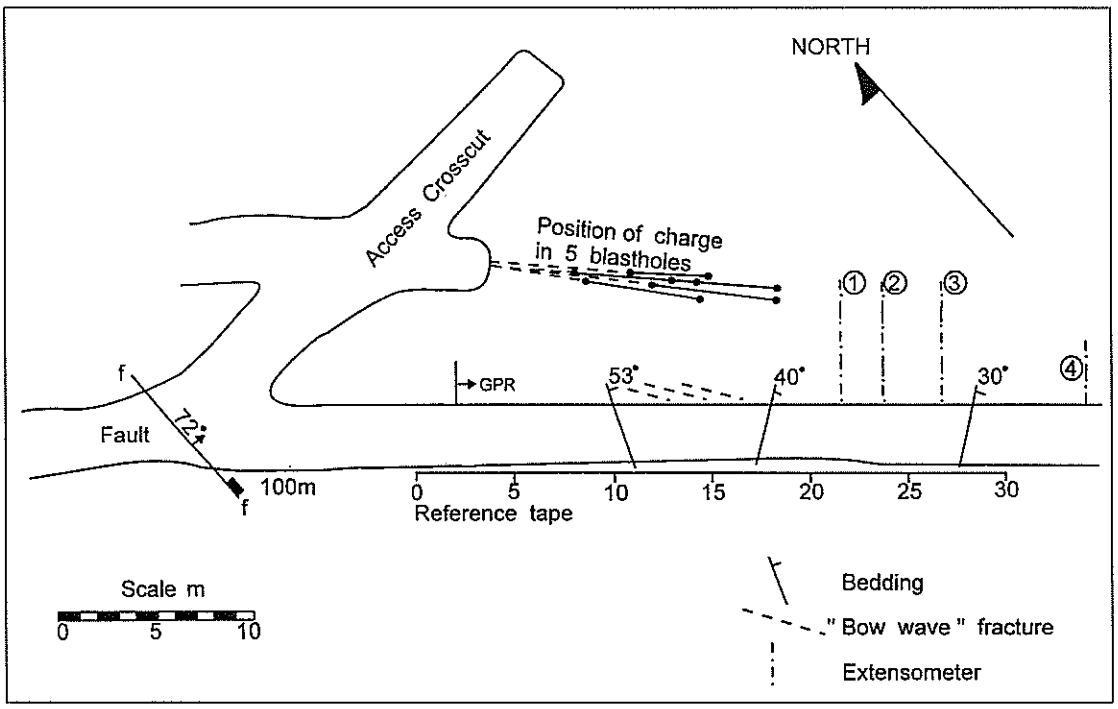

Figure 3.16 Geometry of the controlled seismic source experiment site.

3.6.1 Tunnel wall damage

It was correctly predicted that the general geology in the area and the fracturing in the vicinity of the excavation would play an important role in governing the nature and extent of the damage to the tunnel wall. Detailed mapping of the aforementioned was therefore done (Reddy, 1998).

Mining of the Vaal Reef was in progress at the time of the experiment some 100 m NNW of the site on the west side of the fault shown in Figure 3.16. This is a normal fault, dipping east and downthrowing the Vaal Reef 100 m on the eastern side. The rocks at the site are comprising the hangingwall of the Vaal Reef and are argillaceous quartzites of the Strathmore Formation known locally as the MB2.

Bedding is visible throughout the area and is generally planar with thicknesses ranging from 50 to 500 mm. Dips steepen as one gets closer to the fault, most probably as a result of drag during the faulting process.

The argillaceous quartzites are relatively weak. Three tests revealed an average uniaxial strength of 129 MPa (Drescher, 1998). MINSIM modelling showed a field stress at the site of 50 MPa, only 19 percentile than the virgin stresses of 42 MPa (LeBron, 1998). The increase is as a result of the mining mentioned earlier.

"Bow wave" fractures formed during the development of the tunnel. They define angles of up to 20 degrees to the sidewall. Dips are steep, ranging between 85^0 and 90^0. As with the bedding they occur all along the tunnel. Their position with respect to the tunnel is illustrated in one small zone in Figure 3.16.

The bedding, "bow wave" fractures and rockbolt support all played an important role in controlling the distribution of damage as a result of the shock waves (Le Bron and Haile, 1998b). This can be seen in Figure 3.17, which is a collage of photographs of a portion of the damaged wall. The wall was whitewashed before the blast so the dark areas on the collage show the areas where rock has been ejected. A rockbolt can be seen containing some of the whitewashed rock. Many damaged areas have boundaries defined by the bedding. The "bow wave" fractures often defined other boundaries and block thicknesses in some cases.

Petroscope studies in holes drilled perpendicular to the tunnel wall revealed that new tensile fractures had developed within 1m of the tunnel wall. These were clean, wavy, less than 1 mm wide and aligned parallel to the tunnel wall. In some cases these planes bounded the ejected blocks.

The dimensions of all ejected blocks with lengths greater than 300 mm were measured. The volume of each of the blocks was estimated and then accumulated for every metre along the tunnel wall. The result is shown in Figure 3.18. Relate this to the reference tape indicated in Figure 3.18 and it can be seen that most of the damage was sustained directly opposite the charges in the blast holes i.e. between 9 m and 19 m on the tape. The cut off at 9 m was sharp. There was damage beyond 19 m, however, i.e. up to 9 m ahead of the severely damaged area on the tunnel wall. The solid line in Figure 3.18 is a moving average curve of the damage as reflected by the volume of ejected blocks.

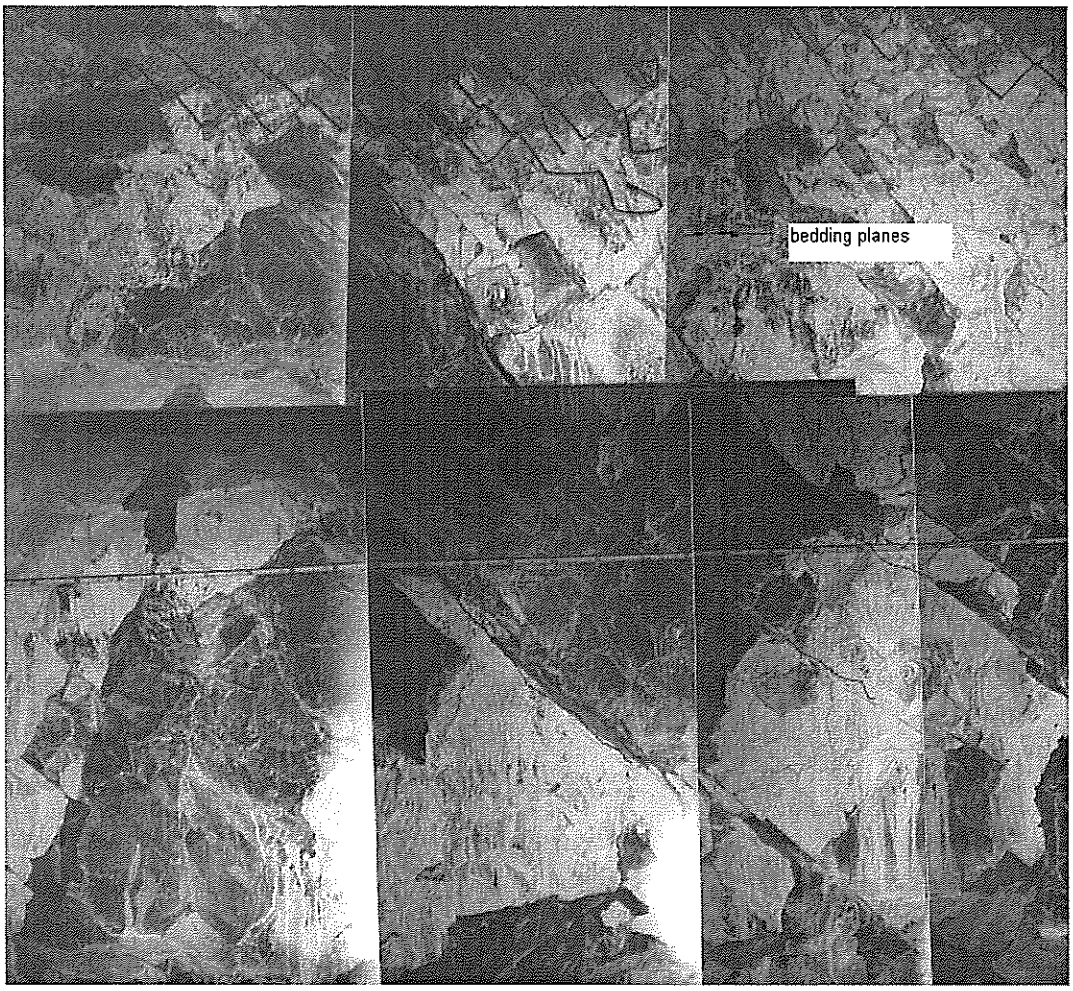

Figure 3.17 Photograph of a portion of the damaged sidewall. A rockbolt can be seen in the top centre.

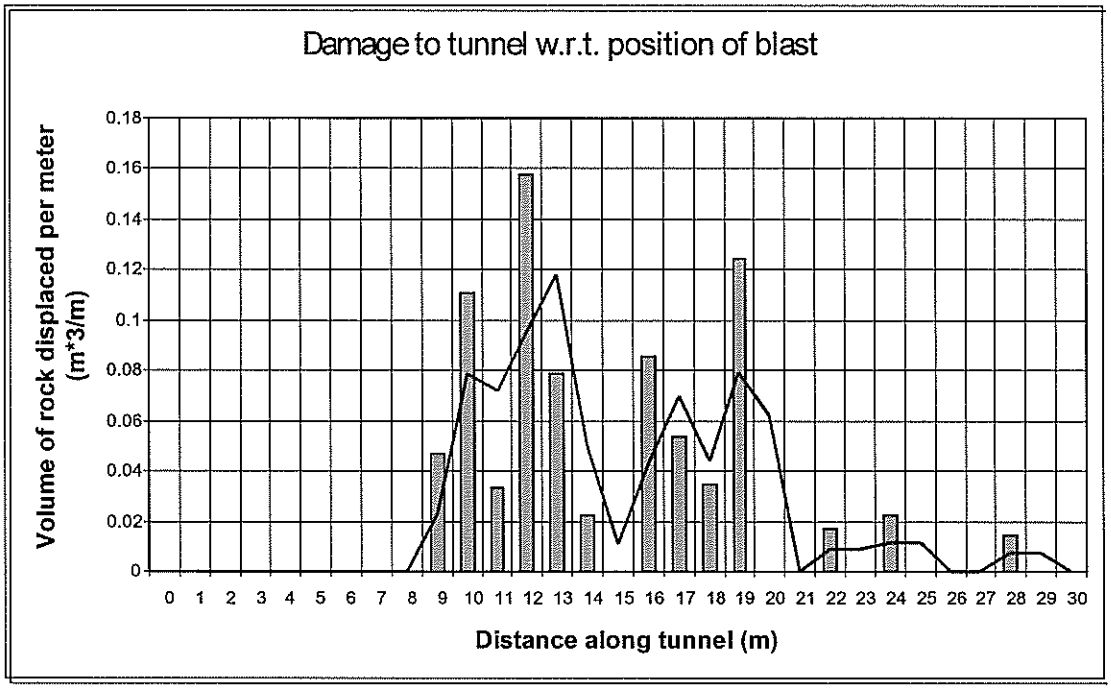

Figure 3.18 Volume of rock ejected along the tunnel wall.

A comparison of ground penetrating radar (GPR) scans taken before and after the blast showed the development of new fractures in the vicinity and ahead of the blast holes themselves. The scans also showed the possibility of the development and opening of fractures close and parallel to the tunnel wall. The latter formed as a result of the interaction of the seismic waves with the surface of the excavation as would be the case in a rockburst. Figure 3.19 is an example of an "after blast" scan that probes 9 m into the rock mass i.e. beyond the blast holes. The fracturing described above can clearly be seen. All the "before blast" scans showed were indistinct indications of the "bow wave" fractures described earlier. A total of 15 scans were done (Grodner, 1998).

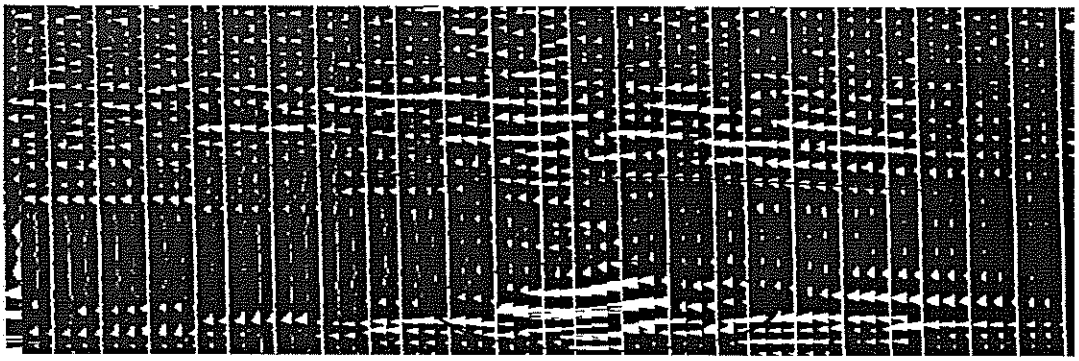

Figure 3.19 A ground penetrating radar scan taken after the simulated seismic event. The lower part of the plot is at the skin of the tunnel and the top part of the plot is at 9 m penetration

Holes containing extensometers, to measure dilation of the rock perpendicular to the tunnel wall, were set up at six sites (Grave, 1998). The position of four of these sites is shown in Figure 3.16. They were designed to measure dilation at the surface and at even intervals into the rock. The results are tabled below. Dilation at the surface ranged between 7 mm and 9 mm, diminishing as one moves away from the damaged area. Readings between say 3 m and 6 m in the rock only make sense when one considers that the instrument penetrates the area affected by the blast holes themselves as confirmed by the GPR scan. Dilation readings for six extensometer stations are given in Table 3.8

Table 3.8

Dilation readings in mm at six extensometer stations.

No. of Extenso -meter	Depth relative to the wall of the tunnel									
	6 m	5 m	4 m	3 m	2,5 m	2 m	1,5 m	1 m	0,5 m	0 m
Ex 1	6	10	3	5		2		3		5
Ex 2	5	0	4	3	5	5	7	4	4	7
Ex 3	2	1	9	0		0		0		4
Ex 4						4		0	3	3
Ex 5						1		0	3	0
Ex 6						0		0		0

3.6.2 Amplification of the seismic signal monitoring after the blast

Seismic data were collected before and after the blast. The sources were two blasting sequences located at two working faces at about 100 m from the test site (Figure 3.20). The geometry "source – receiver" allowed the seismic waves to propagate through the area-effected form the blast. Previous work by Durrheim et al. 1997, indicated that the amplification of the seismic signal on the skin of excavations is dependant on the degree of fragmentation in the vicinity of the receiver. These effects have been studied further using the data recorded before and after the blast.

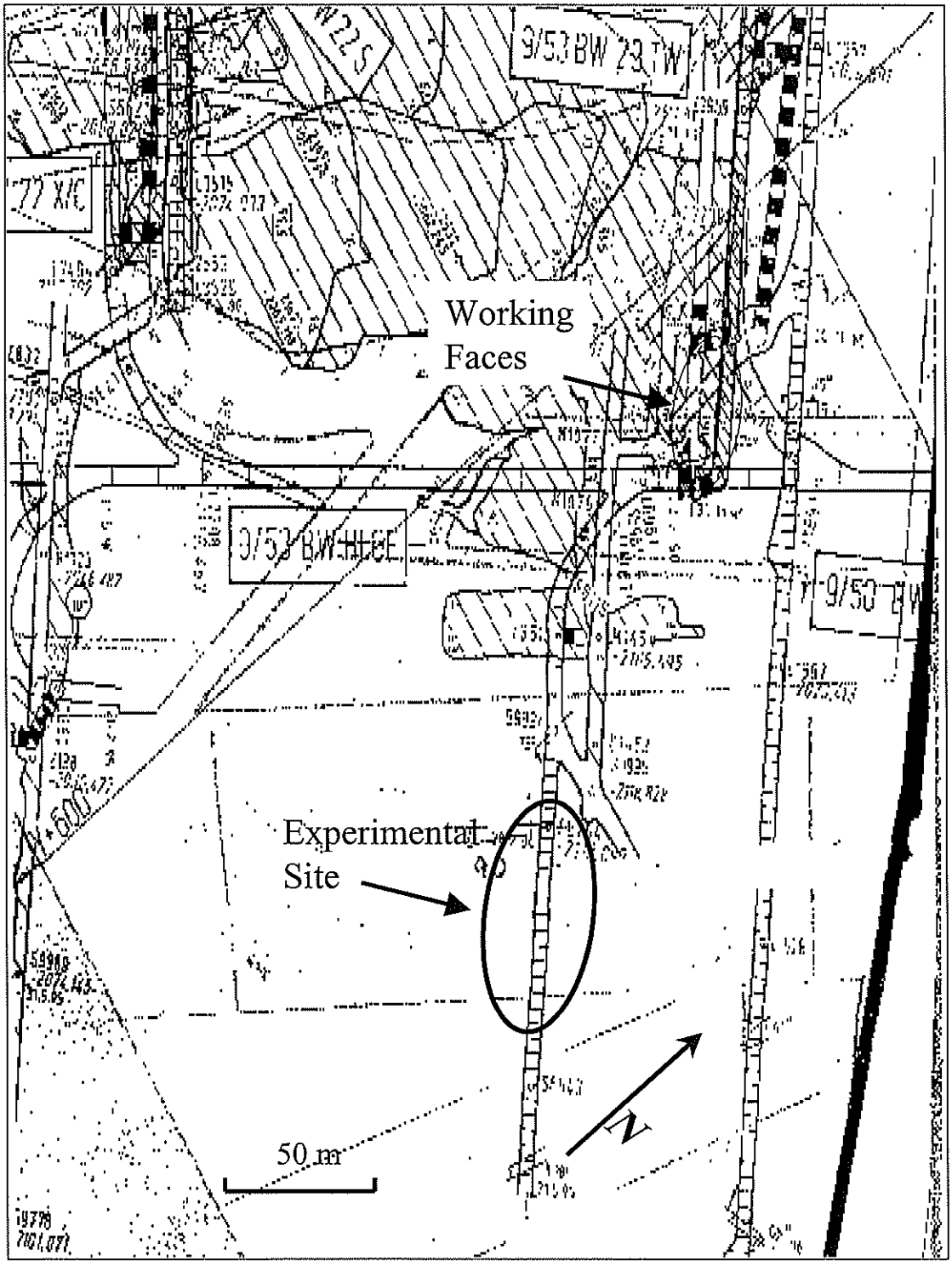

Figure 3.20 A plan of the test site.

Two types of comparison were done to evaluate the destruction effect of the shock wave on the blasting wall.

A comparison of the maximum velocities in the time domain recorded before and after the blast (Geophones C1 to C8 from site "C", Figure 3.1) indicated a five to six folds amplification of the velocities recorded after the blast. (Compare Figure 3.21 - before the blast to Figure 3.22 - after the blast). The only exception is the footwall channel, which was probably less affected by the blast wave or the ground between the rock and the geophone, acted as a damping filter on the incoming seismic waves.

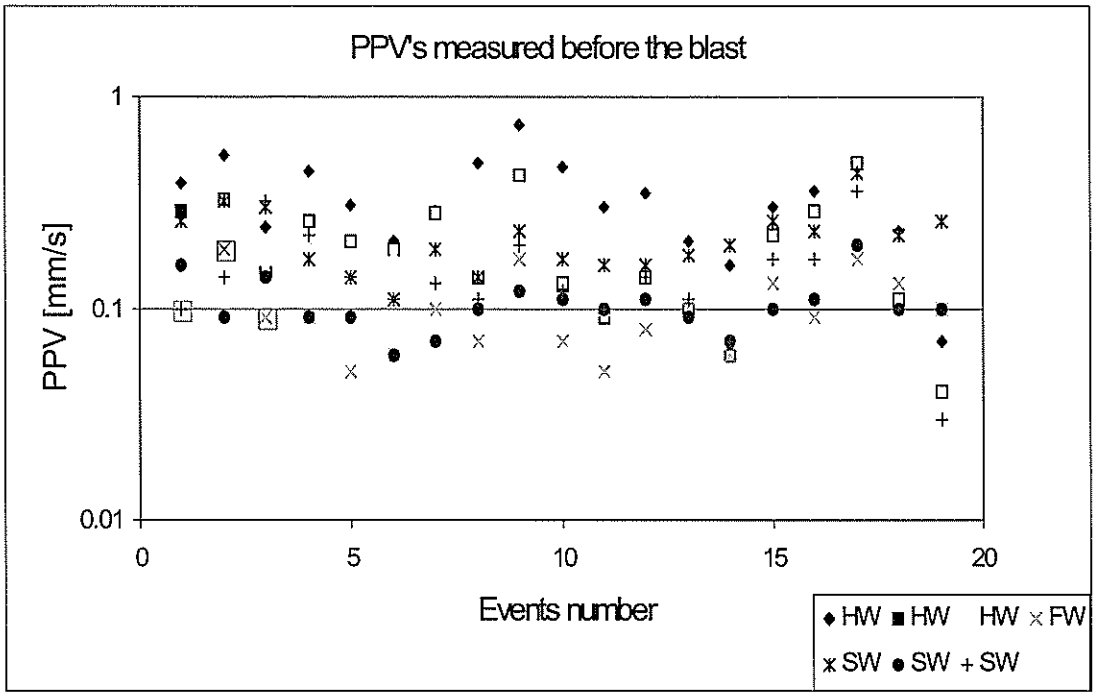

Figure 3.21 Peak particle velocities measured on the blasting wall, the hangingwall and the footwall before the main blast.

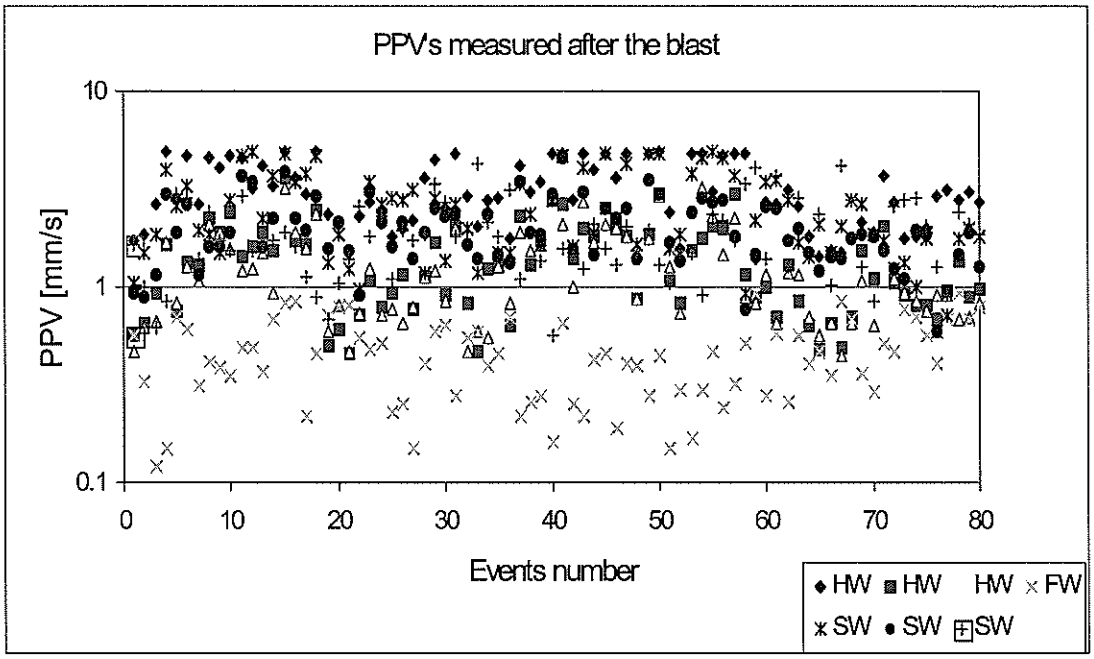

Figure 3.22 Peak particle velocities measured on the blasting wall, the hangingwall and the footwall after the main blast.

A second comparison was done using the spectral ratio between two geophones placed normal to the blasting wall at C5 and C8, using method described by Spottiswoode et al., 1997. The first geophone was closer to the blast and almost at the end of the area of low intensity damage, while the second geophone was 12 m from the first one and further away from the blast, in the area where the damage was not severe.

The maximum velocities recorded before the blast for both the close and the distant geophones were in the range of 0,1 mm/s to 1,0 mm/s and they did not differ significantly from each other Figure 3.23. After the blast the values of the maximum velocities recorded on the closest geophone were 2 to 3 times higher than the velocities recorded at the distant geophone (Figure 3.24). It can be also seen that the velocities recorded at the distant geophone remained almost unchanged.

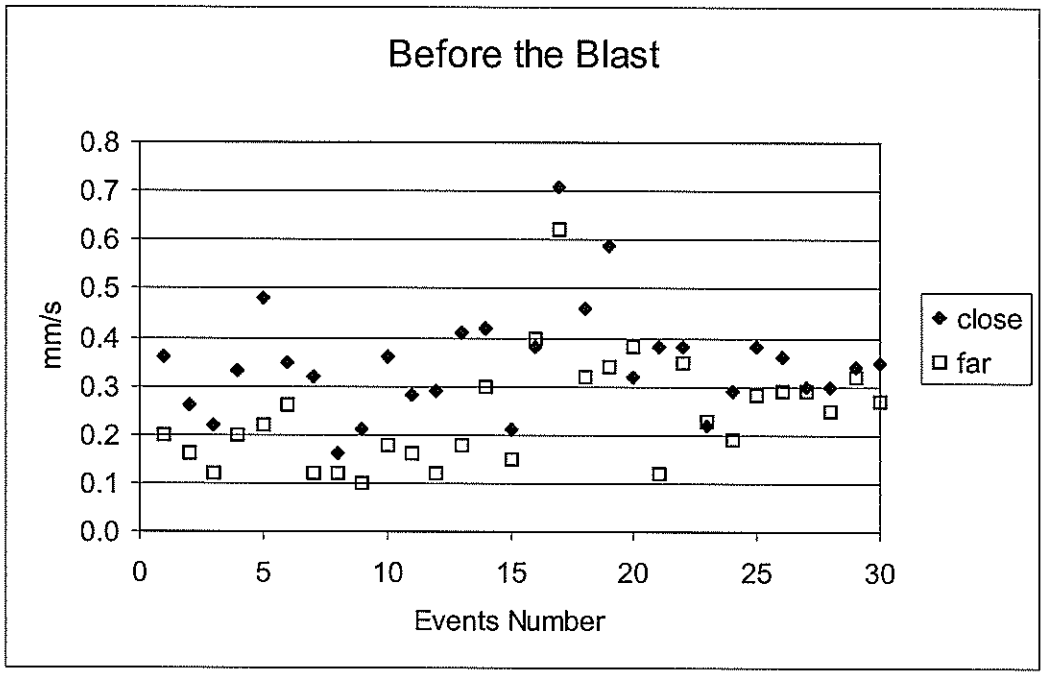

Figure 3.23 Peak particle velocities measured on the blasting wall before the main blast.

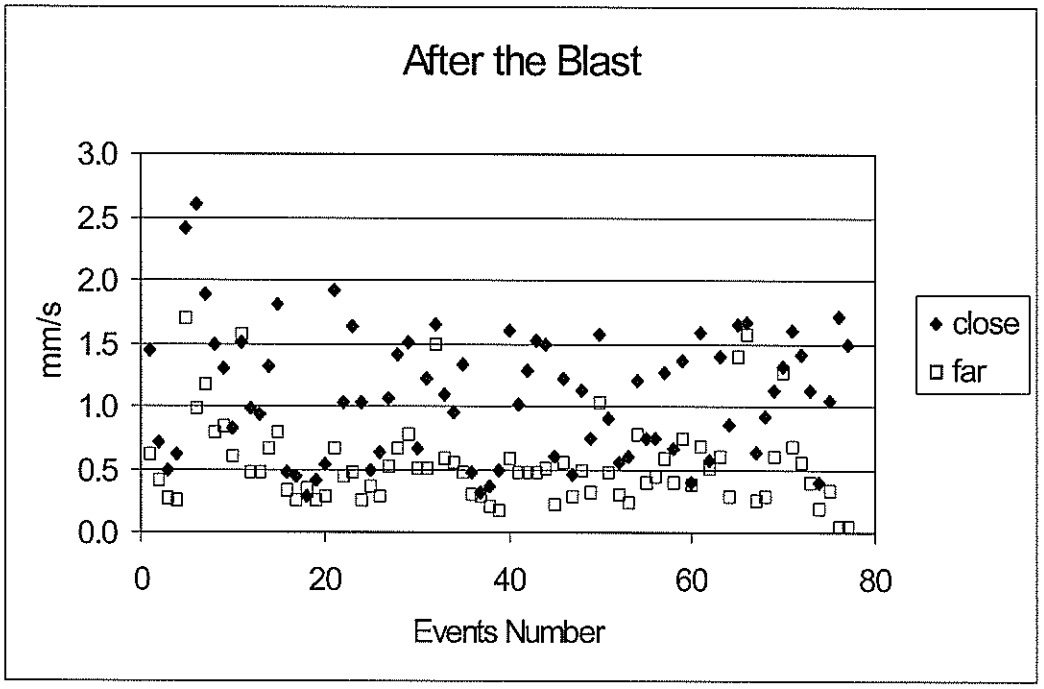

Figure 3.24 Peak particle velocities measured on the blasting wall after the main blast.

It is also interesting to note how these changes are distributed in the frequency domain. Figure 3.25 represents a Log_{10} amplitude spectral ratio for the seismic events recorded at the closer to the distant geophone, before the blast (It can be seen that the amplitude spectral ratio between the geophones is approximately 1,0 at all frequency). Figure 3.26 shows the same spectral ratio but calculated for the events after the blast. The amplification of the signal for the closer geophone is about 10 times on average over the frequency range of 0 Hz 400 Hz and in the low frequency domain even greater.

This result is of interest with respect of support design criteria for rockburst conditions. Frequency less than 100 Hz are expected for larger, potentially damaging events.

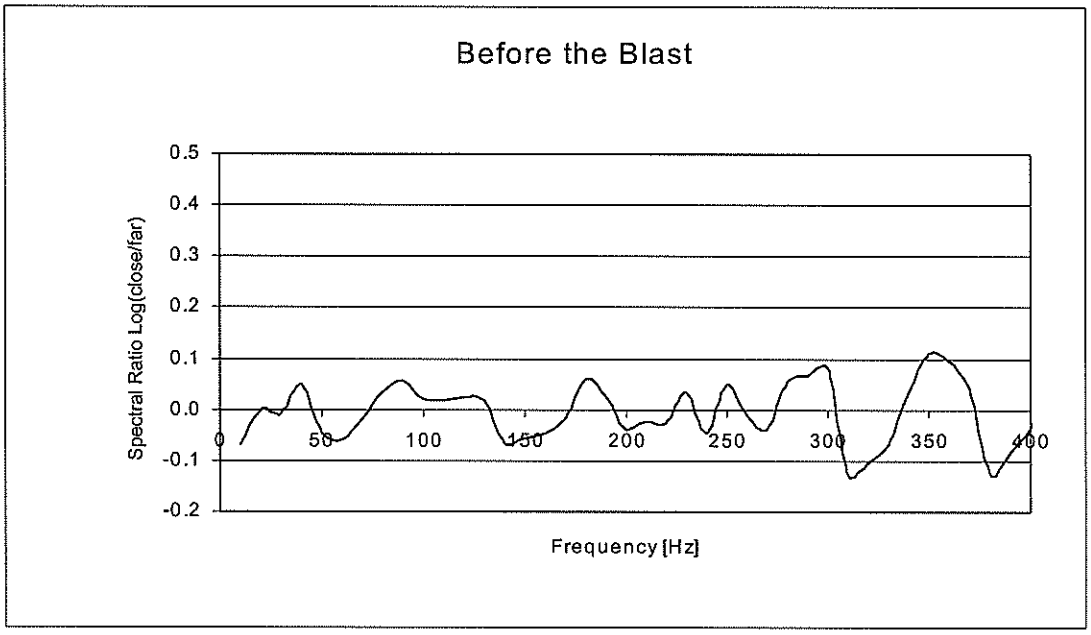

Figure 3.25 A Log_{10} amplitude spectral ratio, closer to distant geophone for seismic events recorded at the blasting wall, before the blast.

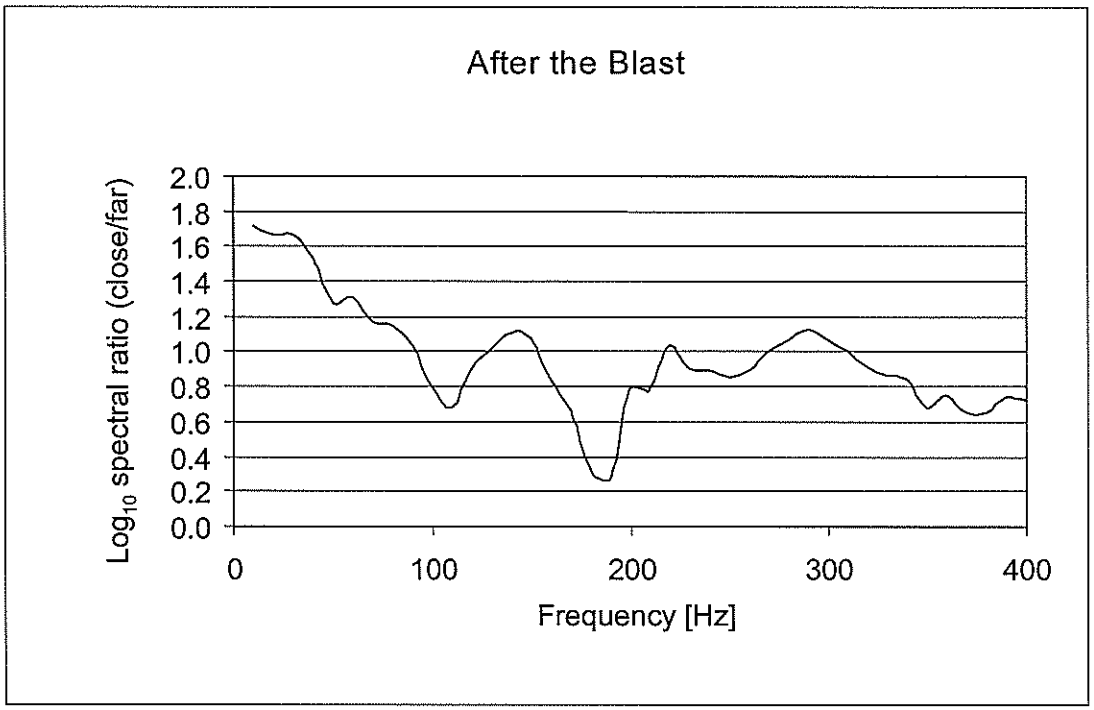

Figure 3.26 A Log_{10} amplitude spectral ratio for the seismic events recorded at the blasting wall, closer geophone to the distant one, after the main blast.

The results obtained so far indicate that there is significant amplification of the peak particle velocities when the seismic wave is propagating through the fractured rock. This analysis has profound implication and needs further study.

3.7 Conclusions

Some of the important findings are listed below:

- The distance of the blast holes from the tunnel wall ensured that no gas pressure was directly involved in damaging the wall of the tunnel. The damage resulted from the interaction of the blast wave with the tunnel, as would happen in a rockburst. Extensiometer probes and ground penetrating radar scans confirmed the development of new fractures close to and parallel to the damaged tunnel wall.

- Two areas of damage were identified on the blasting wall:
    - area with high intensity damage: ground velocity at 3,3 m/s was recorded by an accelerometer ejected with a block of rock
    - area with low intensity damage: ground velocity at 1,6 m/s was recorded by an accelerometer which remained in the tunnel wall
- High speed filming revealed rock fragments being ejected from the wall at velocities in the range of 0,7 m to 2,5 m per second. The measurements were taken in the area of low intensity damage.
- The maximum velocity recorded in the solid rock close to the blast was compared to the velocities recorded on the blasting wall. Ratios were established of 2,2 times, between the solid rock and the area with high intensity damage and ratio of 1,3 times between the solid rock and the area with low intensity damage, after correcting for $R^{-1/2}$, geometric attenuation in the near field.
- The attenuation of maximum velocities for the main blast as a function of distance R was found to follow the law of $1/R^{1,7}$.
- The simulated rockburst was recorded by the Vaal River Operations regional seismic network. The local magnitude was estimated as M_L = 1,3. Further use of the simulated rockburst for scaling of mine tremors located in this region is recommended.
- Peak particle velocities (PPV's) were measured on the tunnel wall both before and after the experimental blast. The PPV's were as a result of normal mining operations some 100 m from the site. The PPV's after the blast were amplified some five to six times, that recorded before the blast indicating the effect of damage caused to the rock surrounding the excavation.
- In the frequency domain well defined amplification in excess of ten fold was obtained in the low frequency band (0 – 100 Hz)
- The new fractures together with both natural bedding planes and "bow wave" fractures formed during the development of the tunnel determined the shape of blocks ejected from the wall at the time of the simulated rockburst.
- Tendon support of the tunnel had the effect of reducing the PPV's and damage to the wall in their immediate vicinity.
- It was found that the failure of the rock occurred predominantly on prominent discontinuities such as bedding planes and fractures. Damage to a tunnel is changed in the presence of discontinuities and this fact should be taken into account when support is designed.

4 Dynamic behaviour of the rock around underground excavations

4.1.1 Introduction

Measurements of the site response made during the past three years have shown that the phenomenon of the dynamic site response is real and significant. Many interesting results have been obtained. For example, it was found that the peak particle velocity on the skin of the excavation may be amplified four to ten fold compared to a point in solid rock a similar distance from the focus, and the total energy flux by even larger amounts. Ground motion at points less than a metre apart show differences in amplitude and phase which can only be accounted for by large strain across fractures. A case has been recorded where this behaviour changed dramatically following a nearby seismic event, suggesting that a significant change in of stress occurred. The data were initially analysed using classical seismological approaches such as spectral ratios. Time domain approaches, such as deconvolution and system identification using data adaptive filters, were also investigated. Latterly, analysis techniques used by earthquake engineers such as single and multi-mode harmonic oscillators have been applied.

Much scope exists for the application of concepts from earthquake engineering to the study of rockburst damage mechanisms and rockburst resistant design. Initially the project focused only on the motions of the rock. Insights gained from the earthquake engineering literature suggested that the entire rock support system should be analysed. This formed an important component of the project.

4.1.2 Site description.

Two sites on Carbon Leader stoping at Western Deep Levels, East Mine – panel 93 E4 were chosen for underground monitored in collaboration with project GAP 330. Figure 4.1 illustrates the position of the sites and the mining environment.

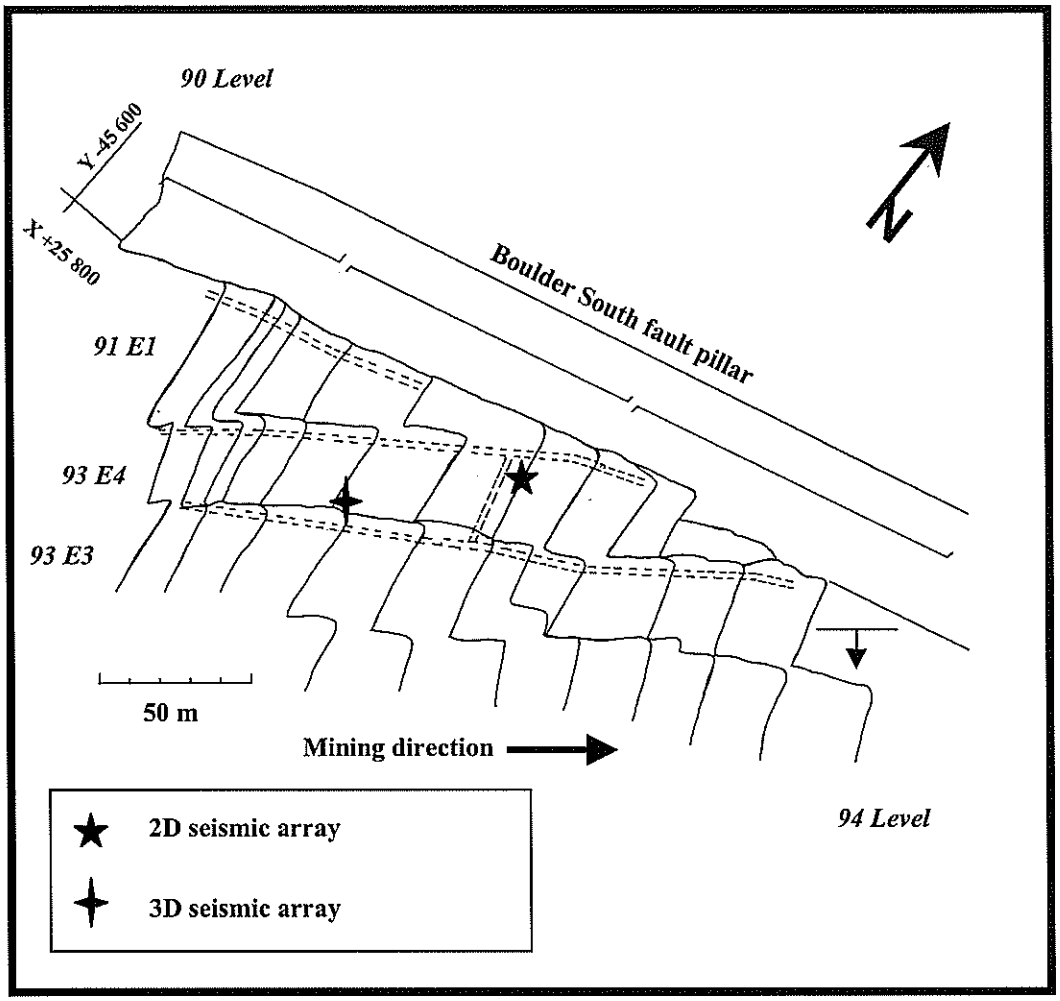

Figure 4.1 Mining plan and position of the test sites.

The discontinuities include joints, faults, bedding and parting planes together with mining induced fractures.

Three major joint sets, throwing a north-north-east, a east-west trending and a north-west were measured. They extend for up to 1 m and are 1 to 3 cm thick. Faults striking north-east, sub-parallel to the dominant joint set. The faults are all normal with throws of less than 1 m and dip steeply to the south.

A well-defined argillaceous bed locally defines the base of the Rice Pebble Marker (found below the Green Bar). The base also occurs as a welded plane with a thin argillite veneer. This variation may be owing to sedimentological control as well as selective bedding parallel movement along the plane.

Mining-induced fractures have been grouped into extension and shear fractures. Extension fractures occur as discrete, persistent fractures. Dips are steep (70^0-85^0), but generally less than those of the shear fractures. Orientation is generally face parallel. Spacing between extension fractures increases near shear fractures and faults typically 2-10 cm but. Between shear fractures the spacing is 15-25 cm. Shear fractures occur as zones of intensely fractured rock up to 15 cm wide along which some displacement has occurred. Spacing of the shear fractures varies between 1,6 m and 2,0 m.

A representative stratigraphic column is presented in Figure 4.2. The footwall consists of a green-grey, poorly sorted, very coarse grained, immature quartzite. Glassy, cleaner quartzites occur locally. Persistent, argillaceous parting planes are up to 20 mm thick and strongly laminated. Impersistent, argillaceous parting planes are 20-30 cm apart and up to 4 mm thick and also strongly laminated. The thicker argillaceous parting planes have smooth, shiny bottom contacts indicating movement along the planes. A 5-10 cm thick medium pebble conglomerate occurs approximately 50 cm below the Carbon Leader and another similar conglomerate up to 170 cm below the Carbon Leader.

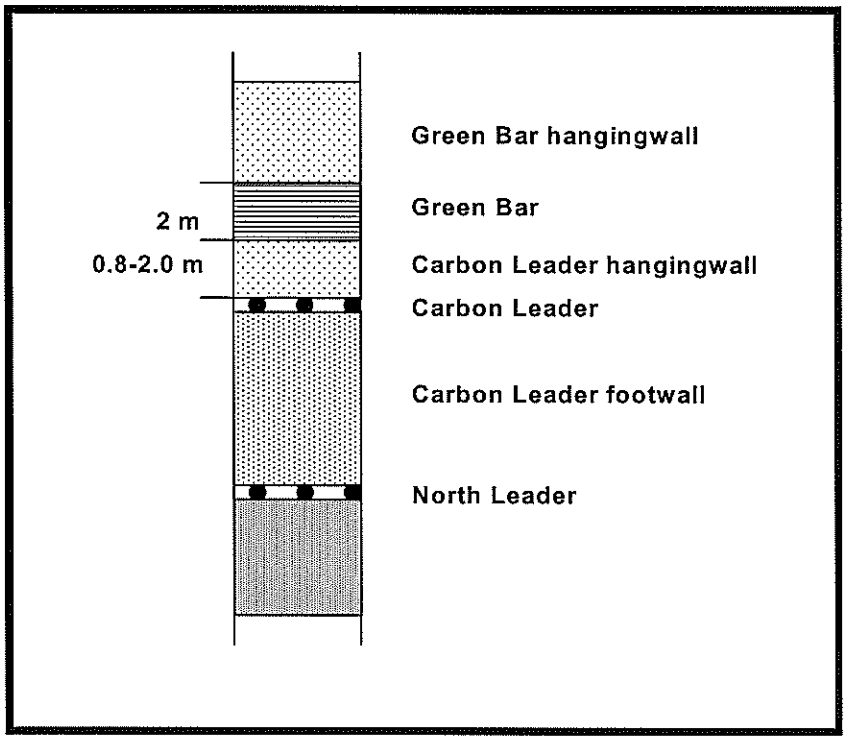

Figure 4.2 Stratigraphic column of the Carbon Leader.

The Carbon Leader is a narrow conglomerate up to 12 cm in thickness. It has an erosive base, often eliminating the argillite parting directly below it.

The Green Bar, an argillaceous unit up to 2,5 m thick, overlies the Rice Pebble Marker. The Green Bar lies at an average of 2,0 m above the Carbon Leader. Local tectonic rolls and erosional features may reduce the quartzite parting to 1,2 m. The base of the Green Bar is characterised by a smooth, polished, tectonised undulating surface. A well-bedded, often pyritic siltstone occurs at the base, grading into a less well-bedded chloritoid shale. Fault gouge and vein quartz may occur locally on the bottom contact.

The Carbon Leader reef is being mined on strike by a conventional 25 m long panel. Until recently the stope used backfill as permanent support and Camlok props as temporary face area support. Permanent support has been replaced with elongates (initially cone props with a later switch to Madodas and then Eben Haeser) and packs without backfill.

The stope is being mined on strike, and the majority of hangingwall fractures are oriented between face-parallel and 20^0 oblique to the stope face, with a moderate to steep dip.

4.1.3 Method of observation

Following previous results we focussed on the analysing the difference in ground motion at closely spaced points.

The dynamic response was represented as an amplitude spectral ratio $R'(f)$ and phase difference $\delta(f)$ between two seismic signals measured at different points in the panel (Spottiswoode et al., 1997).

To compare the ground motion at different sites (e.g. *A* and *B*), the full waveforms were Fourier transformed:

$$V_A(t) \Leftrightarrow \tilde{V}_A(f) \quad \text{and} \quad V_B(t) \Leftrightarrow \tilde{V}_B(f) \tag{4.1}$$

where: $V_A(t)$ and $V_B(t)$ are the ground motion time histories and $\tilde{V}_A(f)$ and $\tilde{V}_B(f)$ are their Fourier transformations.

The ratio of the complex spectrum at each frequency was expressed as amplitude ratio *A(f)* and phase difference *δ(f)*:

$$\tilde{V}_B(f) / \tilde{V}_A(f) = A(f) \exp(2\pi i \delta(f)) \tag{4.2}$$

where: *A(f)* is an amplitude ratio and *δ(f)* is the phase difference:

Spectral values may vary widely and give a noisy appearance. Spectral ratios, such as A(f) in Equation (4.2), are more prone to noise. To obtain stable values, spectra for many events were obtained and the median used, R′(f) and δ′(f), of all spectral components for *A(f)* and *δ(f)* at each frequency. After replacing amplitude ratio's and the phase differences with their median values, averaged for number of events, the Equation (4.2) can be written as:

$$\tilde{V}_B(f) / \tilde{V}_A(f) = R'(f) \exp(2\pi i \delta'(f)) \tag{4.3}$$

The phase difference, *δ(f)*, was interpreted in terms of the propagation velocity of seismic energy. This provides some insights into the "softening" effect of the fracture zone around the stope. These analyses have suggested that the effective velocities of propagation are much less than the S-wave velocity.

The wave velocities and directions of propagation through a 3-D array of geophones can be estimated from time delays between pairs of geophones. The propagation velocity between any pair of geophones is derived by:

$$V = \delta D / \delta T \tag{4.4}$$

where: δD *is* the distance between two geophones and δT is the travel time.

Given the complex nature of in-stope seismograms and difficulty in peaking P- and S-arrival times accurately, we estimated the travel time from cross-correlation analysis of two waveforms. Than the apparent velocity is given by:

$$V_a = V / \sin(\theta) \tag{4.5}$$

Where: θ is the incident angle between the incoming ray-path and the line between the geophones

If the apparent velocity is obtained along two mutually perpendicular directions using two pairs of geophones, the direction and apparent velocity within the plane described by the lines of the geophone pairs can then be obtained. This is illustrated in Figure 4.3 (a), where the apparent velocities are drawn as vectors V_x and V_Y. The "propagating wavefront" is simply parallel to the line between the velocity vectors of each pair. When two pairs are built from three geophones, the common geophone forms the origin, as drawn in Figure 4.3 (b). Two pairs can also be made up of from four geophones. In this case, the two vectors are tied to a common point.

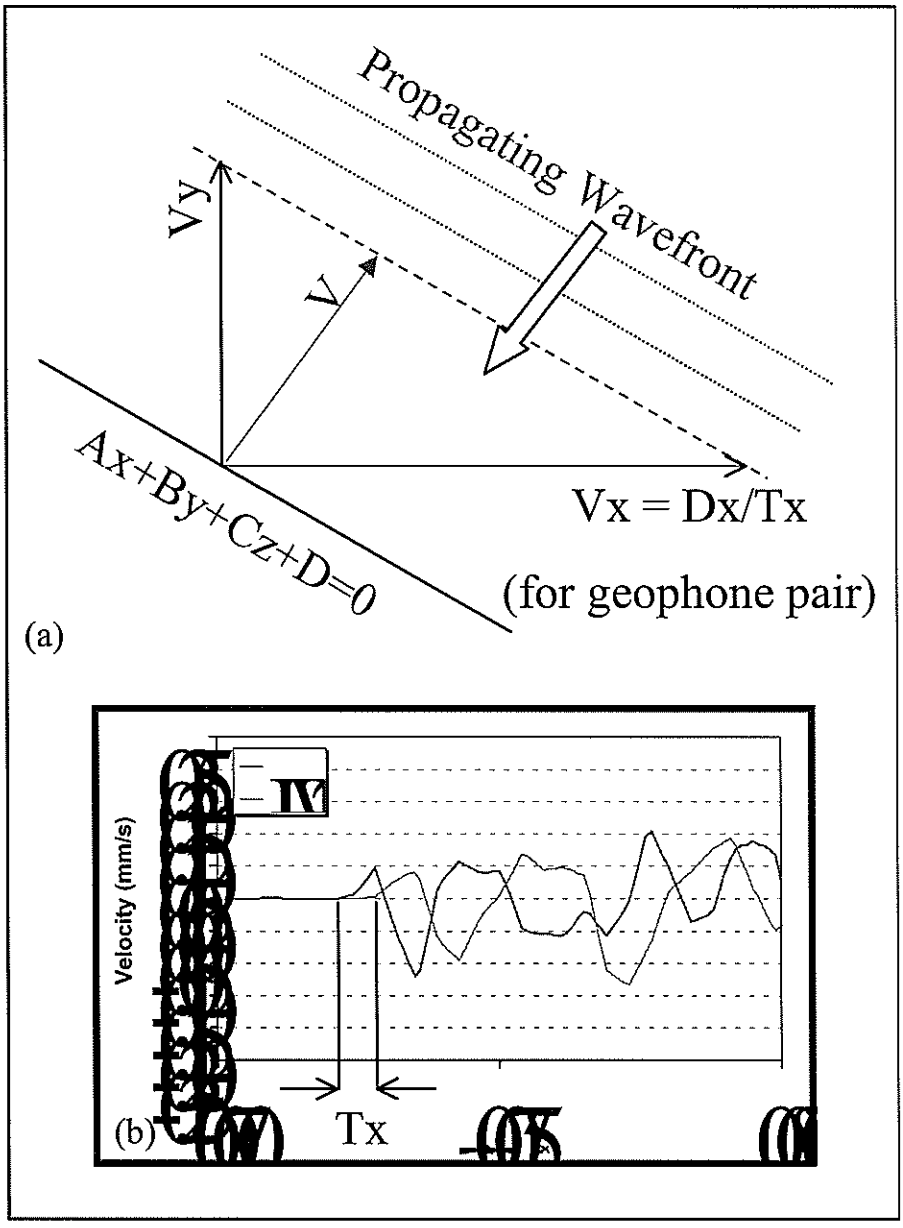

Figure 4.3 (a) Determination of velocity for a plane wave passing a pair of spatially separated geophones; (b) Example of difference in recorded arrivaltimes at a pair of spatially separated geophones.

This procedure can be extended directly into three dimensions. Geophone pairing need not be mutually perpendicular, but must be sufficiently 3 D to provide reasonable resolution.

4.1.4 Analysis of peak particle velocities

4.1.4.1 Up-hole micro seismic array (3 D observations)

A linear array of triaxial geophones connected to a Portable Seismic System (PSS) was installed into a 10 m long hole drilled vertically into the hangingwall. Each of the five triaxial sites was separated from its nearest neighbour by 2 m, with the lowest geophone being positioned into the hangingwall. In addition, a surface array of uniaxial geophones connected to a ground motion monitor (GMM) was installed on the skin of the hangingwall in the immediate vicinity of the hole. The PSS and GMM shared a common channel, to confirm consistency of system calibration and facilitate to combination of the data sets from these two systems (Figure 4.4).

The lowest triaxial geophone was installed just below the bottom the Green Bar interface, while the next geophone was installed above the Green Bar interface. The other three triaxial geophones and the surface vertical geophones are all located in quartzite hangingwall strata above the Green Bar.

A preliminary estimate of wave velocities in the vicinity of up-hole array (Figure 4.4), is presented in GAP 330 report. The velocity values in the range of 500 m/s to 700 m/s were obtained. These were confirmed by direct measurements from a hammer blow source where the numbers are quite variable from event to event and are also so much lower than the P- and S- velocities for solid rock taken as 5800 m/s for P- and 3700 m/s for S- wave. As values much less than those for solid rock have profound implication for our understanding of the rock mass dynamic behaviour. These results were further re-evaluated for a paper in preparation (Milev et al., 1998)

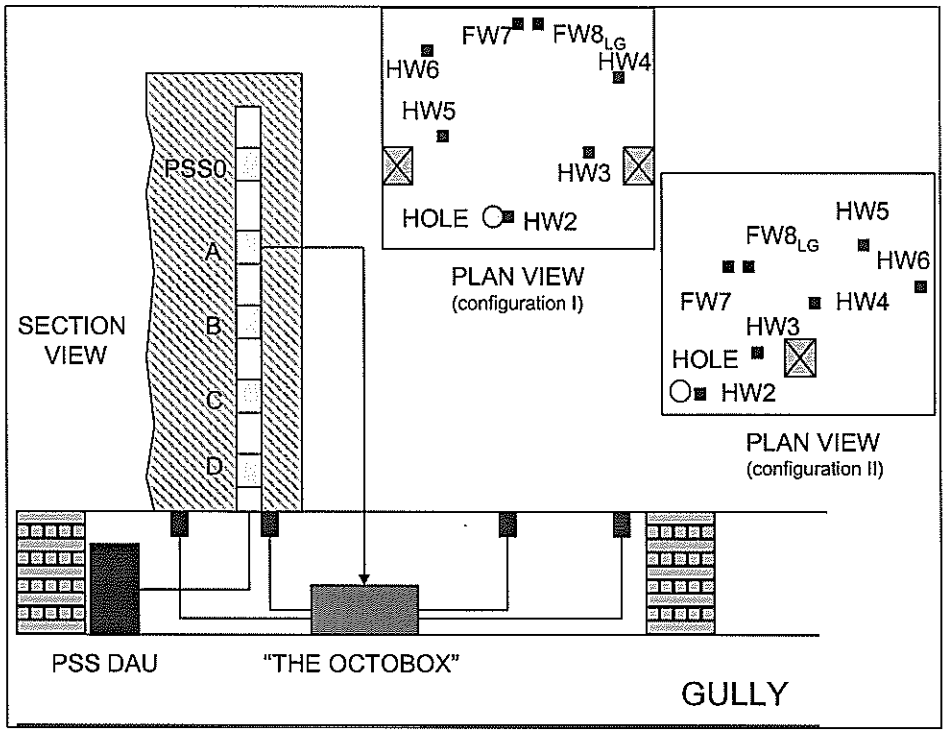

Figure 4.4 Plan and sectional view of 3 D micro seismic network installed at WDL, East Mine, 93E4 panel: configuration I, operated from January '98 to May '98; configuration II has operated since May '98.

Some 521 common events were identified as having been recorded by both the PSS and the GMM, and the data files were combined for joint assessment. All detailed analysis was conducted using the combined data.

Some repeatable characteristics which had been observed in the PSS waveforms – notably, the apparent azimuth angles between source and receiver derived from the known polarisation characteristics of the P-wave first arrivals – were used to group the data into various clusters. The mine's data were then used to associate the clusters with specific source regions (e.g. the 93 Level stope faces to the north east of the recording site, which were steadily advancing away from the site during the period of recording).

It was found that data recorded from seismic events on *90 Level* (to the *west* of the site) tended to have dominant P-wave amplitude on the east-west horizontal component. Travel times for these seismic waves tended to be shorter than expected from the assumed rock mass velocities. The waves recorded on the geophones closer to the hangingwall surface arrived with a noticeable delay compared with those further into the hangingwall.

Data recorded from seismic events on *93 Level* (to the north east of the site – associated with stope faces closest to the site) tended to have similar P-wave amplitudes on both the north-south and east-west horizontal components. Travel times tended to be more or less consistent with the expectations. There was generally negligible delay in arrival of the waves at the geophones at various depths into the hangingwall.

Data recorded from seismic events on *94 Level* (to the *east* of the site, at similar distances as those for the 90 Level events) tended to have a dominant P-wave amplitude on the north-south horizontal component. Travel times for these waves tended to be noticeably longer than expected. There was typically no measurable delay in arrival of the waves at the geophones at various depths into the hangingwall.

A visual of the waveforms shows changes in the appearance of the waveforms from top to bottom through the borehole array.

An increased degree of complication of the signals from top to bottom was accompanied by an increase in the amplitude and duration of the coda waves (most probably Rayleigh waves). These effects are indicative of energy trapping within the fracture zone close to the excavation.

The maximum velocities for the entire data set recorded by the borehole array are shown in Figure 4.5. Their values ranged from 0,6 mm/s to 5 mm/s. Similar behaviour with small dispersion was obtained.

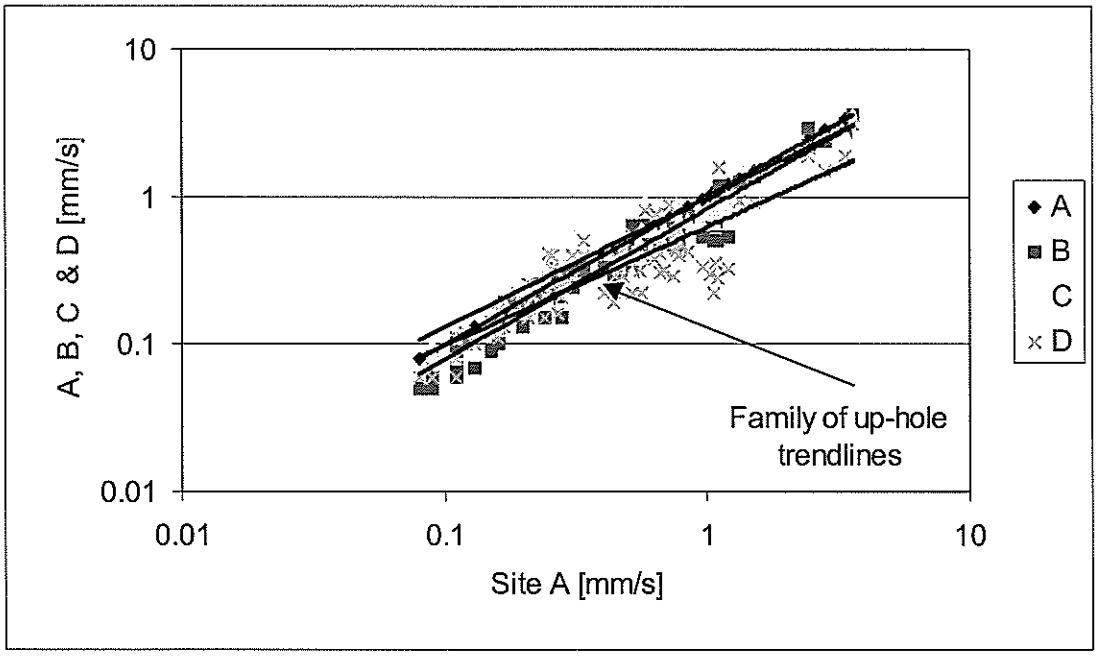

Figure 4.5 Maximum velocities recorded at site WDL, East mine, 93E4 panel, geophones A, B, C and D are installed in the borehole from top to bottom.

The maximum velocities recorded from the skin of the hangingwall are shown in Figure 4.6. The variations in velocity from individual events on the skin of the hangingwall were larger than the variations of velocity within the borehole. Their values (ranging from 0,2 mm/s to 7 mm/s) are larger than the maximum velocities recorded in the borehole array.

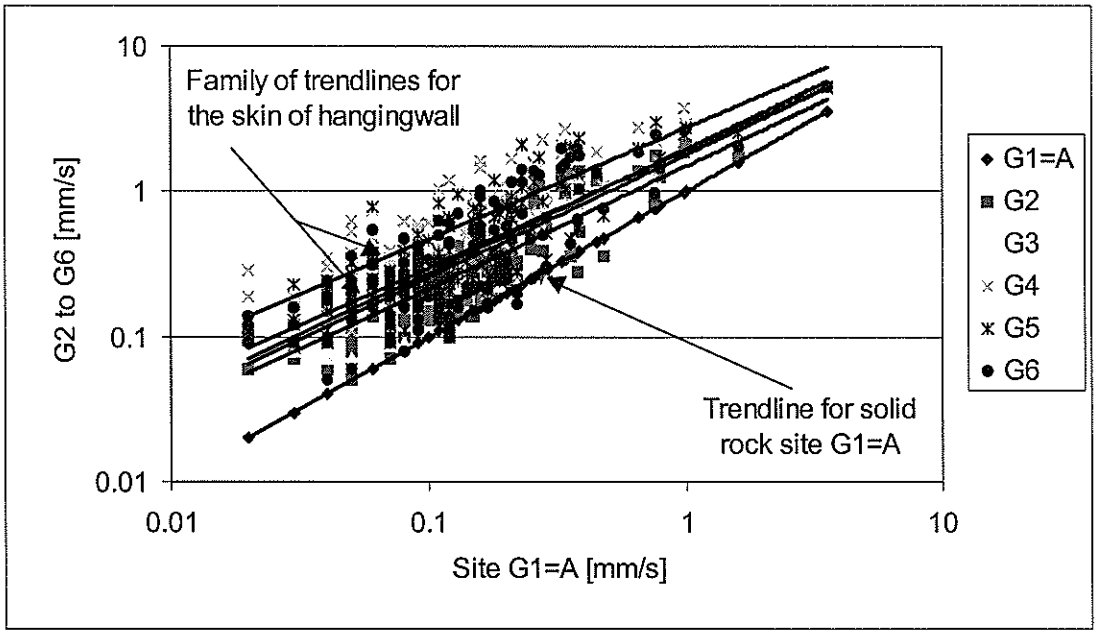

Figure 4.6 Maximum velocities recorded at site WDL, East mine, 93E4 panel (3D observations): G2 to G6 are placed on the hangingwall, G1 is about 5 into a hangingwall, and G7 is on the footwall.

The results from the velocity analysis indicated that the velocities recorded on the skin are several times larger than the values recorded in the more solid rock. These higher velocities are most probably the result of amplification by energy trapped in the fractured rock near the skin of the stope. However, the mechanism of energy trapping and interaction with incoming seismic waves is not well known.

The wave velocities and directions of propagation through a 3-D array of geophones were estimated from time delays between pairs of geophones. Waves passing any pair of geophones were cross-correlated. The time leg derived from the cross-correlation was used to estimate the velocity of propagation between each pair. Minimum of three mutual perpendicular pears was to estimate the velocity in 3 D space.

The results from velocity analysis have indicated that the time delays observed between pairs of geophone sites exceeded the travel time for P- and S-waves in solid rock, indicating lower wave velocities. These lower velocities are expected, given the high degree of fracturing near the skin of the stope. The velocities were quantified by estimation of the direction of propagation (at any moment) for a locally propagating plane wave. We expect that this will give insight into the mechanisms of energy

trapping that result in the pronounced coda waves. It will also assist in estimating the effective stiffness of the fractured rock and, thereby, it's dynamic response.

4.1.4.2 In-stope measurements of the peak particle velocities (2 D seismic array)

Two additional Ground Motion Monitors with a common trigger and 15 geophones were installed as part of the in-stope monitoring program described above. The site location is shown in Figure 4.1. The recording configuration is represented in Figure 4.7. Most of the geophones were placed on the hangingwall except B5, B6 and B7, which were deployed on the footwall.

Quasi-static instrumentation consisting of a closure ride station, extensometer, tiltmeter crack gauge and doorstopper was installed in the area covered by the ground motion monitors. We had hoped to use these data to divide the time plot into stages, for example, high and low stress, or different deformation rates. Unfortunately no clear pattern showing different stages were available from the quasi-static instrumentation. Details on the quasi-static measurements can be find in GAP 330.

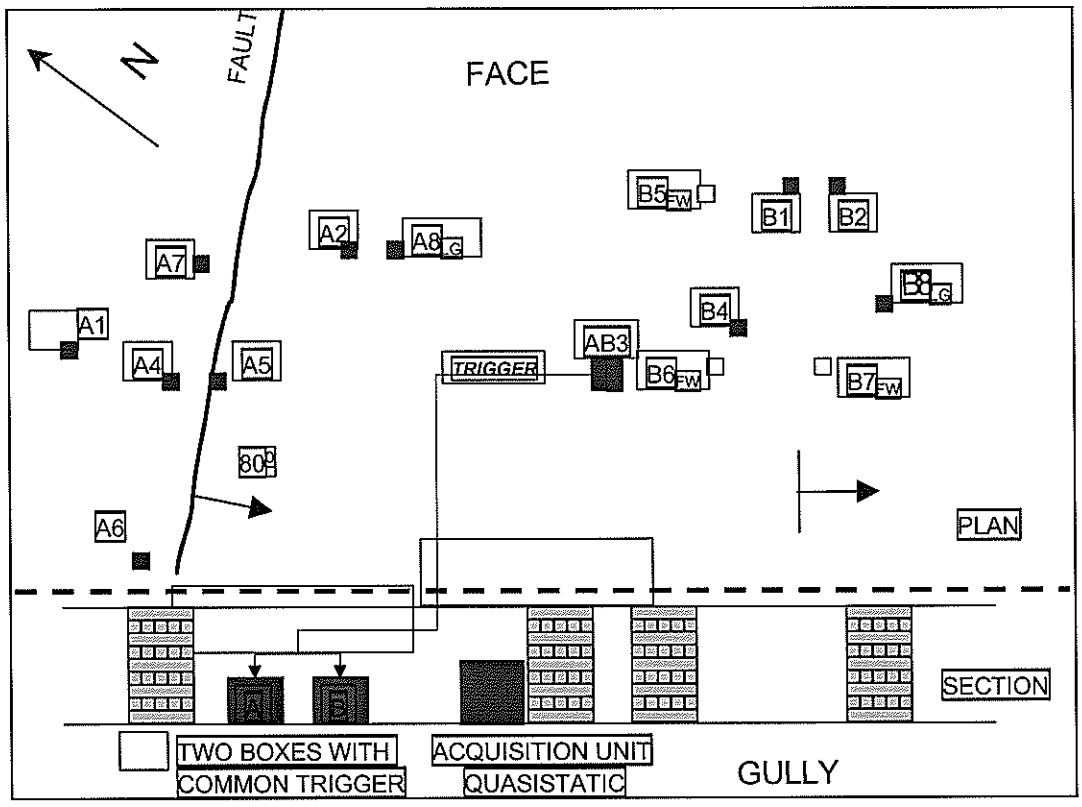

Figure 4.7 Configuration of micro seismic array consisting of two ground motion monitors (A & B) with a common trigger and 15 geophones. All geophones are on the hangingwall except B5, B6 and B7 which are located on the footwall.

The maximum velocities recorded at site A are shown in Figure 4.8. An interesting feature for this site was the northeasterly trending fault that cut through the mini network. The geophones A1, A4, A6 and A7 were on the North side of the fault while the geophones A2, A5, A3 and A8 were on the South side of the fault. Geophones A8 and B8 were reserved for strong seismic events and set on low gain only. Geophone A7 had poor signal characteristics. Geophones A7 and A8 have been excluded from the analysis.

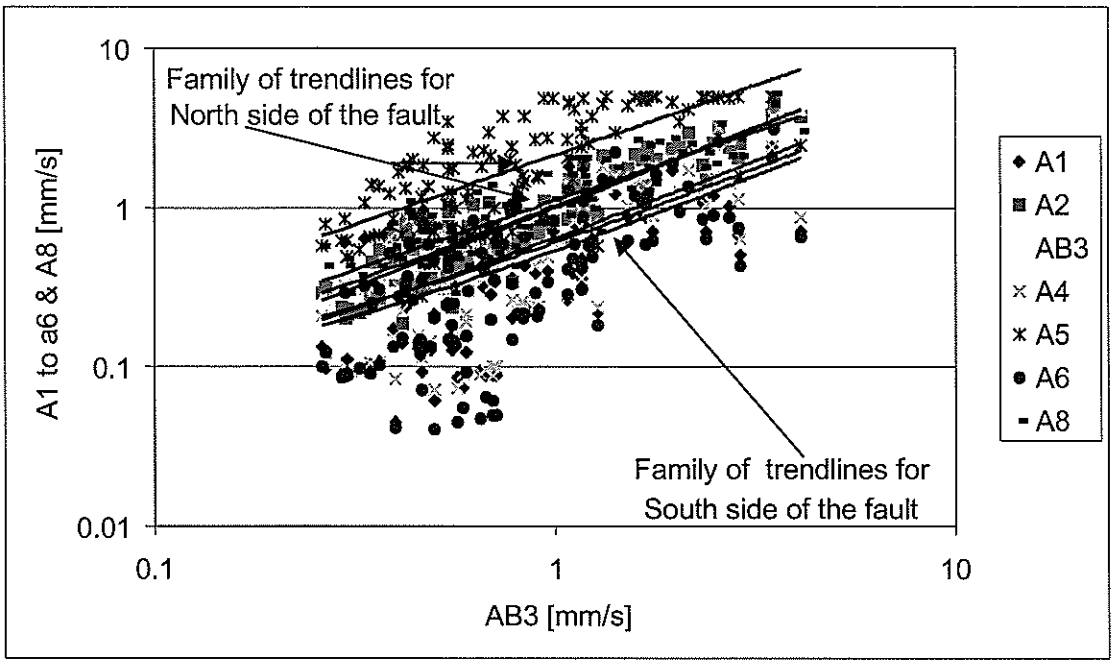

Figure 4.8 Maximum velocities recorded by box "A" (Figure 4.7). All geophones A1 to A8 are on the hangingwall. The geophone A8 is low gain.

It was found that the peak velocities measured at geophones located on the North side of the fault were higher than those at geophones located on the South site of the fault. The difference was clear for geophones A5 and A4 situated very close to the fault and only 20 cm from each other. The Log_{10} spectral ratio for these geophones presented in Figure 4.9 indicates that the maximum velocities recorded at A5 were four to five times higher on average than the maximum velocities recorded at A4, and about 10 times higher in the frequency range 100 Hz to 160 Hz.

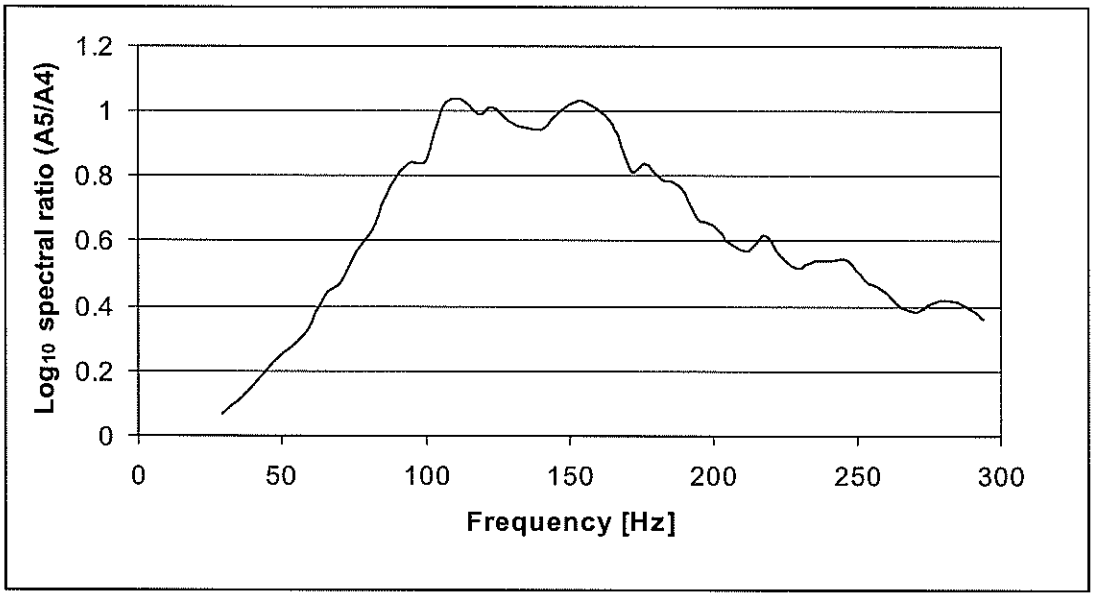

Figure 4.9 Log_{10} spectral ratio (A5/A4) of the seismic signal recorded on both sides of a fault by geophones 20 cm from each other shown in Figure 4.7.

Ground motion on the side of a small fault close to an abutment was found to be much less than on the other side of the fault. One possible explanation is that the fault inhibited the bedding-plane slip that normally allows for stress relaxation on the face. Higher skin stresses then formed on this side of the fault and these stiffened the fracture zone and inhibited the mechanisms, which lead to higher ground velocities.

Another possible explanation follows from observations of rock-bursts, namely that it is uncommon for intense damage to occur simultaneously both on a face and on an adjacent abutment. The highly stressed rock ahead of the abutment in this case allows the seismic energy to escape from the fracture zone. The fault was open in places and would act as a barrier to the transmission of seismic waves. Again, this can inhibit the mechanisms for high levels of ground motion on the north side of the fault

Figure 4.10 shows the maximum velocities recorded at site B. Geophones B1 to B4 were installed on the hangingwall while geophones B6, B7 and B8 were installed on the footwall.

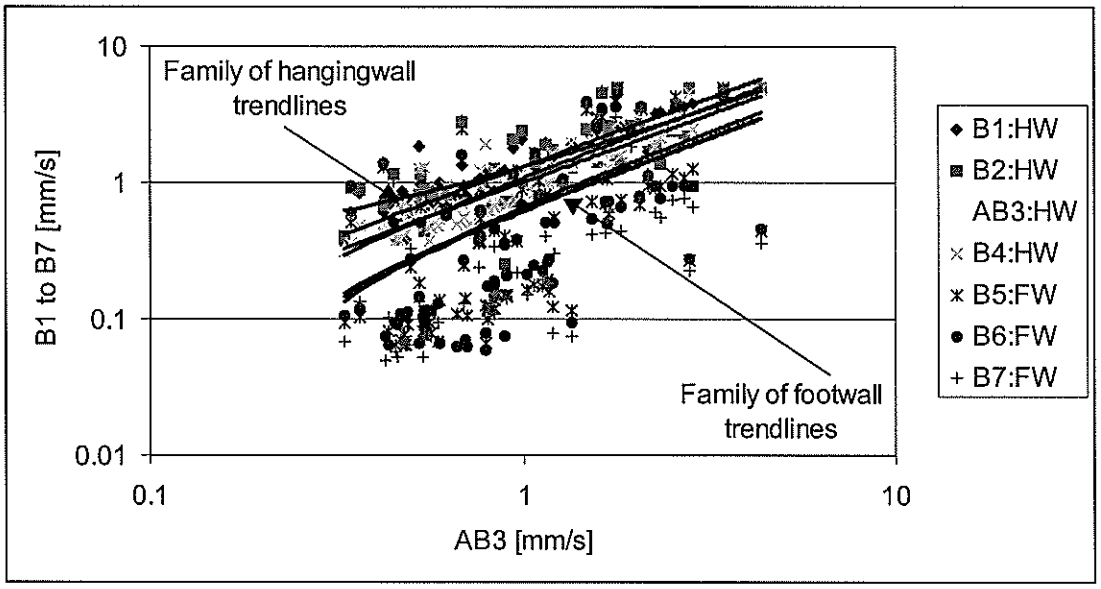

Figure 4.10 Maximum velocities recorded by box "B" (Figure 4.7). Geophones B1 to B4 and B8 are placed on the hangingwall. Geophones B5 to B7 are on the footwall. Geophone B8 is low gain

Peak velocities were used to look at the relative motion between hangingwall and footwall. This shows independent behaviour between the two, as has been observed before.

4.1.5 Dynamic response of the hangingwall observed by 3 D micro seismic array.

The dynamic behaviour of the rock mass surrounding the Up-hole site has been analysed in terms of spectral ratio. The three-dimensional seismic network installed there provides an excellent opportunity to examine the change in the seismic wave close to an underground opening.

Figure 4.11 shows the Log_{10} amplitude spectral ratio of the seismic signal recorded at 6,5 m into solid rock (G1) and a number of seismic signals recorded at the skin of the excavation (G2, G3, G4, G5 and G6) for Configuration I from Figure 4.4. We suggest that G1 (6,5 m into the borehole) closely represent the solid rock.

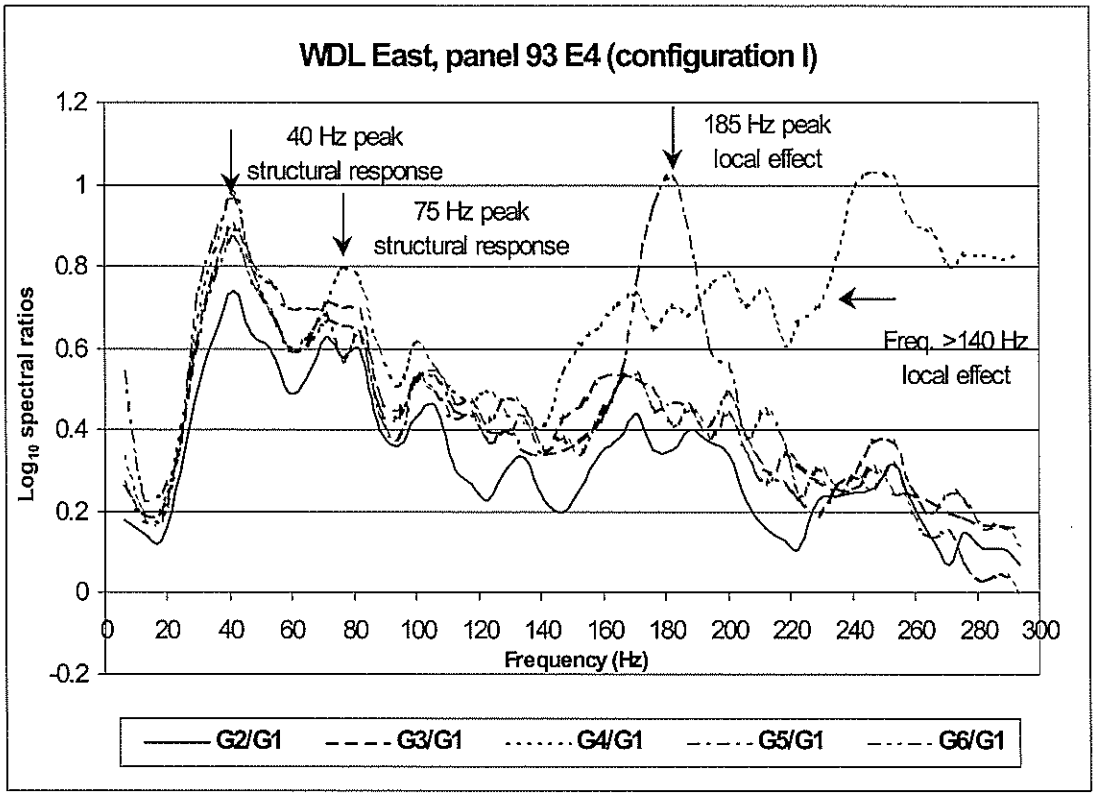

Figure 4.11 Log_{10}(spectral ratio) of the seismic signal recorded at 6,5 m into the hangingwall (G1) and a number of seismic signals recorded at the skin of the excavation (G2, G3, G4, G5 and G6) for configuration I from Figure 4.4.

Two mechanisms of dynamic response have been defined here: structural response, defined as a common spectral behaviour at all surface seismograms; and local site effect, defined by spectral peaks at one or two surface seismograms.

Strong structural response was observed in the low frequency range at 40 Hz and 70 Hz for all surface sites (G2 to G6). Local site effects were observed at two surface sites for frequencies above 140 Hz (G4 and G5), with a clear peak at 185 Hz for G5.

The spectral peaks interpreted as the structural response (40 Hz and 70 Hz for all surface sites) could be associated with widespread effects, such as the Green Bar layer, while the site effects observed at G4 and G5 reflect the difference in the intensity of the local fractures in the vicinity of the geophones.

A few months later the geophones G5 and G6 were moved dipper 1 m beyond the geophone G5. The idea was to trace the size of an anomaly located around G5 (Figure 4.4).

Figure 4.12 shows the spectral ratios between the seismic signals recorded in the solid rock and seismic signals recorded on the skin of the excavation for this new configuration (Figure 4.4 - Configuration II).

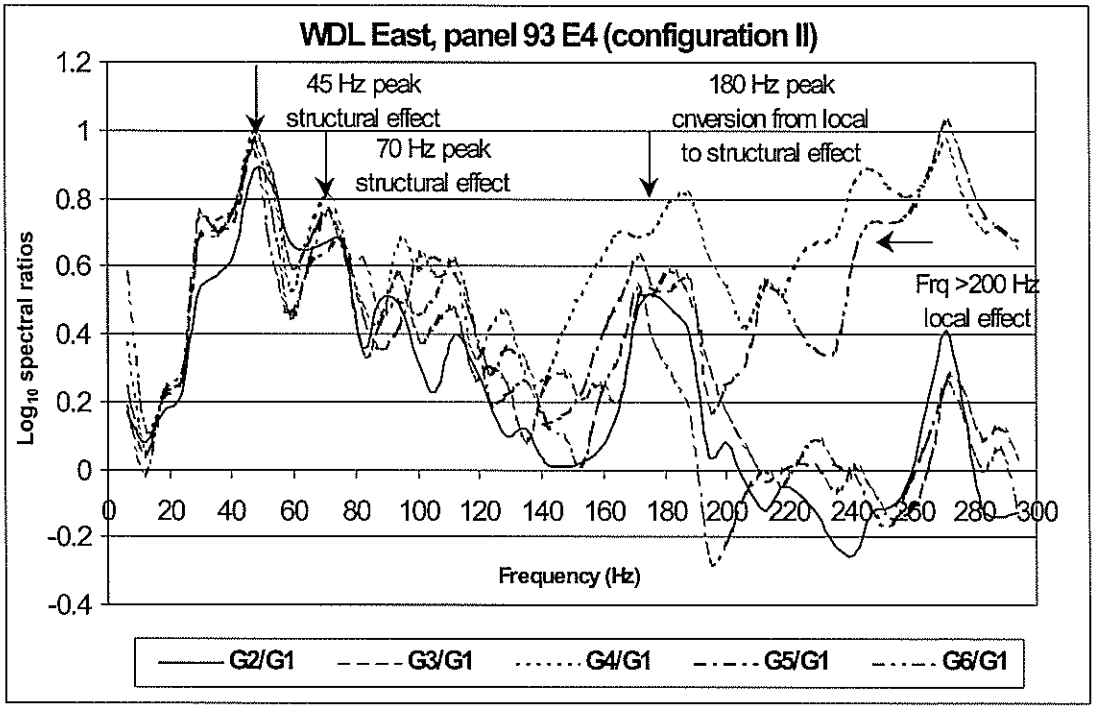

Figure 4.12 Log_{10}(spectral ratio) of the seismic signal recorded in solid rock (G1) and a number of seismic signals recorded at the skin of the excavation (G2, G3, G4, G5 and G6) for configuration II from Figure 4.4.

It can be seen from Figure 4.12 that the spectral peaks at 40 Hz and 70 Hz for all surface geophones remained the same as they were before. This indicates that the expected deterioration in the hangingwall and the support in time, does not effect the low frequencies.

Significant change is obtained for geophones G2 and G3, which have developed a spectral peak at 185 Hz. The spectral behaviour for G5 at its' new position is similar to G3, G3 and G4 in range of 185 Hz, while the spectral behaviour for G6 is similar to those of G4 for frequencies higher than 200 Hz. These changes are interpreted as local effect. However, the size of the affected area is apparently larger than the span of the surface network and cannot be accurately mapped.

The results obtained for the dynamic response of the site, including both the structural response and the local site effect, can be related to the existing support methodology. The normalised load-deformation curve, presently used as a support design criterion, could be modified by the dynamic response spectrum in order to provide additional design information.

4.1.6 Conclusions

The ground motion at points on the skin of a stope hangingwall was found to be some four to ten times larger than at a point 6,5 m into the hanging wall. Coda waves were also more developed on the skin. Measurements at 0,5 m, 2,5 m and 4,5 m showed intermediate behavior. It was suggested that the fracture zone acting as a wave-guide causes the enhanced levels of ground motion and that multiple scattering causes the prolonged duration of motion.

Ground motion on the abutment side of a fault in the hangingwall was much lower than the ground motion on the other side. Possible mechanisms involve the reduction of bedding-plane slip or the loss of seismic energy to the solid ground ahead of the abutment.

The results from velocity analysis have indicated that the time delays observed between pairs of geophone sites exceeded the travel time for P- and S-waves, in solid rock indicating lower wave velocities. These lower velocities are expected, given the high degree of fracturing near the skin of the stope. It is expected that this will give insight into the mechanisms of energy trapping. It will also assist in estimating the effective stiffness of the fractured rock and, thereby, it's dynamic response.

Two mechanisms of dynamic response have been defined: structural response, defined as a common spectral behaviour at all surface seismograms; and local site effect, defined by spectral peaks at one or two surface seismograms. The spectral peaks interpreted as the structural response (40 Hz and 70 Hz for all surface sites) could be associated with the presence of the Green Bar layer in the quartzite, while the site effects observed at G4 and G5 would be more dependent on the difference in the intensity of the local fractures in the vicinity of the geophones. However, this

interpretation is too broad and numerical modelling is required to provides insights into the actual mechanism of dynamic behaviour of the hangingwall.

The results obtained for the dynamic response of the site, including both the structural response and the local site effect, can be related to the existing support methodology. The normalised load-deformation curve, presently used as a support design criterion, could be modified by the dynamic response spectrum in order to provide additional design information.

4.2 Dynamic behaviour of pre-stressed elongates: underground measurements at Western Deep Levels, East Mine site

4.2.1 Introduction

One of the objectives of the site response project was to determine the performance of stope support under dynamic conditions. This kind of study is not a direct evaluation of the site response, but that of the response of support units under different conditions. The interaction of the support unit with the hangingwall and the footwall during the seismic event is still not well understood. Some of the support units used to support the stope during mining are elongate props. By recording the motion taking place in the hangingwall, the prop, and the footwall simultaneously, it is possible to gain better understanding of the interaction between these sites. Because differences between these sites may be frequency dependent, data analysis was done in the frequency domain.

4.2.2 Data

An experiment was conducted at Western Deep levels East Mine (93 level E4) to assess the behaviour of the Eben Haeser prop and the "pencil stick" prop during a seismic event. Figure 4.13 shows a schematic diagram of the experimental set-up.

The diagram shows vertical geophones attached to the hangingwall, the props and the footwall. The props were separated by about 1,6 m. Thus for seismic wavelengths of interest the footwall and hangingwall motions should be similar for both sites. The site was instrumented two weeks after the props were installed. Therefore, a considerable amount of yielding had taken place and the props were expected to be supporting close to their maximum load carrying capabilities.

Channels to which the geophones record motion were numbered consecutively from G1 to G8. A total of 542 events were recorded and analysed. Channel 5, recording the footwall close to the pencil prop did not perform consistently. This meant that there was a reduction in the number of events when this channel was included in the analysis. However there was still enough data to provide a realistic analysis. Amplitude spectra, spectral ratios between channels, and phase differences were used as analysis tools.

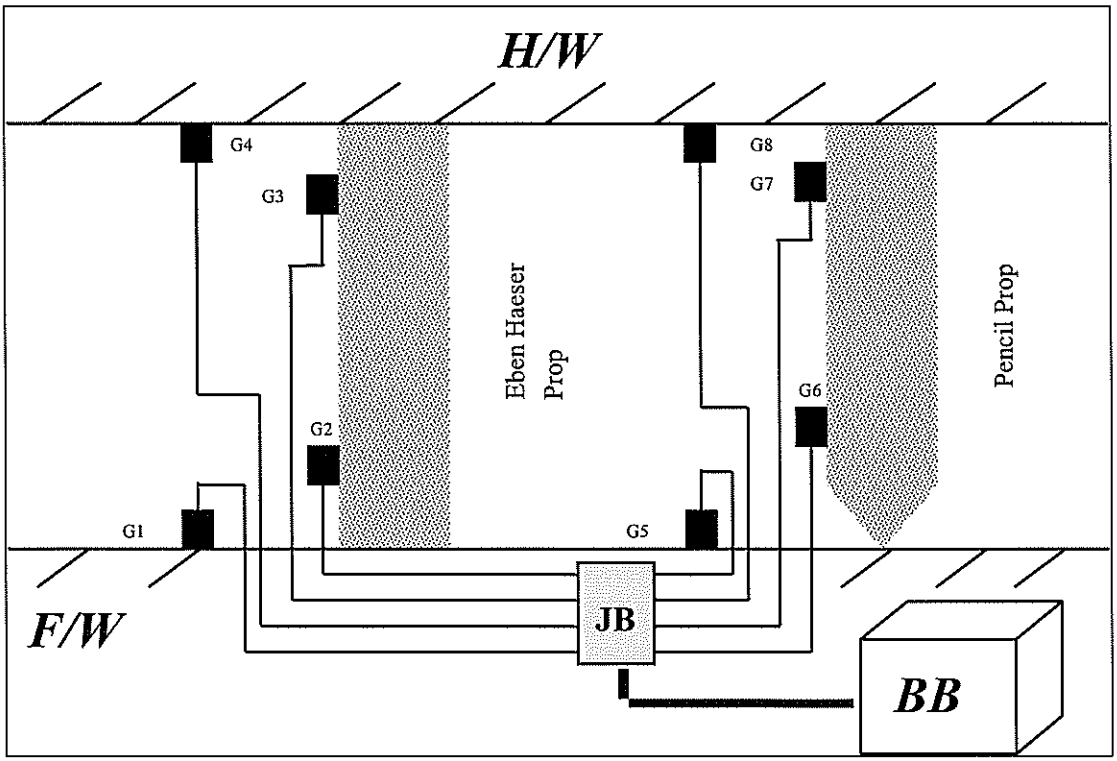

Figure 4.13 A schematic diagram shows the instrumentation of the props, the footwall and the hangingwall. An 8 channel Ground Motion Monitor connected to 8 uniaxial vertical geophones was used. The geophones were connected to the box via a junction box (JB).

4.2.3 Analysis

The amplitude spectra for each channel is calculated and plotted them on the same graph. The spectra were calculated for each event in the data set and the average value of all the events was evaluated. In Figure 4.14 (a) the spectra of the first four channels, corresponding to the Eben Haeser prop and its surrounding footwall and hangingwall were plotted. The thick dashed line is a footwall channel while the thin dashed line is the hangingwall channel in the vicinity of the prop. Similar graphs are plotted in Figure 4.14 (b) and correspond to the next four geophone channels situated on and close to the pencil prop.

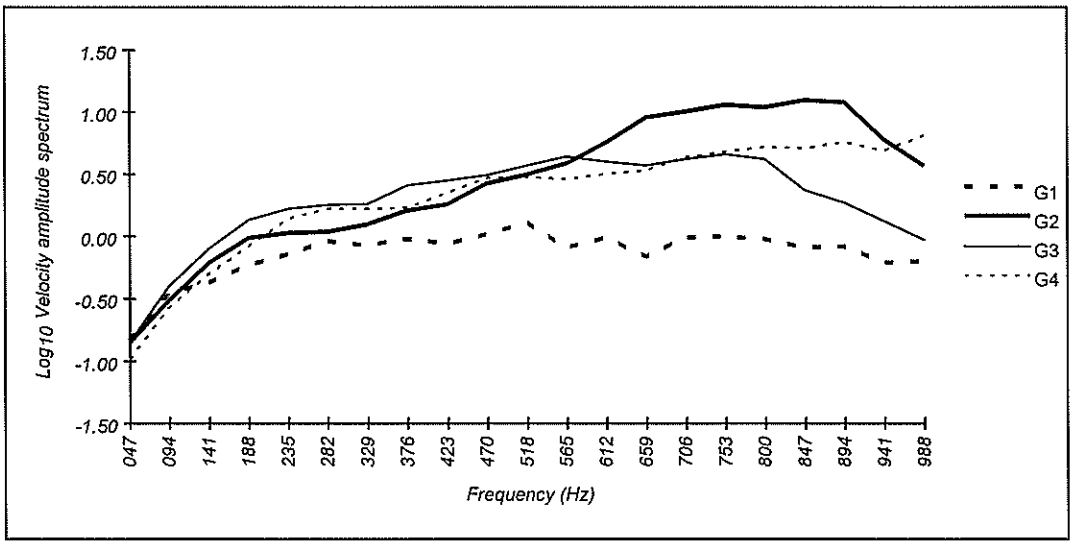

Figure 4.14 (a) Log_{10} velocity amplitude spectrum of the channels recorded on and close to the Eben Haeser prop.

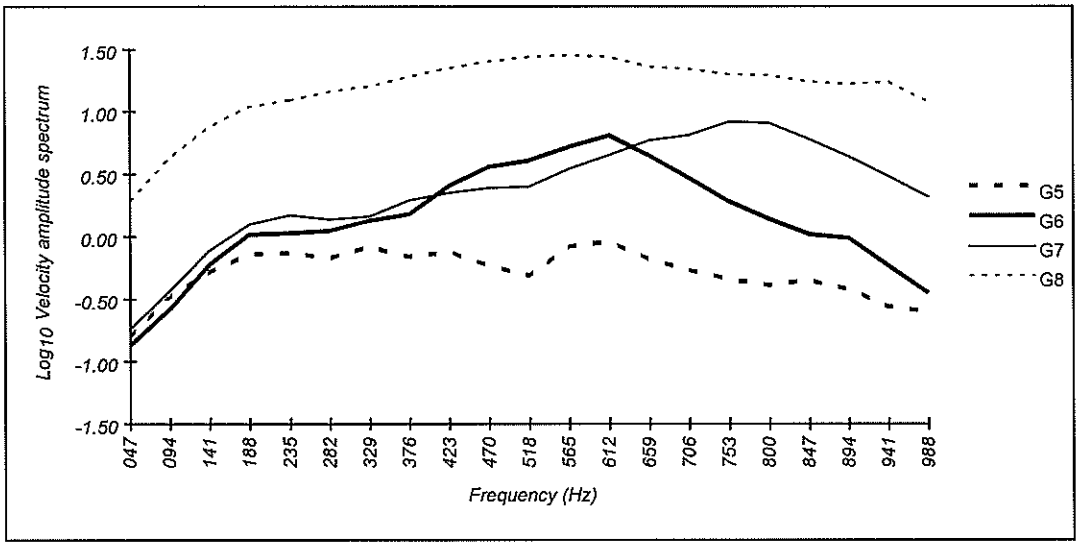

Figure 4.14 (b) Log_{10} velocity amplitude spectrum of the channels recorded on and close to the pencil prop.

For the Eben Haeser prop the spectra for the hangingwall and the two prop geophones are similar for frequencies below 560 Hz. The energy increases steadily with frequency for all of the three channels. This is perhaps representative of the energy distribution in the input signal. As far as the prop is concerned, the input signal comes from the combined hangingwall and footwall contributions. It can be seen that the footwall channel is generally flat from 181 Hz onwards and is of lower amplitude compared to the other three channels. Above 560 Hz, the prop channel close to the footwall "seems" to have higher energy than all the channels. This is only possible when there is constructive interference of the footwall and hangingwall signals at these frequencies.

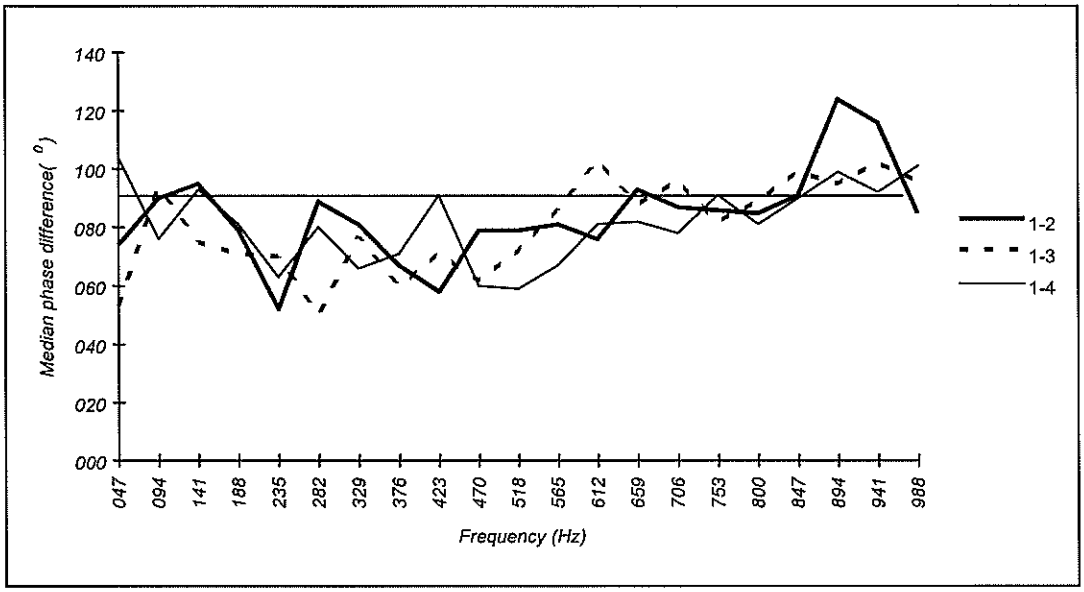

Figure 4.15 (a) Median phase differences between the footwall channel 1 and other channels at the Eben Haeser prop site.

The scenario emerging from this interpretation is that the lower and upper geophones on the prop and the hangingwall have similar amplitude spectra. It is reasonable to assume that the prop motion should be some form of superposition of the hangingwall and footwall motions. If this is the case here, the resultant prop motion is dominated by the hangingwall motion even for the part of the prop close to the footwall. This may be owing to the lower amplitudes in the footwall motion.

Figure 4.15 (b) shows the amplitude spectra of channels situated close to and on the pencil prop. The hanging wall channel has higher energy than the channels of the Eben Haeser prop (Figure 4.14 (a)) at all frequencies. This is a classic display of the site effect in that the two hangingwall sites have a different response even though they are only 1,6 m apart. A further comparison of Figure 4.14 (a) and Figure 4.14 (b) shows that the footwall amplitude responses at the two sites are relatively similar. The top and bottom channels on the "pen sick" prop have the same amplitude spectra as their corresponding Eben Haeser prop channels. Hence this change in the hangingwall input does not seem to affect the response of the prop. One explanation of this is that the change in the prop response may depend on the significance of the change in input motion, i.e., if the hangingwall spectrum at the pencil prop site was very different from that at the Eben Haeser prop.

The important thing though, is that the prop that supported higher amplitude ground motion responded similar to a prop that supported lower amplitude ground motion.

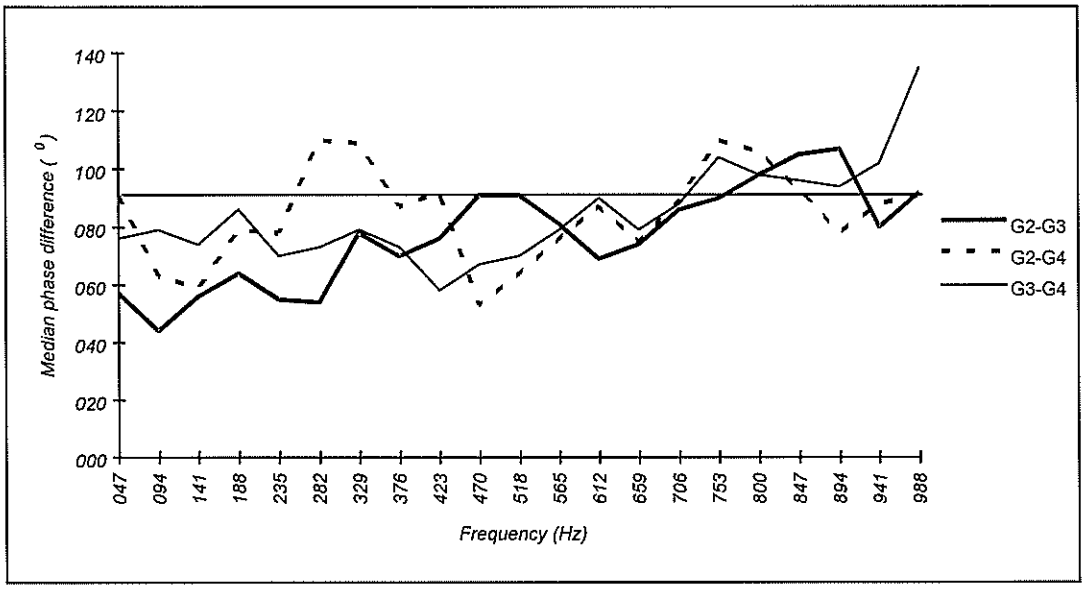

Figure 4.15 (b) Median phase differences between the two prop channels and the hangingwall channel at the Eben Haeser prop site.

Figure 4.15 (a) and Figure 4.15 (b) show phase differences between various channels at the Eben Haeser prop site. There is no phase correlation in the motion at any of the frequencies in the range. A similar situation is obtained for the pencil prop site as shown in Figures 4.16 (a) and Figure 4.16 (b).

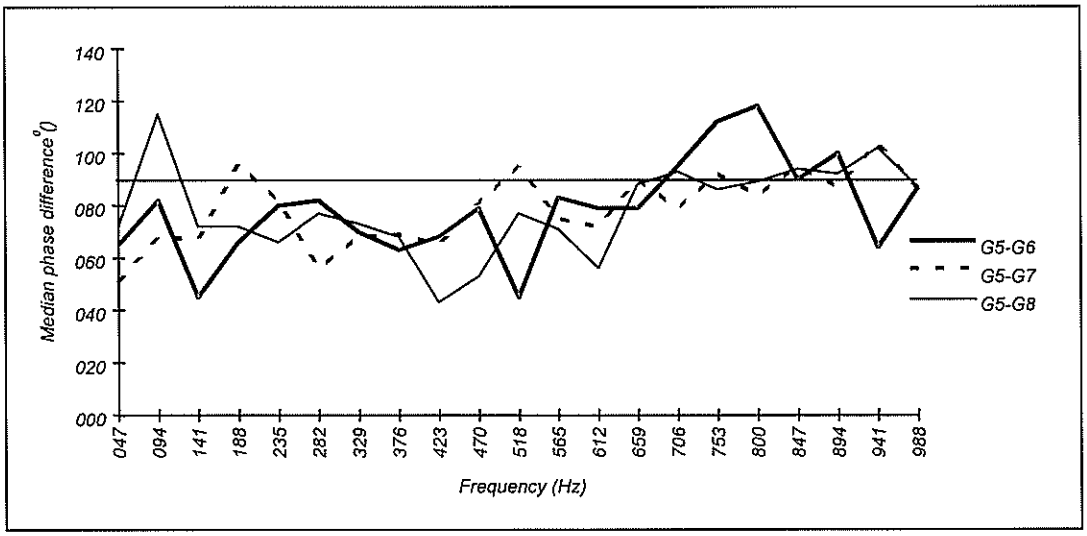

Figure 4.16 (a). Median phase differences between the footwall channel 5 and other channels at the pencil prop site.

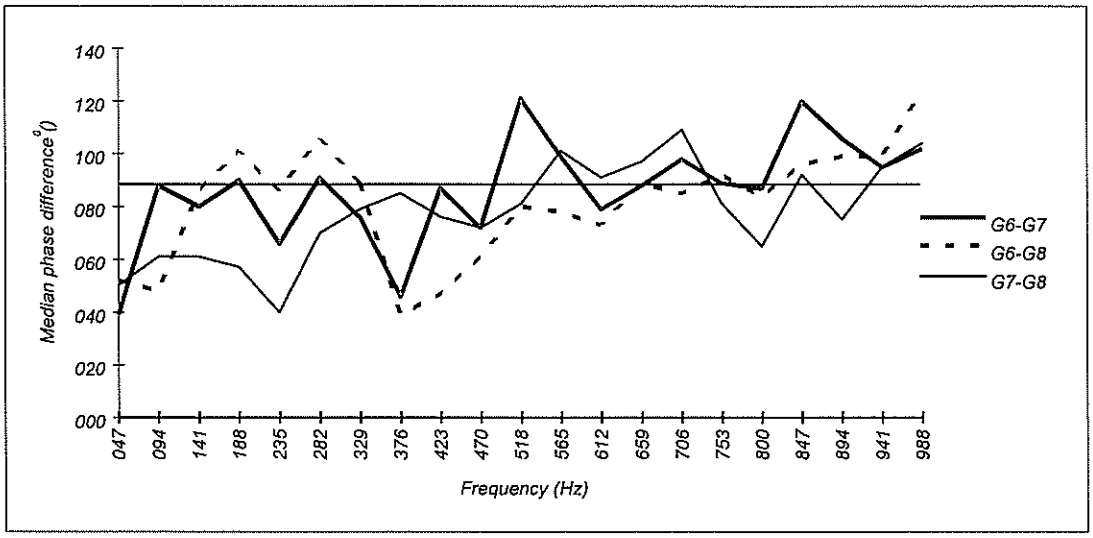

Figure 4.16 (b). Median phase differences between the two prop channels and the hangingwall channel at the pencil prop site.

4.2.4 Conclusions

A prop supporting higher levels of ground motion (as shown by its amplitude spectrum) may have the same amplitude response as one supporting lower ground motion.

During an event, the prop motion may be uncorrelated with the input motion. This is indeed related to the fact that the input motion at the two ends of the prop is uncorrected.

4.3 Triaxial measurements of peak particle velocities in underground tunnel: Kloof Gold Mine

Ground motion monitors were installed in a tunnel in order to analyse support behaviour under dynamic (seismic) loading. Three triaxial geophone boats were installed on both sidewalls and the hangingwall in a tunnel at Kloof gold mine.

Initially only the western wall was instrumented, with the eastern and hangingwall instrumented two weeks later. Within a month of recording, mining in the area was

stopped. This led to a decrease in the number of seismic events. In three months, 92, 58 and 45 acceptable events were recorded on the eastern western and hangingwall respectively.

On the hangingwall the two horizontal directions have the same peak velocities. Unfortunately the vertical component, perpendicular to the hangingwall had resonance due to poor installation of the geophone.

The eastern and western walls show a very slight difference between the two tangential components. The component parallel to the length of the tunnel shows higher peak velocities than the one perpendicular to that direction. Interestingly, perpendicular components do not show high peak values associated with the free surface.

4.3.1 Introduction.

A seismic wave may cause damage to all kinds of underground excavations, including service tunnels. Understanding how the tunnel behaves during a seismic event may shed light on how best to support the tunnel to sustain dynamic loading. Since the rock surrounding the excavation is not homogeneous, the seismic response of the tunnel is expected to vary with position. It is therefore important to understand these variations in order to understand damage owing to a seismic wave. To achieve this, factors such as the position of the tunnel with respect to the seismic event, differences in interaction of waves with different walls of the tunnel, the frequency content of seismic waves, etc., must be investigated.

A complete description of motion at any point (small volume) in solid ground is achieved by recording three components of the motion at that point. On the surface of an excavation, recording motion perpendicular to the ground, and tangential motion in two mutually orthogonal directions usually achieves this. In this way a comparison of motion between the three directions at the same site can be made in order to determine the component that is more diagnostic of seismic damage. This study attempts to address that aspect of site response. The main parameter used in this investigation is the peak velocity. For purposes of this study, the peak velocity is defined as the absolute value of the largest excursion along the seismogram. This

means that when two seismograms are compared with each other, the position and the sign of the peak value are not necessarily the same for both events. This further assumes that the input signal at a site is the same for all components and that the differences between the seismograms emanate from the site. However, with surface recorded Ground Motion Monitor seismograms, it is difficult to separate the P- and S-waves because most of the triggered events are short distance events which reach the recording sites before enough P/S separation has taken place. Added to this is non-linear distortion caused by the fractured zone. It is however thought that the site effects (despite the presence of source effects and inaccurate peak velocity estimates) still contribute a great deal to observed differences.

4.3.2 Site description.

A cartoon showing how the experiment was set up is shown in Figure 4.17 (a) depicting how triaxial geophones were laid out on the surface of the tunnel. Three triaxial sets were attached to the eastern, western and hanging walls. Each triaxial geophone set is connected to a separate Ground Motion Monitor. Figure 4.17 (b) is a plan view of the experimental site, shown as a dashed rectangle, together with its immediate surroundings. The faces being advancing semi-parallel to the footwall tunnel being monitored with all mining activity taking place to the East Side of the tunnel. This led to the assumption that most of the seismic events recorded in Ground Motion Monitors placed at the experimental site emanate from the eastern side of the tunnel.

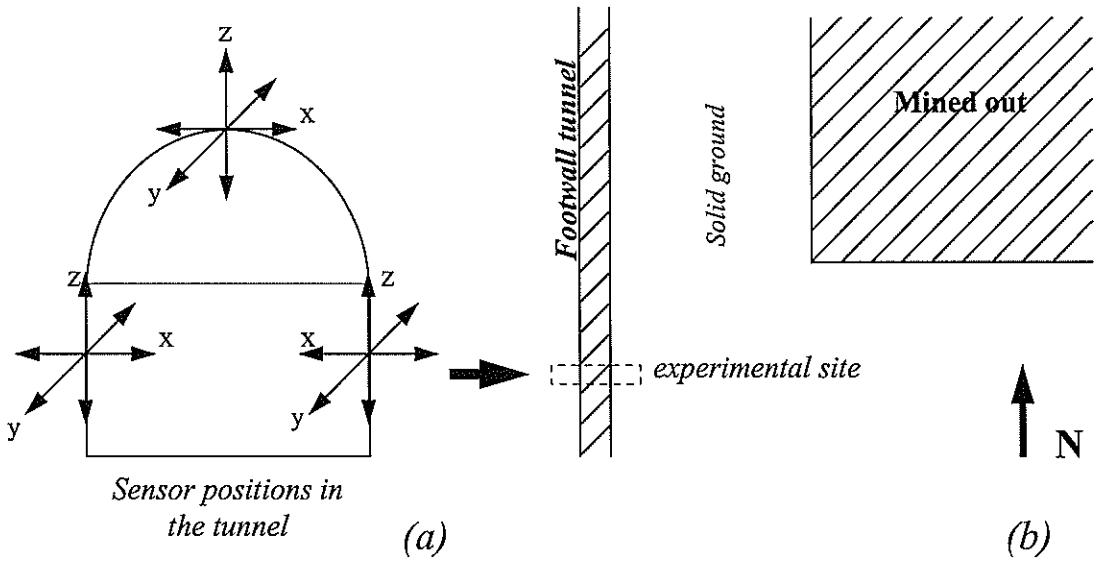

Figure 4.17 Experimental setup (a) showing the cross-section of a tunnel with triaxial sensor positions; (b) plan view of the experimental site and its surrounding areas. The diagrams are not drawn to scale.

4.3.3 Data

The site had been chosen to assess changes in the response of the tunnel skin to seismic waves as the tunnel deformed owing to changing stress conditions imposed by mining of the stope 40 m to the east of the tunnel. Mining advances due south. Ground motion monitors were placed about 25 m ahead of the approaching mining face. At first only the western wall of the tunnel was instrumented with the hanging wall and the eastern wall following two weeks later. Within a few weeks of recording, the mining stopped in this area. This reduced seismicity. In three months the Ground Motion Monitor on the eastern wall recorded 92 "good" events. The western wall and the hanging wall boxes recorded 58 and 45 "good" events respectively. The lower number of events being owing to the fact that the latter two boxes were only installed two weeks after the eastern wall box had been installed. There was no correlation between events recorded by the seismic network and Ground Motion Monitor events. Thus location of the Ground Motion Monitor events was not possible.

4.3.4 Results

Results from the two sidewalls will be discussed first. Peak velocities of the 3 components of ground motion were plotted on the same graph. The x component, which is ground motion perpendicular to the sidewall, was used as a reference component against which the other components were plotted. Figure 4.18 (a) and Figure 4.18 (b) correspond to eastern and western walls respectively.

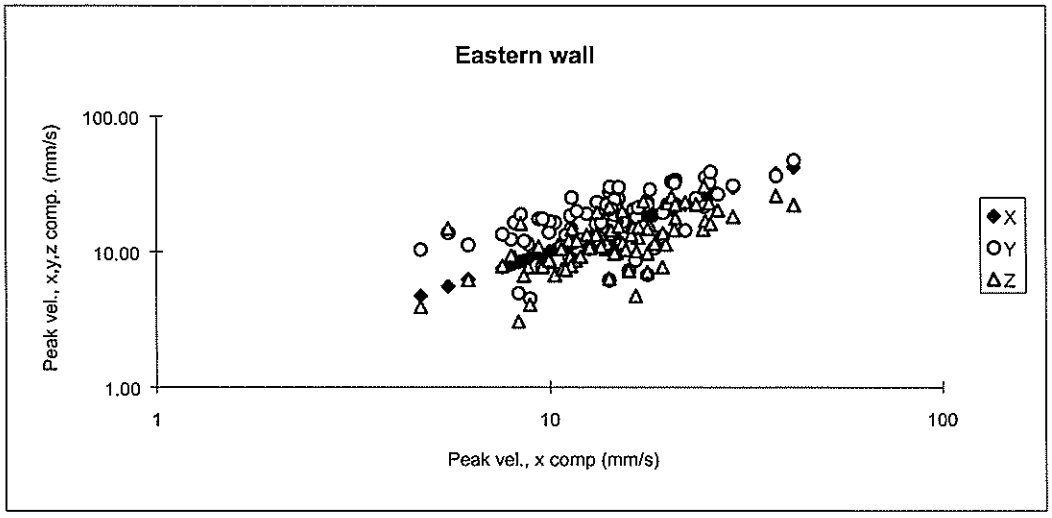

Figure 4.18 (a) Peak velocities of three mutually orthogonal components of the eastern sidewall site plotted on the same graph.

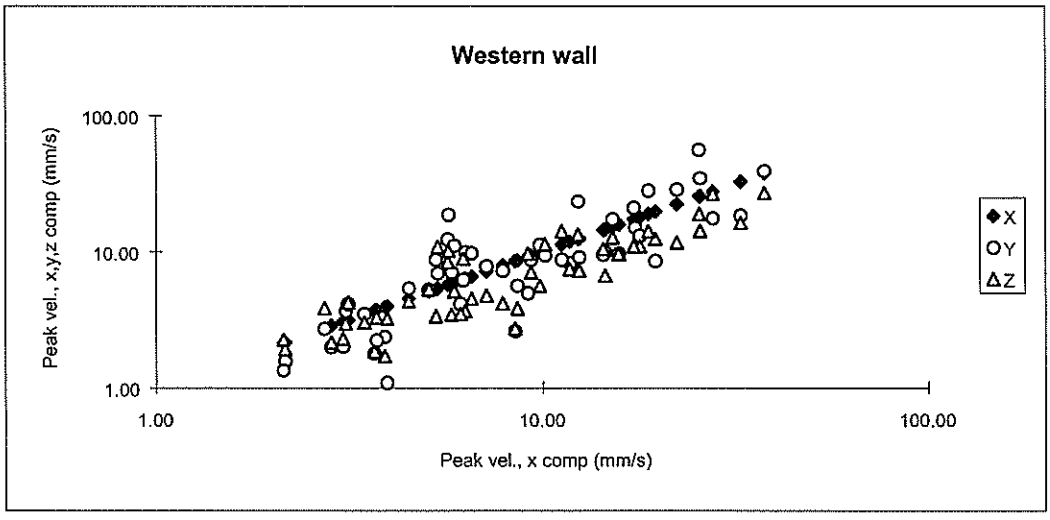

Figure 4.18 (b) Peak velocities of three mutually orthogonal components of the western sidewall site plotted on the same graph.

Both Figure 4.18 (a) and Figure 4.18 (b) show that the y component is generally higher than the x component and that the z component is generally lower than the other two components. It was found that the largest value of the y component is nearly twice as large as the corresponding largest x component value. Generally the y component, whose motion is confined by the surrounding rock, is not expected to have higher ground motion than the x component, whose motion is in the free surface direction. The tunnel wall is expected to fail mainly owing to movement perpendicular to the surface of the wall which causes ejection of the rock into the void. That this is not the case here may be due to location of the events relative to the recording site. Unfortunately this could not be verified because of lack of location data. However for this mining geometry, most of the events were expected to locate some 20 m to the north of the tunnel and between 20 to 50 metres to the east. This gives the angle of incidence of between 45^0 and 60^0. If this hypothesis were true, it would add another dimension to the site response and seismic damage hazard problems.

For the hanging wall site only the x and y components have been plotted. The z component was omitted because of a strong resonance which meant that amplitudes from that component were not reliable. The x and y components are tangential while the z is perpendicular to the surface. Figure 4.18 (c) shows that peak values of the two components are generally equal.

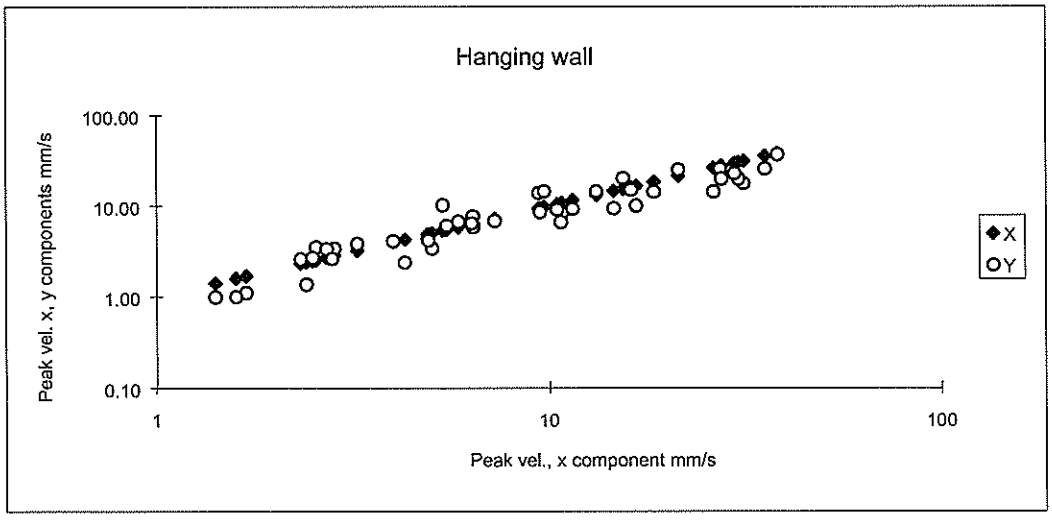

Figure 4.18 (c) Peak velocities of two mutually orthogonal components of the hanging wall plotted on the same graph. The component perpendicular to the surface had resonance.

Furthermore, a comparison between the western and eastern sidewalls was done. Peak velocities of events common to both walls were plotted on the same graph. Channel by channel plots was done. These graphs are shown in Figure 4.19 (a), Figure 4.19 (b) and Figure 4.19 (c).

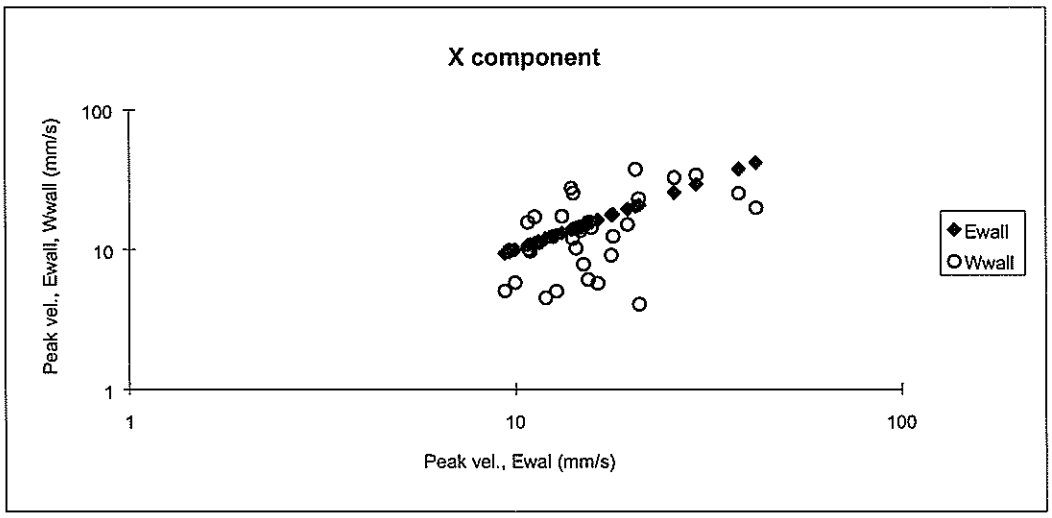

Figure 4.19 (a) Peak velocities of events common to eastern and western walls recorded perpendicular (x component) to the walls.

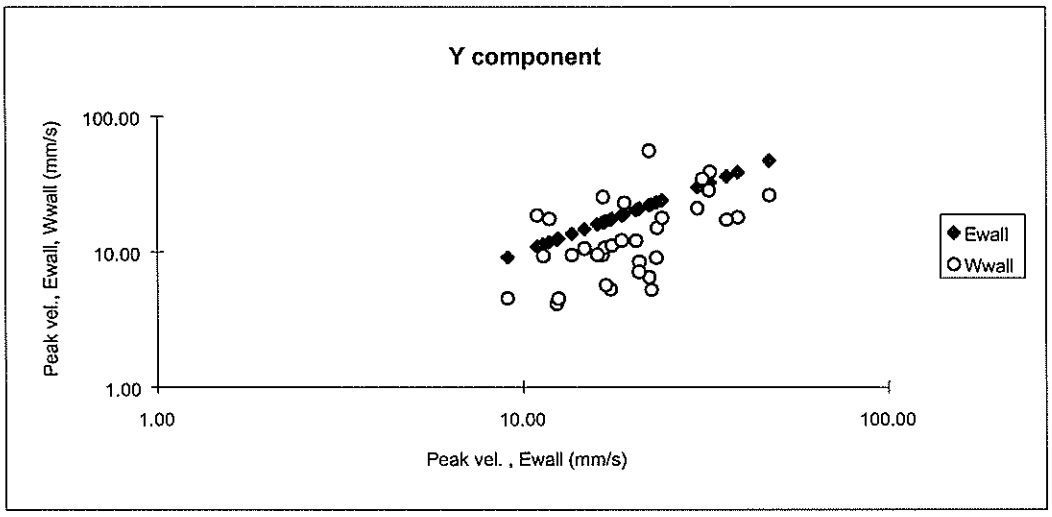

Figure 4.19 (b) Peak velocities of events common to eastern and western walls recorded tangential (y component) to the walls

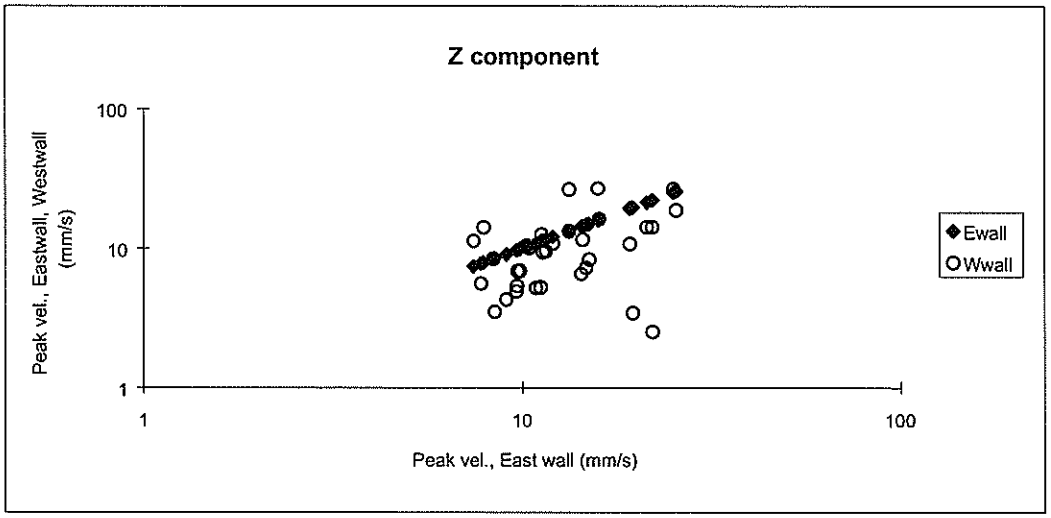

Figure 4.19 (c) Peak velocities of events common to eastern and western walls recorded tangential (z component) to the walls.

The eastern wall was used as a reference against which the other wall was plotted. All three channels show that western wall peak velocities are scattered around the linear plot of the reference eastern wall. This indicates that peak velocities recorded on one wall are not equal to peak velocities recorded on the other wall. However, the scatter seems to be random around the reference line with no definite trend. Visual inspection of a few waveforms from this data set did not readily show a change in the shapes of waveforms. Better tools are needed for this kind of analysis.

Spectral analysis of the data was done. Amplitude spectra of all the events in the data set were calculated and their average values were obtained for the frequency range. Firstly, events common to both sidewalls were considered. Figure 4.20 (a) shows the average of the spectra of events common to both sidewalls. Spectra from both walls have the same general shape with the western wall displaying slightly higher amplitudes at frequencies greater than 300 Hz. Figure 4.20 (b) shows a plot of all the events recorded at each sidewall. A similar situation to that in Figure 4.20 (a) was obtained. Therefore, spectral analysis shows that the two sidewalls behave relatively similarly. Most of the energy is in lower frequencies, below 300 Hz. Slight deviations between the walls occurs at higher frequencies.

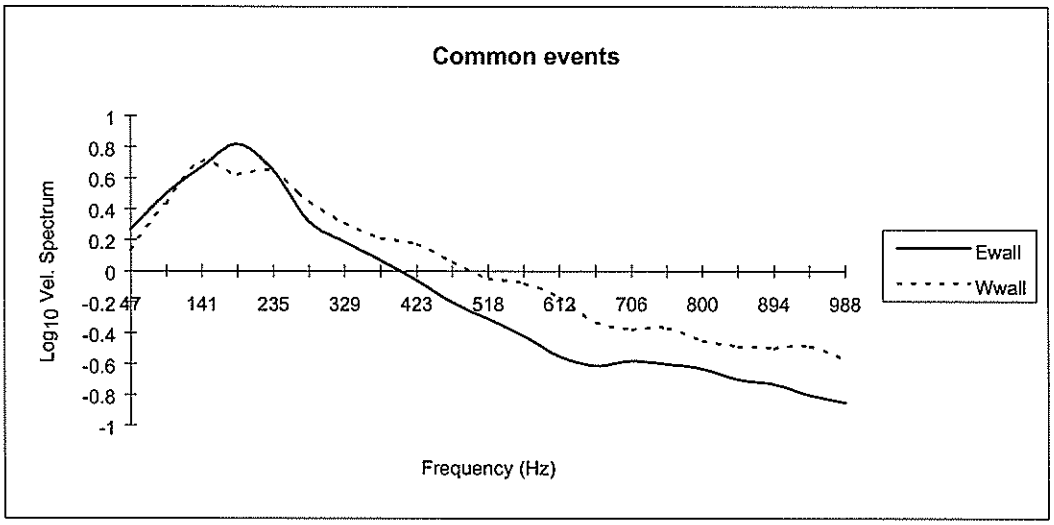

Figure 4.20 (a) Log_{10} average velocity spectra of events from the eastern wall (solid line) and events from the western wall (dashed line). Only events common to both walls were considered

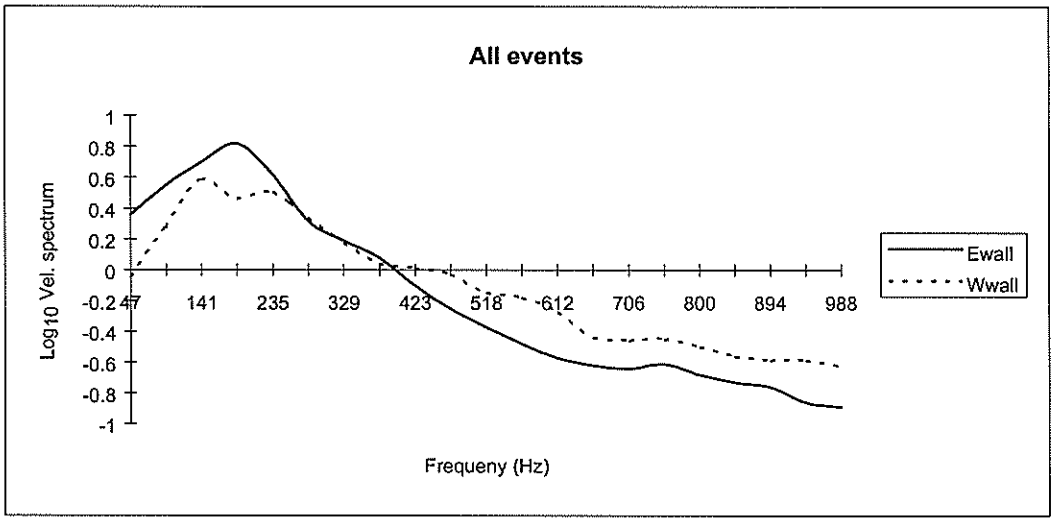

Figure 4.20 (b) Log_{10} average velocity spectra of events from the eastern wall (solid line) and events from the western wall (dashed line). All events recorded at the walls were considered.

4.3.5 Conclusions and discussions

Peak velocities may be affected by the position of the event source relative to the wall of the excavation. This directional dependence means that some parts of the excavation may be more hazardous than others. Spectral analysis shows that the both sidewalls of the tunnel behaved relatively similarly. However this will depend mostly on the frequency content of the incident wave as well as on the direction (position) of the source relative to the tunnel. A complete analysis of these phenomena requires location data and a reference geophone embedded in the solid rock.

5 New interpretation techniques and developments

5.1 Rock mass behaviour under seismic loading in a deep mine environment

5.1.1 Summary

The dynamic behaviour of the rock mass surrounding a stope has been studied in a deep South African gold mine. The three-dimensional seismic network installed at Western Deep Levels East Mine, affords a unique opportunity to examine the change in the wave front close to an underground opening. A set of three-component sensors installed in a borehole above the panel reveals the development of surface waves as the wave front reaches the excavation. An array of vertical component sensors installed on the hangingwall of the excavation provides a two-dimensional image of site effects. The collected data did not include damaging seismic events. Quantitative analysis of the data, however, enables phenomena to be recognised, which could lead to damage.

In the vicinity of the excavation, the energy of the seismic signal is generally transformed from high frequency to low frequency. A strong structural effect is expressed by the well-developed coda of low frequency (at 40 Hz and around 60-70 Hz) at the skin of the hangingwall. The strong low frequency component is not present on records from stations located in solid rock.

A seismic source with relatively high corner frequency (150 Hz-200 Hz) usually excites several modes from 30 Hz to 110 Hz in the hangingwall of the excavation. The seismic sources with low corner frequency (30 Hz-50 Hz) do not always excite higher modes of vibration in the structure. This implies that the rock mass around the excavation is a complex medium, and should be studied using the multi-degree-of-freedom model.

The site effect is defined as a change in signal properties from station to station located in the hangingwall. The site effect usually produces strong resonance around 160 Hz and in a frequency range from 200 Hz to 300 Hz. This effect causes the relative displacement between blocks surrounding the excavation. Time domain analysis of the seismograms, using the transfer function technique, confirms site effect resonance.

Apart from the structural and site effects, the distance of seismic source from the excavation also has a significant influence on vibration.

5.1.2 Introduction

One of the most important problems encountered in engineering seismology is the prediction of ground motion parameters at the site of interest. The classical approach is to evaluate peak ground velocity as a function of distance between source and station (R) and magnitude of seismic event (M) (Kaiser, 1993). In this type of equation, the stress drop of the seismic event ($\Delta\sigma$) often replaces the magnitude as stress drop relates directly to peak ground velocity (McGarr et al., 1981). No damage is expected when peak ground velocity is small. However, records of falls of ground collected at East Rand Proprietary Mine show that peak ground velocities as small as 0,005 m/s can cause damage (Cichowicz, 1995).

The estimations show that most damage occurred at peak ground velocity smaller than 1 m/s. Similar low values of damaging peak ground velocity were estimated by Butler and Van Aswegen (1993). These estimations came from the V_{max} ($\Delta\sigma$; R) relationship, which is only applicable for far field seismic stations located in solid rock. However, the presence of the free surface, fractured rock surrounding the excavations, and the geometry of the excavation influence the ground motion at the excavation wall. These phenomena can cause unusual amplification of ground motion parameters at the site (Durrheim et al., 1996).

The following procedures were applied to analysis of the seismic data:

- study of the anatomy of the seismograms to identify body and surface waves
- three-dimensional image of ground motion
- filtration of the velocity signal with a band pass Butterworth filter
- spectral analysis
- interpretation of surface wave
- one-dimensional and two-dimensional resonance
- mode analysis

5.1.3 Three-dimensional image of ground motion

The three-dimensional seismic network installed at Western Deep Levels, East Mine, 93 E 4 panel, gives the unique opportunity to examine the change in the wave form close to an underground opening. Standard analysis of wave propagation was used to explain the effects experienced by waves as they propagate through a section of a structure.

Four three-component sets of geophones were installed in a borehole (Figure 4.5). The deepest set of three sensors (station A) used in analysis was installed at a depth of 6,5 m. The shallowest set (station D) was installed at a depth of 0,5 m. Stations B and C were located between station A and station D, 2 m apart. The amplitude of the ground motion is expressed in units of mm/s. Another array of five vertical geophones was installed on the skin of the hangingwall in the vicinity of the borehole mouth. Additionally, one vertical geophone was installed on the footwall. The sensors on the skin of the hangingwall were connected to the Ground Motion Monitor (Milev et al., 1998).

After adjustment of time and amplitude scales of both systems, it was possible to the compare waveforms recorded in the vertical borehole array, with the corresponding waveforms recorded at the skin of the excavation.

Data from the vertical array (Figure 5.1) shows records with well-developed groups of P- and S-waves. The group of body waves is followed by low frequency surface waves.

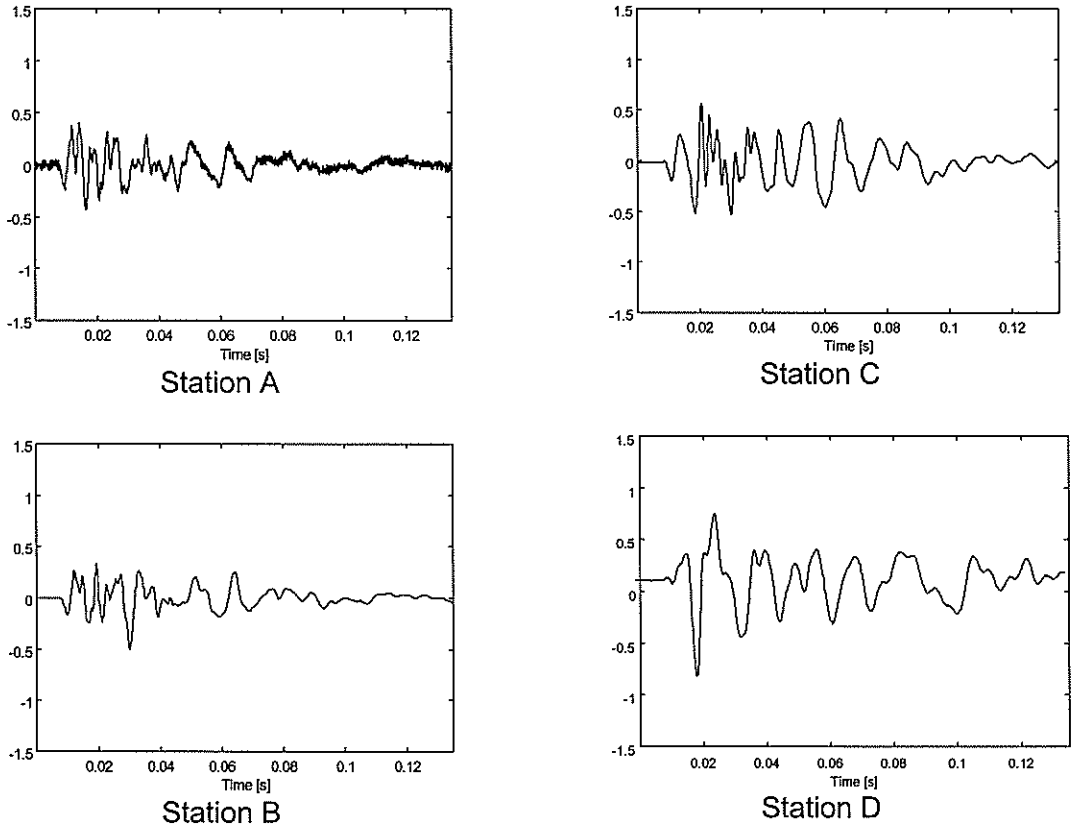

Figure 5.1. Seismograms recorded by the Portable Seismic System (borehole array, vertical channels). Stations A, B, C and D are located from the top to the bottom.

There are several points in time where the amplitude of the group of body waves shows a sharp change in phase - these points are associated with new arrivals. This indicates that the structure is rather complex and also that the seismic events are located close to a three-dimensional array. The sites A and B have almost identical waveforms. A straight extrapolation from the waveform of station B to the waveform of station C or station D is difficult, because the latter sites have additional impulses

associated with the latter part of the body-waves group. This complication could be associated with the presence of the Green Bar which is much softer than the surrounding quartzite. (Schweitzer et al., 1997).

The set of three-component sensors installed in the borehole shows the development of the surface wave as the wave front reaches the excavation. Consequently, energy of the seismic signal is transformed from high frequency to low frequency in the vicinity of the excavation. This transformation depends on the frequency content of the signal generated by the seismic source. After the arrival of the body wave group, there is a low frequency strong pulse or several pulses in the vertical geophones. In general, the horizontal components have the same degree of complexity.

A well-developed low frequency coda, not present in the vertical borehole above the panel, can be observed at the skin of the hangingwall (Figure 5.2). The absence of strong coda waves in records of the top sensors in the vertical hole suggests that these waves propagate primarily close to the surface and can be categorised as surface (probably Rayleigh) waves.

It is also important to notice that the surface wave amplitude can be greater than the body wave amplitude in the skin of the hangingwall.

The two-dimensional image of site effects is shown by means of vertical ground motion recorded at the skin of the hangingwall (Figure 5.3). Channel 2, which has been installed close to the borehole as an extension to the vertical array, shows a waveform very similar to that of station D. Channels 2, 3 and 6 are similar, but channels 5 and 4 show strong site effect.

For a number of seismic events, the ratio of the peak ground motion recorded in the skin of the hangingwall (channels 2,3 and 6) to the corresponding peak value in the solid rock, has been calculated. The ratio of the peak velocity ranges from 0,7 to 4,5 and the amplification factor depends on the dominant frequency of the seismic event. The lower, the dominant frequency of a seismic event, the stronger the amplification at the skin of the hangingwall.

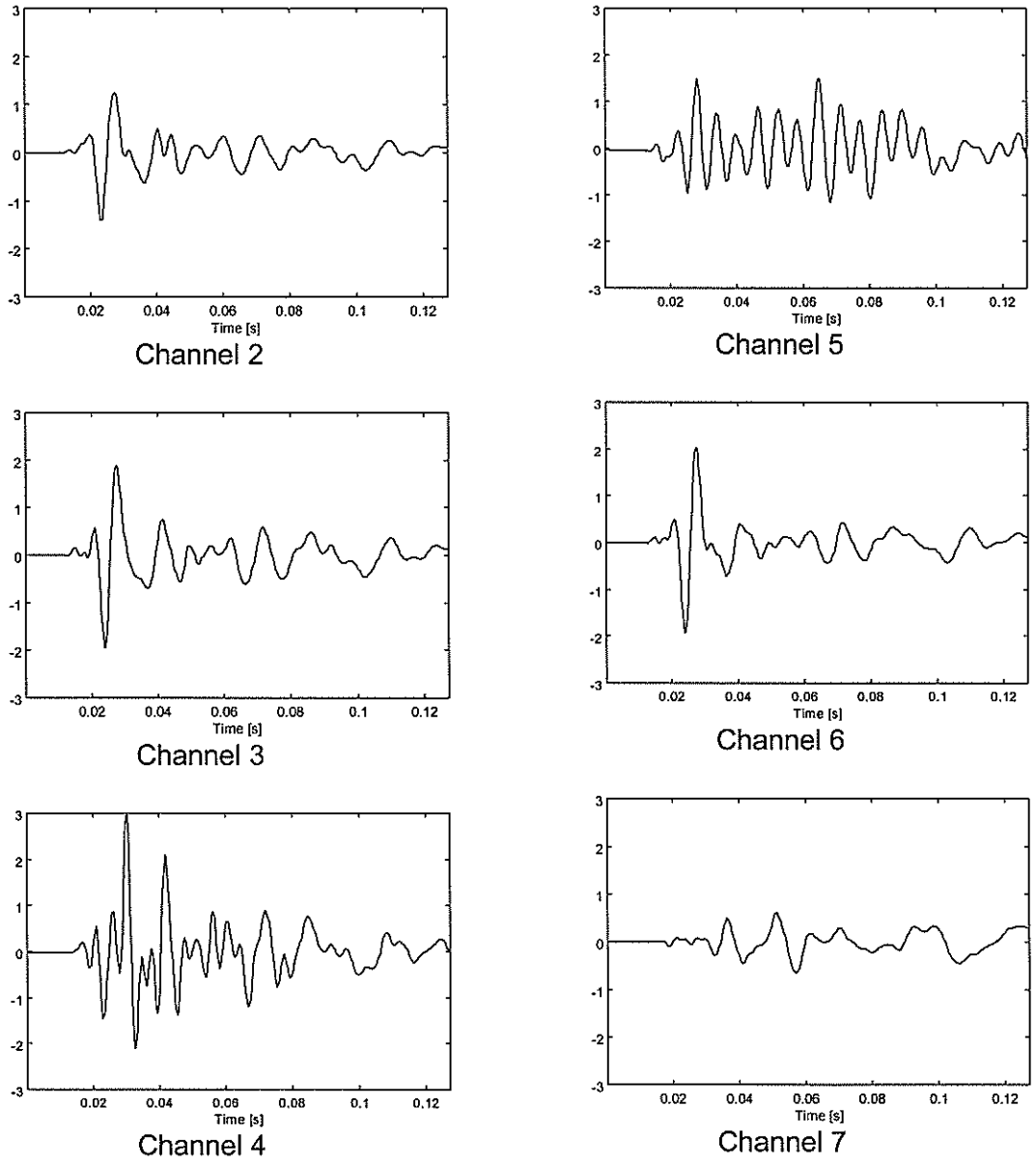

Figure 5.2 Seismograms recorded by the Ground Motion Monitor (surface array, vertical channels). Channels 2, 3, 4, 5 and 6 are located on the skin of the hangingwall and channel 7 is on the footwall.

5.1.4 Spectral analysis of the three dimensional ground motion

Spectral analysis was carried out on all the records. The objective of this analysis was to identify common features responsible for the structural effect and the site effect in the frequency domain.

Data from the borehole array were used to identify the dominant frequency of the seismic source. This task, which is performed routinely in the study of seismic source parameters, gives uncertain results. At station A, the vertical component of the seismograms is controlled by source properties and by structural effects. Therefore, the group of body waves recorded by the horizontal components was used to calculate the corner frequency of the seismic source (see the second column of Table 5.1).

Table 5.1

Spectral peaks from the vertical borehole array (Portable Seismic System data). The peaks without letters indicate that amplification was observed at all geophones, letter D or C indicates that the peak was observed only at that particular geophone.

Event Number	f_o [Hz]	Body Wave Peaks [Hz]	Surface Wave Peaks [Hz]
5243	120-180	105 (200 280 400)C	40 70
5361	200	70-80 (220 400)C	45 60
5384	120-200	60	40 70
5509	200	70-80 140D (180 280 350)C	50 80D 90C
5634	100-200	70-80 140D (180 280 350)C	45 80D 90C
5635	200-350	70-80 140D (200 280 350)C	40 60

Spectra of the vertical components of the borehole array were obtained separately for the body wave group and the surface waves. Table 5.1 shows the spectral peak for both groups. The peaks without letters indicate that amplification was observed at all geophones, letter D or C indicates the peak was observed only at that particular geophone.

The body wave group has a systematic peak around 70 Hz, which does not relate to the corner frequency of the seismic source. At station C, spectra have several systematic peaks, which could be related to the interaction of the seismic wave with the Green Bar. Station D often has amplification at 140 Hz.

The image given by spectra of the surface wave clearly indicates that there are usually two strong peaks at 40 Hz and 60-70 Hz, and obviously the surface wave carries information about structure.

The amplitude of the surface waves recorded by the vertical components increased from station A to station D. The surface waves amplitudes at station A are half those of station D. In addition, there is a significant difference between the amplitude spectra of station A and station D. On average, the peaks of surface spectra are about 6 to 11 times stronger at station D than the peaks at station A. Figure 5.3, shows a systematic peak increase of the 70-80 Hz as the geophones approaching close to the skin of the excavation.

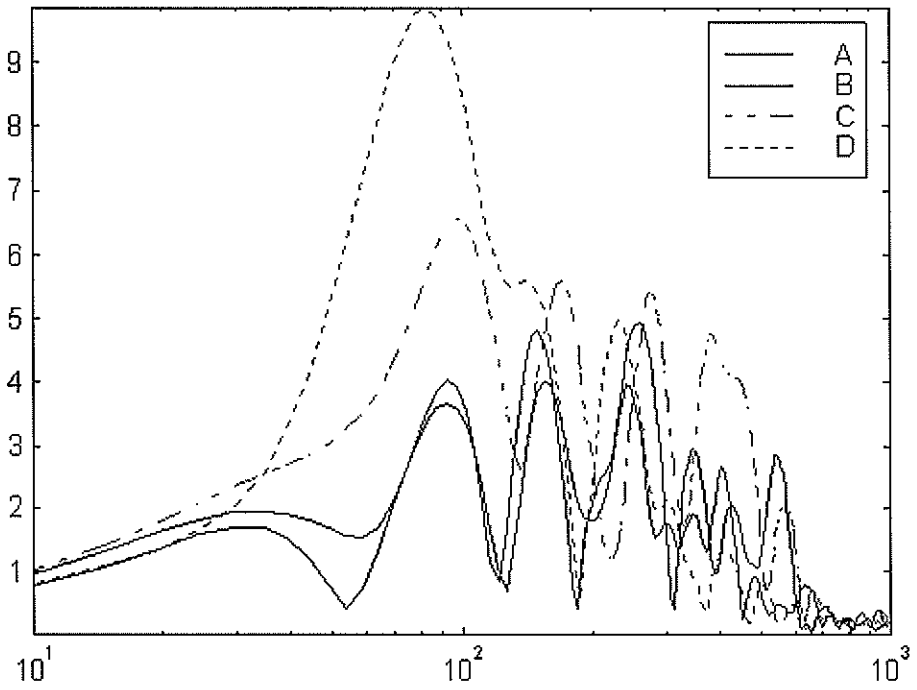

Figure 5.3 Amplitude spectra of body wave group for events recorded by the borehole array. The records from sites A and B are marked by a solid lines; record from station C is marked with dashed-dot line and record from station D is marked by a dotted line.

The array installed in the hangingwall and footwall is used to study the spectral peaks associated with structural and site effects. Table 5.2 shows different dominant frequencies for a number of seismic events observed in channels 2, 3 and 6, and that are not present at station A in solid rock. The peaks are caused by a structural effect, as they are observed at several points in the hangingwall. The prominent finding is that the structure can produce several spectral peaks. Seismic events do not however excite all possible resonance frequencies. Nevertheless, resonance at 30 Hz and 60 Hz is observed most frequently. The location of seismic the events with respect to the position of the stop is the second important feature (the first being structural properties), which determines excitation of the selected resonance.

Table 5.2

Spectral peaks observed at the skin of the hangingwall channels 2, 3 and 6; the peaks are marked by the symbol " * ".

Event number	Spectral Peak [Hz]									
	30	40	50	60	70	80	90	100	110	120
3	*									
7	*	*	*			*				
14	*			*					*	
25		*	*	*		*				*
26	*									
37	*	*	*	*		*		*		
38	*		*	*		*				
42	*			*		*			*	
43	*			*					*	
45	*		*	*					*	
48	*		*	*						
59	*			*						
64	*	*	*							
72	*		*	*					*	
75	*									
83	*									
88	*			*						
89	*		*		*				*	

Inspection of the spectral peaks shows that channels 4 and 5 have site effects in addition to the structural effect. Channel 5 has a very strong resonance at 160 Hz for all seismic events, however data from Table 5.2 do not show such pronounced resonance. Once again, this indicates that the location of the seismic event is the crucial parameter determining excitation of resonant frequency modes. Channel 4 shows a very strong resonance over a broad range of frequencies from 160 Hz to 300 Hz.

The records of the geophone on the footwall (channel 7) in some cases have relatively strong surface waves, which were not observed at the hangingwall sites. In another case, records of the footwall geophone show a very strong signal around 300 Hz and surface wave was not observed.

5.1.5 Structural effect

Almost all records from the hangingwall, the footwall, and the borehole show surface waves. The pulses on the seismograms were classified as surface (Rayleigh) waves when the following features were present:

- arrival after the S-wave,
- frequency contents much lower than body waves,
- decrease in amplitude with distance from the free surface of the underground excavation.

A number of different researchers have confirmed that the dominant frequency of the Rayleigh wave is strongly dependent on the variation of shear wave velocity with depth at the site (Murphy and Shah, 1988). The characteristic dominant frequency at the site can be approximated by the following equation:

$$f = V / 2.3H \qquad (5.1)$$

where: V is the average shear wave velocity and H denotes the depth to the first significant discontinuity. The dominant frequencies of surface pulses wave 40 Hz, 70 Hz and 90 Hz. Thus possible causes of the generation of these waves are layers of 30 m (40 Hz), 20 m (70 Hz) or 14 m (90 Hz) in thickness. The dominant frequency and location of the seismic source determines which layer is excited.

There is a two metres thick layer of Green Bar at 1,0 to 1,8 above the free surface of the excavation. This layer could be responsible for the peak in the spectrum around 350-400 Hz, if it was present everywhere. However, this peak is not strong.

The presence of several Rayleigh wavelets in the seismograms could be interpreted in terms of the existence of a complex structure around the stope. The results of experimental techniques (Daehnke et al., 1997) and numerical modelling (Hildyard et al., 1995) were used to explain the wave interaction with the stope. Three models were investigated: (1) a stope situated in a homogeneous medium, (2) a stope surrounded by fracture softened material, where the interface between the softened and bulk material is bonded, (3) a stope situated within a softened material, with a non-cohesive material interface. The results from the three models were generalised as: (i) Rayleigh wave is well developed in the hanging – and footwall. (ii) Rayleigh waves are able to propagate along the hangingwall and footwall surface, (iii) The non-cohesive parting plane traps energy within the hangingwall and footwall beams in the form of reflected shear waves. In the third experiment the coda wave was much stronger than in the second experiment.

There is an alternative explanation for the surface wave. Lateral changes in the shear wave velocity could lead to the formation of a Rayleigh wave that contains delayed surface waves that reach the seismic station indirectly. The vertical discontinuity could gives rise to the development of surface waves, which then propagate back and forth within the lateral structure. The complicated structure of the recorded Rayleigh waves makes it impossible to identify vertical discontinuities using a small number of recordings (Meier at al., 1998).

5.1.6 Site Effect – Microzonation

The seismic array in the hangingwall was used to study the site effect. The prominent features of records or spectra unique to each record from the hangingwall are called the site effect. Channels 4 and 5 show strong site effects for all seismograms. Channel 5 has strong resonance at 160 Hz (about 20 m wavelength). Channel 4 usually has several peaks around 160 Hz and 300 Hz. At the channel number 3, an 160 Hz peak can be observed but it is very small.

A band pass Butterworth filter (120 Hz-250 Hz) was applied to data from stations 4 and 5 to study the resonance frequency signal in the time domain. At station 4 the filtered signal is strong at the arrival of the SV group (only the vertical component is available) and quickly decays. Usually the resonance signal is not present in the coda. At station 5 the selected signal is distributed across the entire seismogram and its amplitude is smaller than the one recorded at station 4.

The site effect can be explained by introducing a local contrast in medium properties: the contrast between the Green Bar and the quartzite, or the difference in fracture intensity of the rock around the excavation. The site effect is not observed at channel 2 and channel 6 indicating that the width of the inhomogeneity is less than two metres. The length is not well defined, as there is no other station to the right side of geophone 5.

A one-dimensional resonant frequency (f_h) model is commonly applied to estimate the thickness of the layer causing resonance ($H = Vs / 4 f_h$). However, a numerical study leads to the conclusion that the two-dimensional resonant frequency and amplification values differ substantially from their one-dimensional estimate. Bard and Bouchon (1985) showed that the transfer function for different sites at the surface of a sine-shaped valley exhibits specific resonance patterns, with the following characteristics:

- the frequency of the resonance peak is the same at each location within the inclusion regardless of local thickness
- the two-dimensional resonance is controlled by the shape ratio (thickness to half-length ratio) and the impedance contrast insignificant
- the corresponding amplification is the largest in the inclusion centre, and decays toward the edges

The observed pattern of resonance peaks and the motion duration of the resonance frequencies indicate that geophone 5 is in the centre of the inhomogeneity, geophone 4 is off centre and geophone 3 is at the edge.

The one-dimensional resonance at 160 Hz gives a layer thickness of about 4,7 m (for $V_S = 3000$ *m/s*). However this thickness has to be rejected as geophone 2 and 6 do not show similar resonance frequencies.

The resonant frequency of a soft rectangular inclusion (two-dimensional resonance) is given by the following approximate empirical equation:

$$f_0 = f_h \sqrt{1 + (2.9H / L)^2} \qquad (5.2)$$

where: f_0 is the *SV* fundamental resonance frequency and f_h is the one-dimensional resonant frequency. The estimation of the inclusion thickness, *H*, using the two-dimensional resonance, requires knowledge of the length of the inclusion, *2L*. Table 5.3 presents several options for possible inclusion thickness, *H*, and length, *2L*. These dimensions are strikingly large in comparison to the inclusion width of 2 m. However, in relation to a resonant frequency wavelength of 20 m they are quite reasonable.

Table 5.3

A number of possible inclusion thickness* H *and length* 2L*, for a resonance frequency of 160 Hz.

H/L	f_h [Hz]	H [m]	L [m]
0,8	63	12	15
0,6	80	9	16
0,4	104	7	18
0,2	138	5	25

The resonance of the excavation itself (natural resonance) could be another possible explanation for the site effect pattern. The fact that stronger site effects (spectral peaks) are observed at the sites located in the central part of the excavation (channels 5 and 4) supports this claim. Numerical modelling is needed to support or reject the concept of natural resonance of the excavation.

5.1.7 Multi-degree-of-freedom model in time and frequency domains

A method for the time-domain identification of linear multi-degree of freedom structural dynamic systems was outlined by Cichowicz and Durrheim, (1997). Seismic records of a single input and single output are sufficient to determine the transfer function between seismic sensors installed in the solid rock and at the skin of the hangingwall. The transfer function is parameterised as a series of damped oscillators.

The transfer function is obtained in a time domain inversion process. This approach has the additional benefit of being able to observe how the excavation effect and the site effect develop during ground motion caused by a seismic event.

Data from the borehole array shows that the transfer function has at least three different phases. Two phases are observed in the shear wave group and the third phase is associated with surface waves. This indicates that the group of body waves has a very complex composition. Therefore it is difficult to model the whole seismogram with one transfer function. A model of the transfer function obtained at the end of a seismogram matches the output reasonably well, however to get the perfect match it is necessary to use a separate transfer function for each of the three intervals of the seismogram. The good match in the time domain indicates that the spectral peaks can be modelled using damped oscillators.

Data from the hangingwall array are modelled reasonably well with one transfer function. The transfer function from the end of the seismogram matches the whole record. This indicates that the interaction between blocks in the hangingwall can be modelled using several damped oscillators. Figure 5.4 shows the sum of three modal responses calculated at the time 0,105 s (solid line). The model of ground motion correlates well with the real one. (channel 5 - dashed line). The modal frequencies are 225 Hz, 413 Hz and 431 Hz and respective damping ratios are 0,258; 0,075 and 0,462.

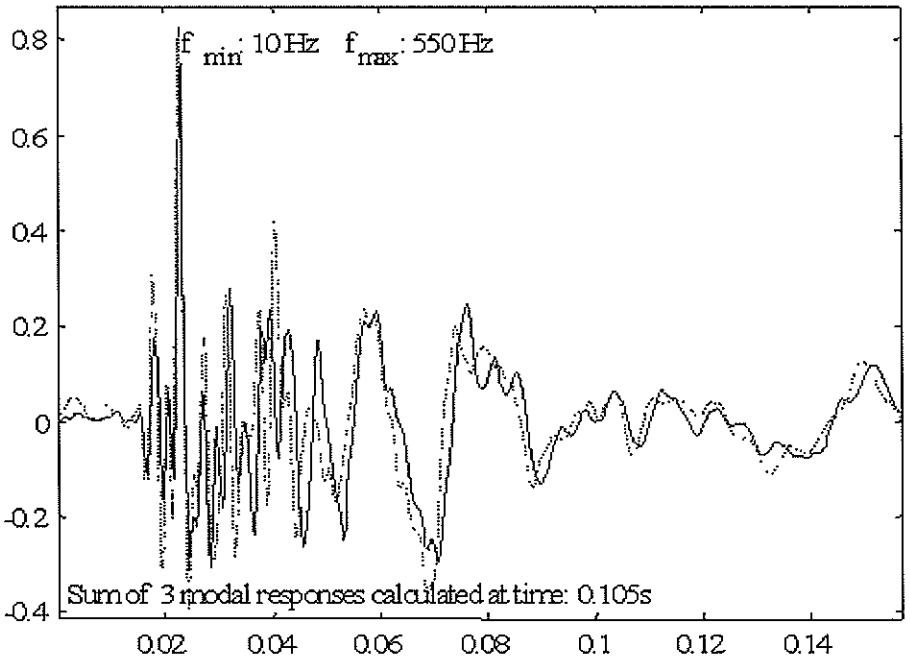

Figure 5.4 The sum of three modal responses calculated at the time 0,105 s (solid line); the match with the real ground motion is very good (channel 5 - dashed line).

Figure 5.5 shows the spectra of the real output (channel 5 is marked by a solid line) and the calculated one (dashed line). Third curve is the transfer function in the frequency domain between channel 5 and channel 6. Resonance at 160 Hz is observed but is very weak. The transfer function does not include 160 Hz resonance.

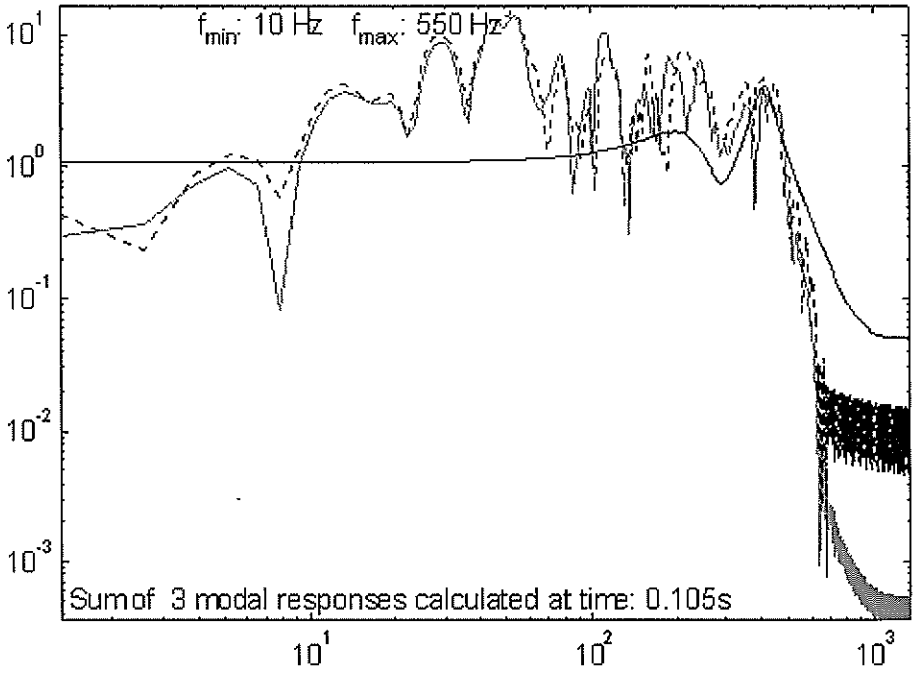

Figure 5.5 Observed (solid line) and calculated (dashed line) spectra for channel 5. The third curve is the transfer function in the frequency domain between channel 6 and channel 5.

5.1.8 Conclusions

A comparison of the records from the borehole array with the records from the skin of the hangingwall quantifies the influence of an underground excavation on the ground motion parameters. Seismic sensors placed in a borehole provide information on the seismic source and structural effects. The array of sensors installed at the skin of the hangingwall provides information about the excavation effect and the site effect.

Structural Effect

- The seismic signal is amplified 2-4 times at the skin of the hangingwall. The spectral peak associated with structural resonance can be up to 10 times stronger than the signal from solid rock.
- Apart from the structural effect and site effect, the distance of the seismic source from the excavation has a significant influence on the vibration.
- The amplitude of the low frequency signal of the surface wave can be greater than that of the body wave. This low frequency signal is created by the structural effect. A low velocity layer around the excavation with a non-cohesive material interface or vertical discontinuities around the excavation can be responsible for the creation of the strong low frequency signal.
- The broad spectrum of possible modal resonance (30 Hz, 50 Hz, 60 Hz, 80 Hz and 110 Hz) indicates the structures surrounding Western Deep Levels are complex.

Site effect

- The site effect is visible as a strong amplification of selected frequencies at channel 4, and 5 on the surface.
- The observed pattern in time and frequency domain suggests that a two-dimensional inclusion is responsible for the site effects. The amplification value associated with a two-dimensional inclusion is extremely large. As a consequence, these values must be taken into account during the assessment of the local seismic hazard.
- The resonance of the excavation itself (natural resonance) could be another possible explanation for the site effect pattern. The fact that stronger site effects (spectral peaks) are observed at the sites located in the central part of the excavation (channels 5 and 4) supports this claim.

5.2 Monitoring falls of ground with Modified Ground Motion Monitor

The management of Lonrho Platinum Mine requested CSIR Mining Technology to developed a method of determining the exact time and location of falls of ground in the mining panels. There was the opinion that most of the falls of ground occurred during the blasting time. A ground motion monitor was modified to fulfil this task.

In collaboration with GAP 416, and M & M Systems, the standard 5 m cable between each geophone and recording box was replaced with 100 m bell wire thin enough to be broken by an average sized fall of ground. This wire was then attached to the hangingwall between the support units. The hangingwall of a potentially hazardous panel was then banded as is shown in Figure 5.6.

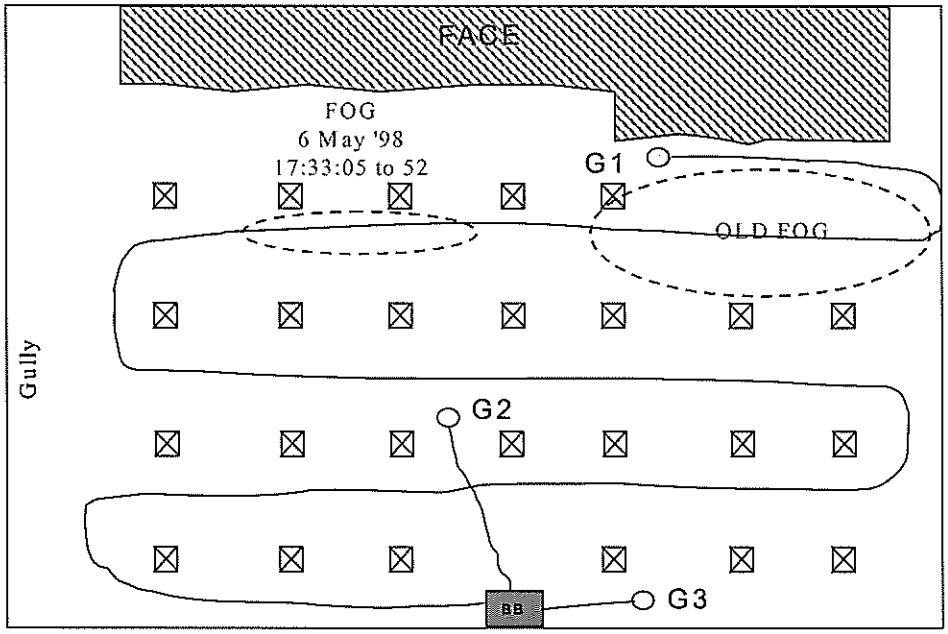

Figure 5.6 Sketch of the geophones and wire deployment for monitoring fall of grounds (FOG) at Lonrho Eastern Plats belt 2.

Figure 5.7 illustrates two consecutive seismograms where channel 3 was disconnected after the fall of ground had cut the circuit. The accuracy of this case is 47 s, or the time interval between these two consecutive events.

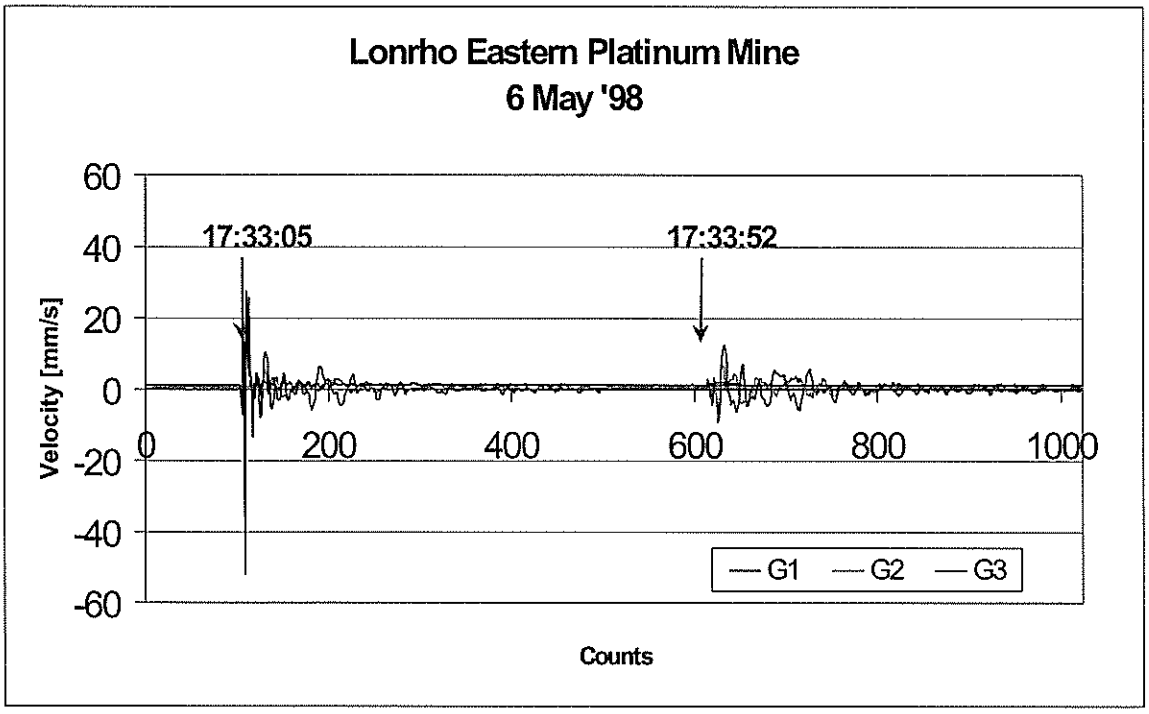

Figure 5.7 Two consecutive seismograms before and after the fall of ground on 6 May '98, recorded at 6 E 1 down-dip Lonrho Eastern Plats belt 2

The development of maximum velocities in the progression to the fall of ground is shown in Figure 5.8. It can be seen that the fall of ground occurred at maximum velocities in the range of 50 to 60 mm/s.

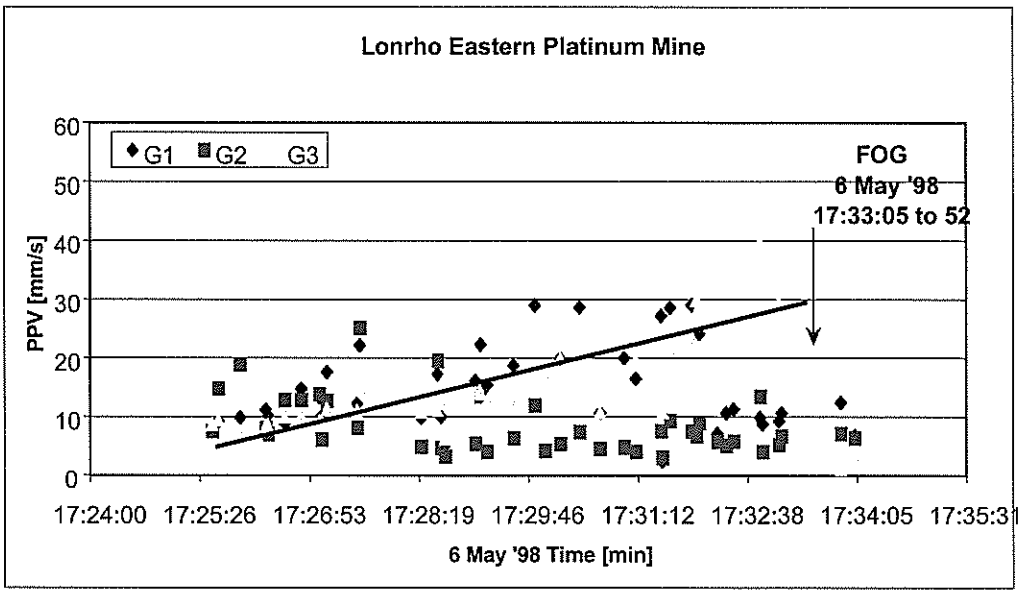

Figure 5.8 Maximum velocities as a function of time shortly before the fall of ground on 6 May '98.

A few moments later a second fall of ground was monitored in a neighbouring panel. In both cases the falls of ground occurred during blasting.

The new modification to the Ground Motion Monitor successfully fulfilled the requirement of monitoring the time of fall of ground.

5.3 Single-block rockburst model

Rockburst-resistant support is currently designed on the basis of an ejection velocity, usually of the order of 3 m/s. The mechanisms of ejection are still a matter for debate. In even the most severe rockburst, there is always rock that has not been ejected. In most minor rockbursts only isolated blocks come out of the hangingwall. Figure 5.9 shows a model of a single-block rockburst, or shake-out.

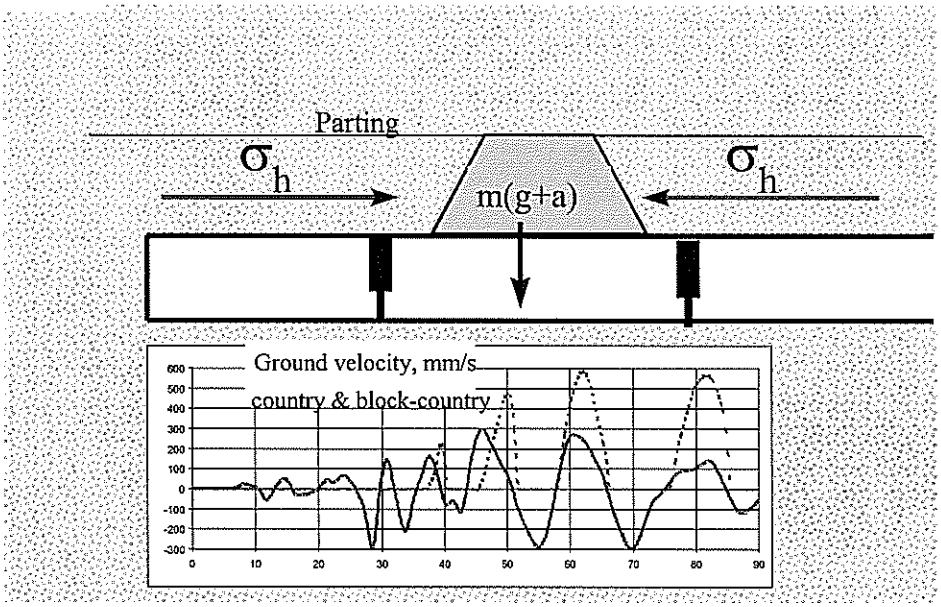

Figure 5.9 Sketch of a single-block rockburst. In this model, the total amount of damage, or relative slip, amounted to 9 mm.

The essence of this model is that damage results from the inability of blocks to move up when the rock mass moves up. In this model, horizontal stress and vertical acceleration control damage.

1. Horizontal stress, quasi-static and dynamic, holds the block in place even during upward acceleration through friction. The dynamic stress can be estimated from the ground motion.
2. The effective weight, or downward force, of the block is increased as the adjacent rock mass is accelerated upwards.

Relative motion and damage occur when the vertical downward forces exceed the vertical upward forces on the block. Damage can accumulate over successive cycles of ground motion.

In addition, damage can possibly be caused by high horizontal stresses, especially when a weak parting is in the immediate hangingwall.

Given the existence of blocks surrounded by fracture planes with known strength, the accuracy of this model depends mostly on deriving good estimates of dynamic stress from seismograms. Rayleigh waves and vertically moving P-waves have been assumed. In the second half of 1998, further models were considered and applied to existing data.

6 Conclusions and Recommendations

The first enabling output involves comprehensive investigations of at least four rockburst accident sites. The investigation by a team of specialists typically encompassed an assessment of the source and damage mechanisms, layout, and support performance. In addition it was decided to include less detailed investigations of other rockburst sites.

- The most common source mechanism of a causative seismic event is slip on either a dyke contact or a fault. In some cases the seismic data coupled with the extent, nature and location of the damage allowed the identification of the source mechanism with a high degree of accuracy.
- Other identified source mechanisms include remnant pillar failure, stabilising pillar foundation failure and face bursting.
- The most common damage mechanism resulting from seismic activity is predictably, collapse and shakedown of hangingwall. Other mechanisms are tunnel wall damage, footwall heave and face rock ejection.
- Many factors affected the severity of damage. Mine layout, factors included poor remnant shape, poor pillar design, breast-on face orientation when approaching geological features and excessive leads or lags between panels. Incorrect input parameters, such as k-ratios, when modelling also resulted in poor layouts. Tunnels positioned in fault loss zones sustained serious damage in some cases. Inappropriate and poorly designed support in tunnels, gullies and stopes and in some cases sub-standard application of the support in these excavations also played a role in determining the severity of the damage sustained.
- Assumptions regarding the stress field affecting a particular mine are probably invalid in many cases. An improved knowledge of the stress field would assist significantly with mine layout (numerical modelling) and both local and regional

support planning. It is recommended that mines make use of a database of stress measurements that has recently been established and in some cases additional stress measurements may be necessary where anomalous situations are evident or anticipated.

- The degree of corrosion of tunnel support can have a significant effect on the extent and severity of damage resulting from a seismic event. Where tunnels are needed for extended periods, and where seismic activity is likely, areas where support may be compromised must be identified and rehabilitated.
- The depth of the unstable zone surrounding tunnels needs to be estimated. This determines the length and spacing of tendon support.
- The siting of tunnels and crosscuts in fault loss zones where extensive mining of nearby reef is planned should be avoided.
- Cementitious packs, designed to yield at loads lower than that required to induce damage in the gully sidewall, have been seen to perform well under dynamic loading. In one case a direct comparison with timber packs could be made.
- The stability of remnant pillars depends largely on the shape and the width: height ratio. The latter may be affected by local geology and by reef geometry. A triangular shape, as opposed to L-shaped or narrow rectangular remnants, which are particularly troublesome, is recommended.
- Backfill can be shown to have a significant regional and local support benefit in some areas particularly on the Far West Rand. The positive effect that backfill has on gully and stope conditions has been observed.

The second enabling output involved the measurement and analysis of the dynamic response of the rock surrounding excavations to seismic shaking. The measurement was be done by means of ground motion monitors in stopes and tunnels. Techniques were developed or adapted for analysing the data. In addition a controlled seismic source (simulated rockburst) was carried out to augment the findings. The influence of support elements and the integrity of the excavation skin was also assessed.

Controlled seismic source experiment

- The distance of the blast holes from the tunnel wall ensured that no gas pressure was involved in damaging the wall of the tunnel. The damage resulted from the interaction of shock wave with the tunnel, similar to what would happen in a rockburst. Petroscope probes and ground penetrating radar scans confirmed the development of new fractures close to and parallel to the damaged tunnel wall.
- Two areas of damage have been identified on the blasting wall:
    - area with high intensity damage: ejection velocity at 3,3 m/s was recorded by an accelerometer ejected with a block of rock
    - area with low intensity damage: ejection velocity at 1,6 m/s was recorded by an accelerometer left over the blasting wall
- High speed camera shots revealed rock fragments being ejected from the wall at velocities in the range of 0,7 m to 2,5 m per second. The measurements were taken in the area of low intensity damage.
- The maximum velocity recorded in the solid rock close to the blast was compare to the velocities recorded on the blasting wall. The ratio of 2,2 times, between the solid and the area with high intensity damage and ratio of 1,3 times between the solid and the area with low intensity damage were found.
- Peak particle velocities recorded on the blasting wall attenuate exponentially with the distance. The velocities measured at distance of 30 m from the blast where at about 20 times less than the velocities measured at 6 m from the blast. The attenuation of the velocities obtained from the calibration blast have similar trend.
- The simulated rockburst was well recorded by the Vaal River Operations regional seismic network. The local magnitude was estimated as M_L = 1,3. Further use of the simulated rockburst for scaling of mine tremors located in this region is recommended.
- Peak particle velocities (PPV's) were measured on the tunnel wall both before and after the experimental blast. The PPV's were as a result of normal mining operations some 100 m from the site. The amplification of the PPV's after the blast were amplified some five, six times indicating the effect of the damage caused to the rock surrounding the excavation.
- In frequency domain well defined amplification was obtain in the low frequency band (0 – 100 Hz)

- The new fractures together with both natural bedding planes and "bow wave" fractures formed during the development of the tunnel determined the shape of blocks ejected from the wall at the time of the simulated rockburst.
- Tendon support of the tunnel had the effect of reducing the PPV's and damage to the wall in their immediate vicinity.
- It was found that the failure of the rock occurred predominantly on prominent discontinuities such as bedding planes and fractures. Damage to a tunnel is changed in the presence of discontinuities and this fact should be taken into account when support is designed.

Dynamic behaviour of the rock around underground excavations

- The ground motion at points on the skin of a stope hangingwall was found to be some four to ten times larger than at a point 6,5 m into the hanging wall. Coda waves were also more developed on the skin. Measurements at 0,5 m, 2,5 m and 4,5 m showed intermediate behavior. It was suggested that the fracture zone acting as a wave-guide causes the enhanced levels of ground motion and that multiple scattering causes the prolonged duration of motion.
- Ground motion on the abutment side of a fault in the hangingwall was much lower than the ground motion on the other side. Possible mechanisms involve the reduction of bedding-plane slip or the loss of seismic energy to the solid ground ahead of the abutment.
- The results from velocity analysis have indicated that the time delays observed between pairs of geophone sites exceeded the travel time for P- and S-waves, in solid rock indicating lower wave velocities. These lower velocities are expected, given the high degree of fracturing near the skin of the stope. It is expected that this will give insight into the mechanisms of energy trapping. It will also assist in estimating the effective stiffness of the fractured rock and, thereby, it's dynamic response.
- Two mechanisms of dynamic response have been defined: structural response, defined as a common spectral behaviour at all surface seismograms; and local site effect, defined by spectral peaks at one or two surface seismograms. The spectral peaks interpreted as the structural response (40 Hz and 70 Hz for all surface sites) could be associated with the presence of the Green Bar layer in

the quartzite, while the site effects observed at G4 and G5 would be more dependent on the difference in the intensity of the local fractures in the vicinity of the geophones. However, this interpretation is too broad and numerical modelling is required to provides insights into the actual mechanism of dynamic behaviour of the hangingwall.

- The results obtained for the dynamic response of the site, including both the structural response and the local site effect, can be related to the existing support methodology. The normalised load-deformation curve, presently used as a support design criterion, could be modified by the dynamic response spectrum in order to provide additional design information.

7 References

Aki, K. and Richards, P. G., 1980. Quantitative seismology, Freeman, San Francisco.

Anon, 1988. An industry guide to methods of ameliorating the hazards of rockbursts and rockfalls. Chamber of Mines Research Organisation. Chamber of Mines of South Africa.

Bard, P. and Bouchon, M., 1985. The two-dimensional resonance of sediment-filled valleys, Bull. Seism. Soc. of Am., Vol. 75, pp. 519-541.

Butler, A. G. and Van Aswegen, G., 1993. Ground velocity relationship based on a large sample of underground measurements in two South African mining regions, In: R. P. Young (Editor), Rockbursts and Seismicity in Mines, Kingston, Canada, pp. 41-51.

Cichowicz, A., 1995. Develop a more reliable means of assessing safety risk due to rockbursts and rockfalls as a managerial decision support technique Report for CSIR Mining Technology, Johannesburg, South Africa.

Cichowicz, A. and Durrheim, R.J., 1997. The Site Response of the Tunnel Sidewall in a Deep Gold Mine, Analysis in the Time Domain, In: R.G. Gurtunca and T.O. Hagan (Editors), *Proc. 1st Southern African Rock Eng. Symp.* Johannesburg South Africa, pp. 56-61.

Daehnke A., 1998. Personal communication on the choice of blast parameters. CSIR Mining Technology, July, 1998.

Daehnke, A., Rossmanith, H. B. and Kanashmirner R. E., 1996. Using dynamic photoelasticity to evaluate the influence of parting planes on stress wave interaction with stopes, Int. J. Num. and Analy. Methods in Geomech., 20 pp.101-107

Daehnke, A., L. M. Andersen, D. de Beer, E. Esterheinzen, F. J. Glisson, E. P. Jaku, J. S. Kuijpers, A. V. Peake, P. Piper, G. B. Quaye, N Reddy, M. C. K. Roberts, J. K. Shweitzer, R. D., Steward. 1998. Stope Face Support systems, SIMRAC Final Report on Final Project Report GAP 330. Pretoria: Department of Minerals and Energy, 530p.

Drescher, K 1998. Classification of rock specimen uniaxial compressive strength, Internal report, CSIR: Division of Mining Technology, Auckland Park 2006, S.A.

Durrheim, R.J., Kullmann, D. H., Stewart, R. D. and Grodner, M. 1996. Seismic excitation of the rock mass surrounding an excavation in highly stressed ground. In M. Aubertin, F. Hassani and H. Mitri (eds), Proc. 2nd North American Rock Mechanics Symposium: 389-394. Rotterdam: Balkema.

Durrheim, R.J., Milev, A.M., Spottiswoode, S.M. & Vakalisa, B. 1997. Improvement of worker safety through the investigation of the site response to rockbursts, *SIMRAC Final Report on Final Project Report GAP 201.* Pretoria: Department of Minerals and Energy, 530p.

Durrheim, R.J., Roberts, M.K.C., Haile, A.T., Hagan, T.O., Jager, A.J., Handley, M.F., Spottiswoode, S.M. & Ortlepp, W.D. 1998. Factors influencing the severity of rockburst damage in South African gold mines, *Journal of South African Institute for Mining & Metallurgy* Vol. 98, No.2. 53-57.

Durrheim, R. J., Jager, A. J. and G. York. 1998. Rock engineering aspects of the rockburst at No. 11 shaft, Impala Platinum Mine, on 31 December 1997, Internal report, CSIR: Division of Mining Technology, Auckland Park 2006, S.A.

Essrich, F. and Amidzic, D. 1999. Influence of backfill on seismicity in the West Rand Region. To be published. 2nd Southern African Rock Engineering Symposium (SARES99). Sept 1999. Johannesburg.

Finnie, G. J., 1998. Personal communication on the seismic parameters reported by Vaal River Operations regional seismic network, Vaal Reef, 2162.

Grave, M. 1998. The extensometer results of the sidewall-monitoring of 53-54 crosscut at Vaal Reefs No. 9 Shaft following a simulated rockburst, Internal report, CSIR: Division of Mining Technology, Auckland Park 2006, S.A.

Grodner, M. 1998. GPR Results from the Vaal Reefs controlled blast site, Internal report, CSIR: Division of Mining Technology, Auckland Park 2006, S.A.

Guler, G., G. B. Quaye, J. K. Shweitzer, M. Grodner, A. J. Jager, N. Reddy, L. Andersen, and, A. Milev. 1998. A methodology for the definition of geotechnical areas within the South African Gold and Platinum stoping horizons. SIMRAC Final Report on Final Project Report GAP 416. Pretoria: Department of Minerals and Energy, 530p.

Hagan, T.O, Haile A. T., Spottiswoode S.M., Turner A.P. and Malan D.F. 1998. Hartebeesfontein No. 4 Shaft: Rock Engineering Aspects of the Rockburst Accident on the of 5th March 1998. *Internal report,* CSIR: Division of Mining Technology, Auckland Park 2006, S.A.

Hagan, T. O., M. K. C. Roberts, A. T. Haile, A. Daehnke, N. Reddy, R. J. Durrheim, and W. D. Ortlepp. 1997. Follow-up visit to the affected by the rockburst at Elandsrand Gold Mine (Deelkraal Section) on 7 May 1997, Internal report, CSIR: Division of Mining Technology, Auckland Park 2006, S.A.

Haile, A. T. 1998a. Strata control in tunnels and an evaluation of support units and systems currently used with a view to improving the effectiveness of support, stability and safety of tunnels, SIMRAC Final Report on Final Project Report GAP 335. Pretoria: Department of Minerals and Energy, 135 p.

Haile, A. T. 1998b. Investigation of damage to 64 B West haulage at the Great Noligwa Mine due to a seismic event of magnitude M = 3,7 on 21 August 1998, Internal report, CSIR: Division of Mining Technology, Auckland Park 2006, S.A.

Hildyard, M. W., Daehnke, A. and Cundall, P. A., 1995. WAVE: A computer prog ram for investigating elastodynamic issues in mining, Proc 35th U.S. Symp on Rock Mech., pp. 519-524.

Kaiser, A. G., 1993. Support of tunnels in burst-prons ground - Toward a rational design methodology, In: R. P. Young (Editor), Rockbursts and Seismicity in Mines, Kingston, Canada, pp. 13-29.

Kouzniak N. (1998). Personal communication on *'Comparisons with the analytical propagating source model'*. University of Vienna, Austria.

Kouzniak N. and Rossmanith H.P. (1998). Supersonic detonation in rock mass - Analytical solutions and validation of numerical models - Part 1 stress analysis. *In print, submitted to FRAGBLAST.*

Lay, T. and Wallace, T.C. 1995. Modern Global Seismology, Academic Press, San Diego, USA, p 49.

Le Bron, K. 1998. Determination of the average stress levels at the 53-54 crosscut at Vaal Reefs No. 9 Shaft, Internal report, CSIR: Division of Mining Technology, Auckland Park 2006, S.A.

Le Bron, K., A. T. Haile. 1998. Investigation of the influence of a support unit on the stability of a tunnel in fractured rockmass as the seismic wave passes, Internal report, CSIR: Division of Mining Technology, Auckland Park 2006, S.A.

Linkov, A. L. and Durrheim, R. J., 1998. Velocity amplification considered as a phenomenon of elastic energy release due to softening, *Proc of the 3rd conference of mechanics of jointed and faulted rock, Ed H-P Rossmanith,, pp. 243-249*

Lightfoot, N., Kullmann, D.H., Toper, A.Z., Stewart, R.D., Grodner, M., Janse van Rensburg, A.L. & Longmore, P.J. 1996. Preconditioning to reduce the incidence of face bursts in highly stressed faces. *Mining Technology Division of CSIR, SIMRAC Final Report, Project GAP 030.*

McGarr, A., Green, R. W. E. and Spottiswoode, S. M., 1981. Strong ground motion of mine tremors: some implications for near source ground parameters, Bull. Seism. Soc. of Am., Vol. 71, pp. 295-319.

Meier, P. G., Malischewsky, P. G. and Neunhofer, H., 1998. Reflection and transmission of surface waves at a vertical discontinuity and imaging of lateral heterogeneity using reflected fundamental Rayleigh waves, Bull. Seism. Soc. of Am., Vol. 87, pp. 1648-1661.

Milev, A. M., Spottiswoode, S. M. and Stewart, R. D., 1998. Dynamic response of the rock surrounding deep level mining excavations, Proc. 9th ISRM, Paris'99, submitted.

Murphy, J. R. and Shah, H. K., 1988. An analysis of the effects of site geology on the characteristics of near-field Rayleigh waves, Bull. Seism. Soc. of Am. Vol. 78, pp. 64-82.

Napier. J, F. Malan, E. Sellers, A. Daehnke, M. W. Hilyard, T. Dede, and, K and J. Shou. 1998. Deep Gold Mine fracture zone behaviour, SIMRAC Final Report on Final Project Report GAP 322. Pretoria: Department of Minerals and Energy, 530p.

Ouchterlony, S Nie, Nyberg, U. and Deng J. 1997. Monitoring of large open cut rounds by VOD, PPV and gas pressure measurements. Fragblast International *Journal of Blasting and Fragmentation* Vol1, No1, pp 3 - 25.

Persson, P., R. Holmberg, and Y. Lee, 1990. Rock blasting and explosives engineering, CRC, Press, USA.

Reddy, N. 1998. Pre and post blast geological investigation of the controlled blast site, Internal report, CSIR: Division of Mining Technology, Auckland Park 2006, S. A.

Rorke A.J. 1992. Measurement of the direct effects of preconditioning blasts. Monitored results from the first test blast. Internal report, prepared for D. Adams, Feb 1992, COMRO, Ref R62/92.

Rorke, A. J. 1998. Vaal Reefs rockburst simulation project, report, Blastinfo, P.O. Box 70040, Bryanton 2021, S.A.

Schweitzer, J. K. Johnson R. A., 1997. Geotechnical classification of deep and ultra-deep Witwatersrand mining areas, South Africa, Mineralium Deposits, V 32, 4, pp. 335-338.

Spottiswoode, S.M., Durrheim, R.J., Vakalisa, B. & Milev, A.M. 1997. Influence of fracturing and support on the site response in deep tabular stopes, In: *R.G. Gutunca and T.O. Hagan (Editors), Proc. 1st SARES,* pp. 62-68

Spottiswoode, S. M., M. Grodner, F. Malan, and A. Z. Toper. 1998. Rock engineering aspects of the rockburst at the Western Deep Levels South Mine on 7 January 1998, Internal report, CSIR: Division of Mining Technology, Auckland Park 2006, S.A.

Stacey, T. R. and Wesseloo, J. 1998. Evaluation and upgrading of records of stress measurement data in the mining industry. SIMRAC project GAP511b Final Report.

Turner, P. A. 1998. Report on the investigation of several rock-burst damaged sites at Western Deep Levels, between June and October' 98, *Internal report,* CSIR: Division of Mining Technology, Auckland Park 2006, S.A.

Van den Heever, P. 1982. The influence of geological structure on seismicity and rockbursts in the Klerksdorp Goldfield. M.Sc. Thesis, RAU, Johannesburg (unpublished).

Wagner, H, 1984. Support requirements for rockburst conditions, in Proceedings of the 1st International Congress on Rockbursts and Seismicity in Mines, Johannesburg, 1982, N. C. Gay and E H Wainwright (eds.), SAIMM, Johannesburg, pp. 209-218,

8 Published Articles

Cichowicz, A., Milev A .M. & Durrheim, R. J. 1998. Transfer function for a seismic signal recorded in solid rock and on the skin of an excavation, submitted *to Journal of South African Institute for Mining & Metallurgy.*

Cichowicz, A., Milev A .M. & Durrheim, R. J. 1998. Rock mass behaviour under seismic loading in deep mine environment, submitted to *Journal of South African Institute for Mining & Metallurgy.*

Durrheim, R.J., Roberts, M.K.C., Haile, A.T., Hagan, T.O., Jager, A.J., Handley, M.F., Spottiswoode, S.M. & Ortlepp, W.D. 1998. Factors influencing the severity of rockburst damage in South African gold mines, *Journal of South African Institute for Mining & Metallurgy* Vol. 98, No.2. 53-57.

Hagan, T.O., Milev, A.M., Spottiswoode, S.M., Reddy, N. & Hildyard, M.W. 1998. Simulated Rockburst on the wall of Underground Tunnel, In: T.O. Hagan (Editor), *Proc. 2nd SARES symposium, Johannesburg, 1999,* in preparation

Hildyard, M.W., Milev, A.M., & Rorke A.J. 1998. Numerical Modelling of an Experimental Rockburst Near a Mining Tunnel, In: T.O. Hagan (Editor), *Proc. 2nd SARES symposium, Johannesburg, 1999,* in preparation

Milev, A.M., Spottiswoode S.M. & Stewart R.J. 1998. Dynamic response of the rock surrounding deep level mining excavations, *Proc of the 9th ISRM congress, Paris 1999*, in preparation.